

The Three-Dimensional Numerical Simulation of Crystallizing Media

Thesis submitted in accordance with the requirements of the University of Liverpool
for the degree of Doctor in Philosophy by Michael Thomas Elliott.

February 1998

LIVERPOOL
UNIVERSITY
LIBRARY



Abstract

The Three-Dimensional Numerical Simulation of Crystallizing Media

The textural evolution of a crystallizing medium is the result of two main physical processes; the nucleation and growth of crystals. The development of textures is currently poorly understood, because it is difficult to interpret three-dimensional textures from two-dimensional sections of a crystallized medium which only depict the final stage of textural evolution. An understanding of the textural evolution of a crystallizing medium is fundamentally important because it records information about the physical processes that occurred during the formation of the medium, such as the flow of fluid phases.

A new, three-dimensional numerical simulation of the textural development of crystallizing media is presented. The simulation produces three-dimensional textures that can be evolved progressively with time which can then be 'thin-sectioned' to compare with and help understand real textures. The texture is simulated by nucleating crystals in a volume and then allowing them to grow by the accretion of unit cell-like elements. Complicated textures are produced by the impingement and interference of the growing crystals. Variation of the nucleation density, anisotropic growth rates and the relative time at which different phases nucleate can allow the evolution of many different textures to be studied.

A new general method for characterizing the void-space and calculating transport properties, such as permeability and electrical conductivity, for three-dimensional porous media is presented. This method partitions the void-space into pore bodies and pore throats enabling a network simulation to be used to calculate the transport properties of the medium. This method is applied to the three-dimensional textures produced by the numerical simulation of crystallization.

The three-dimensional numerical simulations of crystallization and fluid-flow have been used to investigate two different problems. First, the numerical simulation of crystallization has been used to investigate the distributions of apparent dihedral angles expected in unequilibrated rock textures for comparison with those expected in equilibrated rock textures. An important conclusion of this work is that apparent dihedral angle curves for unequilibrated textures may be similar to those for equilibrated textures. Therefore great care must be taken when interpreting distributions of apparent dihedral angles. Second, the network simulation of fluid-flow has been used to investigate permeability in crystallizing igneous systems which has not been possible previously because the time and length scales involved in the crystallization of igneous rocks preclude direct experimentation on melts at magmatic temperatures. Two different single crystal phase igneous systems were investigated; a system with a homogeneous nuclei distribution and a system formed by the over-growth of a settled distribution of pre-existing crystals. An important implication of this work is that it is only possible to crystallize monomineralic rocks from a melt if compaction and/or convection and hence equilibration is occurring.

Acknowledgements

I would like to thank my supervisors, Mike Cheadle and John Wheeler; Mike for the inspiration for this thesis and John for reminding me that the real world is never that simple. I would also like to thank my examiners Andy Woods and Mike Atherton. Steve Bryant for being my permeability guru from afar (the wonders of e-mail) and David Coker for providing the tomographic image of the Fontainebleau sandstone sample. I am indebted to Alan McCormack, C.S.D. and Mary Thorpe for keeping the computers working. The Natural Environment Research Council are gratefully acknowledged for funding.

The moment you've all been waiting for, your fifteen minutes of fame. Thanks to Patster for being earnest (cricket is rubbish!); Caroline for reading this 'wafer'; Susie for food when needy; Rachel and Kathy for being top office mates; Markr for chewing the cud on assorted topics over the last three years; Dougal for talking 'balls'; Mattjack for bizarre 'scientific' conversations (touché); Nickc for the odd perl (sic) of wisdom; and anybody else I've interacted with during my time in Liverpool.

Moral support from afar has been gratefully received from my Mum and Brother. Last, but by no means least, thanks to Charlotte for putting up with me during writing up!

Or a *thing* about some *stuff*.

TABLE OF CONTENTS

CHAPTER 1	1
INTRODUCTION	1
1.0 INTRODUCTION.....	1
1.1 PRINCIPLE AIMS	1
1.2 THESIS OUTLINE.....	2
CHAPTER 2	3
THE TEXTURES OF NON-EQUILIBRATED CRYSTALLIZING MEDIA	3
2.0 INTRODUCTION.....	3
2.1 <i>Nucleation of Crystals</i>	3
2.2 <i>Growth of Crystals</i>	4
2.3 SUMMARY	4
CHAPTER 3	5
THE SIMULATION OF THE TEXTURES OF NON-EQUILIBRATED CRYSTALLIZING MEDIA	5
3.0 INTRODUCTION.....	5
3.1 PREVIOUS MODELS	5
3.1.1 <i>Derivation of the JMA Model</i>	6
3.1.2 <i>Discussion of the Assumptions of the Analytical Model</i>	9
3.2 3-DIMENSIONAL NUMERICAL SIMULATION.....	10
3.2.1 <i>Spatial Partitioning and the Representation of Objects in Three-Dimensions</i>	10
3.2.2 <i>The Model Algorithm</i>	11
3.2.2.1 <i>Ideal Morphology</i>	12
3.2.2.2 <i>Space-Filling Morphology</i>	14
3.2.3 <i>Problems with the Model</i>	15
3.3 APPLICATION OF THE MODEL TO THE CRYSTALLIZATION OF ROCKS	16
3.3.1 <i>Assumptions of the Model for Crystallizing Rocks</i>	16
3.3.2 <i>Removal of Edge-Effects</i>	17
3.4 TESTING THE MODEL.....	17
3.4.1 <i>Comparison with an Analytic Solution</i>	17
3.4.2 <i>Comparison with Experiment</i>	18
3.5 CONCLUSIONS	18
CHAPTER 4	19
TEXTURAL EQUILIBRIUM IN ROCKS	19
4.0 INTRODUCTION.....	19
4.1 THREE-DIMENSIONAL NUMERICAL SIMULATION	21
4.2 RESULTS	22
4.2.1 <i>Fully Crystallized Textures</i>	22
4.2.2 <i>Partially Crystallized Textures</i>	24
4.3 DISCUSSION.....	25
4.3.1 <i>Fully Crystallized Textures</i>	25
4.3.2 <i>Partially Crystallized Textures</i>	26
4.4 CONCLUSIONS	27
CHAPTER 5	29
THE SIMULATION OF THE PERMEABILITY AND THE ELECTRICAL CONDUCTIVITY OF POROUS MEDIA	29
5.0 INTRODUCTION.....	29

5.1 THE CALCULATION OF PERMEABILITY	32
5.2 THE CHARACTERIZATION OF VOID-SPACE	36
5.2.1 <i>Previous Methods for Characterizing the Void-Space</i>	36
5.3 CALCULATION OF PERMEABILITY/ELECTRICAL CONDUCTIVITY USING A NETWORK SIMULATION AND ITS RELATION TO THE CHARACTERIZATION OF THE VOID-SPACE.....	39
5.3.1 <i>Calculation of Permeability using a Network Simulation</i>	39
5.3.2 <i>The Three-Dimensional Numerical Characterization of Void-space</i>	41
5.4 PARTITIONING OF THE VOID-SPACE IN THREE-DIMENSIONS	42
5.4.1 <i>Erosion of the Void-Space in Three-Dimensions</i>	43
5.4.2 <i>Partitioning of the Void-Space in Three-Dimensions</i>	44
5.4.3.1 <i>Combining the results of the Pore-Characterization Algorithm with the Network Simulation Algorithm</i>	45
5.4.3.2 <i>Calculating Absolute Permeability</i>	46
5.4.3.3 <i>Removal of Dead-End Branches in the Network Topology</i>	46
5.4.4 <i>Calculation of the Electrical Conductivity</i>	47
5.5 TESTING THE ALGORITHM.....	49
5.5.1 <i>Self-Consistency</i>	49
5.5.2 <i>Comparison with Experimental Results</i>	49
5.5.3 <i>Fontainebleau sandstone: case study</i>	49
5.6 CONCLUSIONS	55
CHAPTER 6.....	57
THE PERMEABILITY OF PARTIALLY MOLTEN ROCKS	57
6.0 INTRODUCTION.....	57
6.1 PERMEABILITY RESULTS FOR THE SIMULATIONS OF CRYSTALLIZING MEDIA	58
6.1.1 <i>The Determination of a Representative Volume (ReV)</i>	58
6.1.2 <i>The Permeability of the Models</i>	59
6.1.3 <i>Scaling of the Permeability Results</i>	61
6.1.4 <i>Sources of Error in the Calculation of Permeability</i>	61
6.1.5 <i>Permeability-Porosity Relationships for the Three Different Models</i>	62
6.2 COMPARISON OF THE PERMEABILITY RESULTS FOR THE SIMULATED CRYSTALLIZING MEDIA WITH EXPERIMENT AND THEORY	63
6.2.1 <i>Comparison of the Permeability of the Simulated Crystallizing Media with Theoretical and Experimental Work on Sphere Packs</i>	64
6.2.2 <i>The Permeability of Crystallizing Igneous Systems</i>	65
6.2.2.1 <i>Implications</i>	67
6.3 CONCLUSIONS	68
CHAPTER 7.....	70
CONCLUDING REMARKS AND FUTURE WORK	70
7.0 CONCLUSIONS	70
7.1 FUTURE WORK	72
7.1.2 <i>Fluid-Flow</i>	73
7.1.3 <i>Textures</i>	73
REFERENCES.....	74
APPENDIX A: PUBLICATIONS IN SUPPORT OF THIS THESIS	A.1

Chapter 1

Introduction

1.0 Introduction

The textures of a crystallizing medium record fundamental information about how that medium formed including the evolution and behaviour of fluid flow within the medium. A medium's texture is a complex three-dimensional structure that commonly has been observed by two-dimensional sectioning. Two examples of the textures of rocks are simple, texturally equilibrated grain boundary geometries (see fig. 1.1) and complex, texturally non-equilibrated grain boundary geometries (see fig. 1.2). A texturally equilibrated rock is one in which the surface topology of its grains is in mechanical and thermodynamical equilibrium. Previous work has focused on texturally equilibrated media (Beeré, 1975, Von Bargen and Waff, 1986, Cheadle, 1989) which may be applicable to mantle and lower crustal rocks, but due to the complexity of the problem there has been no analogous work on texturally non-equilibrated media which may be applicable in faster cooling systems, such as magma chambers. This thesis presents a model for the textural evolution of non-equilibrium, crystallizing media and methods for quantifying fluid flow in such media.

1.1 Principle Aims

The principal aims of this thesis are to:

- i) Develop a three-dimensional model of crystallization textures in non-equilibrium media;
- ii) Compare the textures of equilibrium and non-equilibrium media;
- iii) Develop a method for characterizing the void-space of porous media;
- iv) Develop a method for calculating the permeability and electrical conductivity in porous media;
- v) Investigate permeability in texturally non-equilibrated crystallizing media;

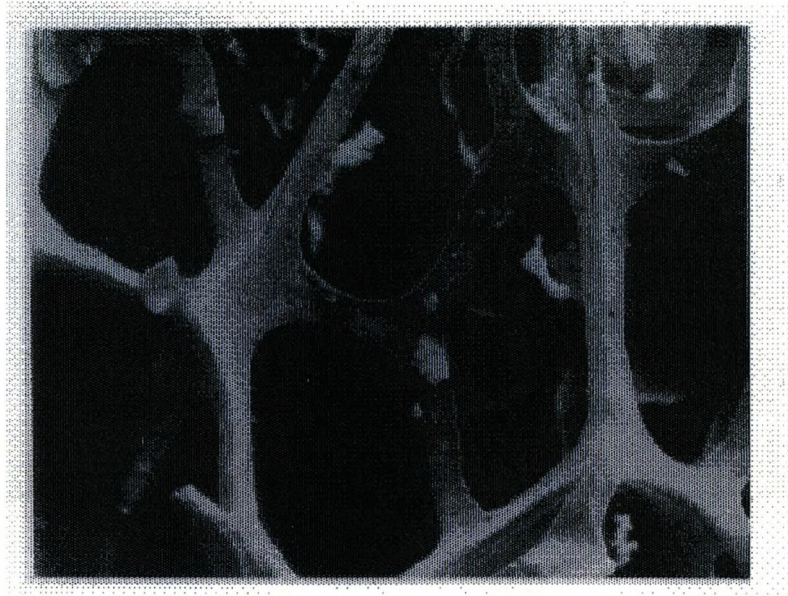


Figure 1.1 Example of the void-space network of an equilibrated system. The image is a scanning electron micrograph of an inter-connected void-space network formed by liquid phase sintering. The solid grains have been removed by chemical dissolution. Composition and scale are unknown (after German, 1985).

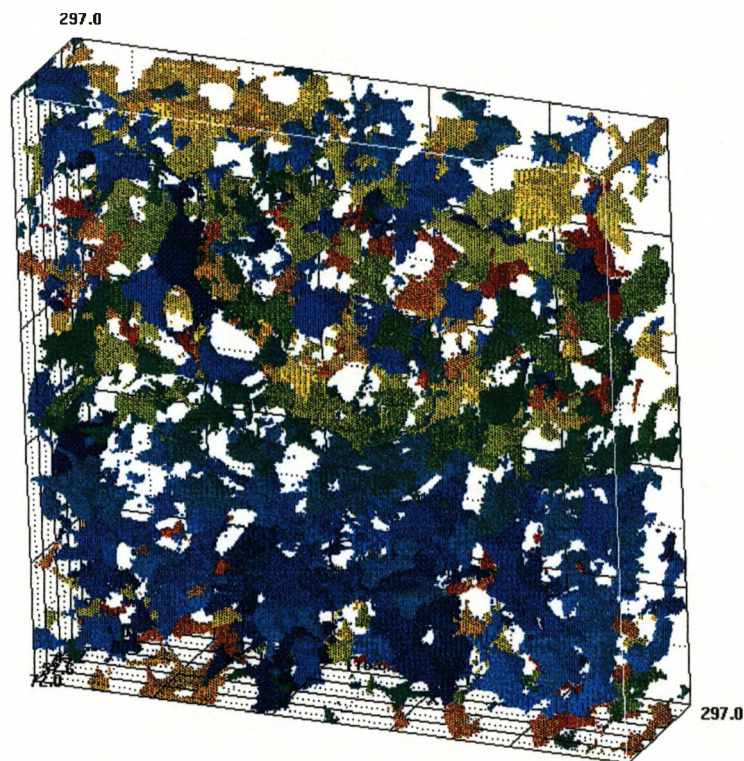


Figure 1.2 Example of the void-space network of a non-equilibrated system. The image is constructed from the micro-tomographic reconstruction of a Fontainebleau sandstone sample. The diagonal of the front face of the image is 3 mm (sample courtesy of D.A. Coker).

1.2 Thesis Outline

Chapter 2 outlines the approach taken for modelling the complex processes occurring during the crystallization of texturally non-equilibrated media. The modelling of these processes are described in detail in Chapter 3. In Chapter 4 a critique of one method for determining the degree of textural equilibration in a medium is made by comparing the results measured from simulated non-equilibrium textures with equilibrium textures. Chapter 5 presents general methods for characterizing the void-space of porous media and develops a technique for calculating permeability and electrical conductivity. These methods are applied to a micro-tomographic image of a sandstone as a test of the technique. Chapter 6 applies these methods to porous media generated by the model outlined in Chapter 3. Chapter 7 contains concluding remarks and discussion of future work.

All computer code used in this thesis was written by the author except for the random number generator used in the crystallization simulation (Chapter 3) (which was from the NAG FORTRAN 77 library) and is available upon request. Visualization of the results was achieved using AVS Express and GMT.

Chapter 2

The Textures of Non-Equilibrated Crystallizing Media

2.0 Introduction

Textures are formed by the geometrical relationships between crystals. For example, the texture may be defined by the geometry of the boundaries between different crystals in the case of a single-phase medium (see fig. 2.1), or the fluid-solid interface in a two-phase medium (see fig. 2.2). The texture of a medium depends fundamentally on the spatial distribution of the growing crystals. Therefore to model the textures of non-equilibrated crystallizing media, a knowledge of the *nucleation* (spatial distribution) and *growth* (morphology, rate) of the crystals is required.

2.1 Nucleation of Crystals

Nucleation in a melt is a process by which atoms aggregate to form a thermodynamically stable region (nucleus), which with further addition of atoms would become a crystalline region within a phase boundary between the crystal and melt. The spatial distribution of these nuclei will depend on the style of nucleation within the system. The style of nucleation can take two general forms, homogeneous nucleation arising from some random fluctuation within the melt (of temperature or pressure for example) or heterogeneous nucleation occurring on a pre-existing phase within the melt. Due to its sub-microscopic nature nucleation is difficult to study experimentally and theoretically (Kirkpatrick, 1981). Although nucleation theory (Dowty, 1980, Kirkpatrick, 1981, 1983) predicts the temporal distribution of nuclei it does not predict their spatial distribution and relatively little is known about this. In the case of homogeneous nucleation the spatial distribution of nuclei is usually considered random, although the process of nucleation itself must modify the temperature and compositional fields within the melt thereby affecting subsequent nucleation. The effects of this on the spatial distribution of later nuclei are unknown. In the case of heterogeneous

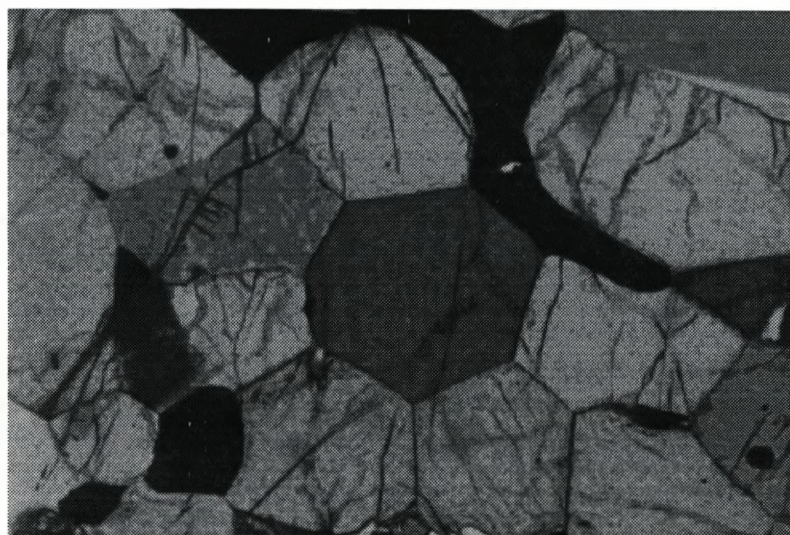


Figure 2.1 Photomicrograph of olivine-magnetite adcumulate from Freetown complex, Sierra Leone. Single-phase boundaries between olivine grains are clearly visible. Horizontal field of view is 4 mm. (Courtesy of R. Hunter).



Figure 2.2 Photomicrograph of Fontainebleau sandstone showing quartz overgrowths on sand grains. Two-phase boundaries between the quartz overgrowths and the void-space are clearly visible. Horizontal field of view is approximately 1 mm (after Bryant *et al.*, 1993).

nucleation the heterogeneity in the spatial distribution of nuclei may be very large, for example nucleation on a substrate at the edges of a melt or nucleation on irregularly distributed pre-existing phases. Overall, very little is known quantitatively about nucleation within igneous systems (Dowty, 1980).

2.2 Growth of Crystals

Growth of a crystal occurs by the addition of atoms to a thermodynamically stable region or nucleus (Dowty, 1980). The growth rate and shape of an isolated crystal is controlled by two main processes, diffusion in the melt, which can be driven by chemical and/or thermal gradients and interface attachment/detachment (Dowty, 1980, Kirkpatrick, 1981). Interaction between these processes can cause large differences in crystal shape from isotropic and rounded, anisotropic and faceted to dendritic (or branching). In addition if there are neighbouring crystals, then crystal growth rate and shape will be affected by the competition between the crystals for space and for the extraction of atoms from the melt for growth. However, once again little is known quantitatively about the controlling factors in igneous systems (Dowty, 1980).

2.3 Summary

The above discussion suggests that the textures present in a system crystallizing under non-equilibrium conditions are controlled by the initial distribution of crystal centres (nucleation) and their subsequent evolution with crystallization (growth). Therefore, if a distribution of crystal centres is prescribed and the growth and interaction of crystals can be calculated then it should be possible to generate realistic textures.

The essence of the approach used in Chapter 3 to model crystallizing systems is therefore **to simulate the results of the processes that generate the textures in crystallizing systems not the actual processes themselves**. An example of this would be to simulate the growth of a crystal by prescribing a growth rate of an interface rather than modelling the addition of atoms that compose that interface directly. This is justifiable firstly because many of the atomic scale processes are difficult to predict quantitatively due to lack of theoretical and critical data (Dowty, 1980) and secondly because of the extensive computation time that would be required to simulate the crystallization processes themselves at the scale of single atoms.

Chapter 3

The Simulation of the Textures of Non-Equilibrated Crystallizing Media

3.0 Introduction

There are two fundamental factors controlling the textural development of non-equilibrated crystallizing systems, as discussed in Chapter 2. These are the spatial distribution of crystal centres (nucleation, section 2.1) and the degree of interaction between crystals (growth, section 2.2). Any physical model of the textural development of non-equilibrated crystallizing systems must therefore include these factors.

3.1 Previous Models

Previous models of crystallizing systems have been either based on the tessellation of 3-D space (Thompson, 1942) or the use of analytical methods to subdivide space into crystals (Johnson and Mehl, 1939, Avrami, 1939, 1940, 1941). There are a number of problems associated with these approaches.

The tessellation of 3-D space is simplistic and introduces a constraint on the spatial distribution of the crystals because the tessellation of the volume is periodic. This approach is therefore only suitable for the modelling of systems that can reasonably satisfy this constraint, for example highly equilibrated two-phase rocks (Von Bargen and Waff, 1986, Cheadle, 1989). The aim of this thesis is to model texturally non-equilibrated systems, which do not satisfy this constraint (section 2.1). Therefore the tessellation of 3-D space will not be considered further.

The analytical approach has greater applicability to a variety of crystallizing systems as it is based on simple assumptions (section 3.1.1) about the origin and growth of crystals. However this approach (Johnson and Mehl, 1939, Avrami, 1939, 1940, 1941) approximates the impingement of the growing crystals and only produces statistical representations of crystal-size distributions not

actual textures. However, the analytical model as expressed by the Johnson-Mehl-Avrami (JMA) equation clearly describes the main features of a crystallizing system in a simple mathematical form. Therefore considering its derivation (section 3.1.1) will enhance the readers understanding of crystallizing systems.

3.1.1 Derivation of the JMA Model

The derivation given in this section loosely follows that by Kirkpatrick (1981) and begins by stating the physical assumptions made by the JMA model, the validity of which will be discussed in section 3.1.2:

- i) Nucleation of crystals begins at $t = 0$ and the nuclei have a Poisson distribution within the volume V i.e. they are spatially uncorrelated.
- ii) Crystal growth ceases at the points of mutual impingement.
- iii) The growth rate is the same in a given direction for all crystals and depends only on time.
- iv) Crystallization occurs in an infinite melt.

Using these assumptions the following derivation can be made:

First, consider the growth of a single spherical crystal that nucleates at an arbitrary time τ .

The volume of the crystal (V_{crystal}) at a time t later is:

$$[3.1] \quad V_{\text{crystal}} = \frac{4\pi}{3} \left(\int_{\tau}^t Y_t dt \right)^3$$

Where Y_t is the growth rate. Now consider a volume V that is initially all melt and therefore at $t=0$; $V=V_L$, where V_L is the volume of melt. The number of crystals, dn , nucleated in the melt during a small time interval $d\tau$ is:

$$[3.2] \quad dn = V_L I_{\tau} d\tau$$

Where I_{τ} is the nucleation rate per unit volume. Multiplying equations [3.1] and [3.2] gives the total volume crystallized (V_{crystals}) at time t of all the crystals nucleated in the melt during the interval $d\tau$.

$$[3.3] \quad V_{crystals} = \frac{4\pi}{3} V_L I_\tau d\tau \left(\int_\tau^t Y_t dt \right)^3$$

Assuming no impingement of crystals has occurred. Now consider the number of crystals that could have nucleated in the same time interval in the volume previously crystallized (defined as V_s).

$$[3.4] \quad dn' = V_s I_\tau d\tau$$

And similarly:

$$[3.5] \quad V'_{crystals} = \frac{4\pi}{3} V_s I_\tau d\tau \left(\int_\tau^t Y_t dt \right)^3$$

The crystals in this volume are referred to as 'phantom' crystals (Avrami, 1939). The sum of [3.3] and [3.5] gives the instantaneous extended volume ($V_{i_{ext}}$):

$$[3.6] \quad V_{i_{ext}} = \frac{4\pi}{3} V I_\tau d\tau \left(\int_\tau^t Y_t dt \right)^3$$

Where V is the total volume of the system. The total extended volume (V_{ext}) that could have formed from the start of crystallization ($\tau = 0$) to some time later ($\tau = t$) is then given by:

$$[3.7] \quad V_{ext} = \frac{4\pi}{3} V \int_{\tau=0}^{\tau=t} I_\tau d\tau \left(\int_\tau^t Y_t dt \right)^3$$

This volume is larger than the 'true' volume crystallized because it includes the volume of the 'phantom' crystals ($V'_{crystals}$) and the volume of the 'real' crystals ($V_{crystals}$). This means that the

calculations have allowed the crystals to nucleate and grow as if there are no constraints on the positions of the crystals. Although this is non-physical the relationship between the extended volume V_{ext} and the growth and nucleation rates can be used to calculate the 'true' volume crystallized because of assumption i) as will be shown next.

Consider a randomly chosen small region of the volume (V), the 'real' melt fraction ($V_{realmelt}$) at time t is given by:

$$[3.8] \quad V_{realmelt} = \left(1 - \frac{V_{realcrystals}}{V} \right)$$

Where $V_{realcrystals}$ is the 'true' volume crystallized. Now the increase in the 'true' volume crystallized ($V_{realcrystals}$) can be related to the increase in the extended volume (V_{ext}) during a small interval of time dt by assuming that on average:

$$[3.9] \quad dV_{realcrystals} = \left(1 - \frac{V_{realcrystals}}{V} \right) dV_{ext}$$

This means that on average $(1 - V_{realcrystals}/V)$ of the new extended volume will be in the uncrystallized volume. Integrating this gives:

$$[3.10] \quad V_{ext} = -V \ln \left(1 - \frac{V_{realcrystals}}{V} \right)$$

and defining the solid fraction (ϕ) as:

$$[3.11] \quad \phi = \left(\frac{V_{realcrystals}}{V} \right)$$

Combining [3.7], [3.10] and [3.11] give:

$$[3.12] \quad \ln(1 - \phi) = -\frac{4\pi}{3} \int_{\tau=0}^{\tau=t} I_{\tau} \left(\int_{\tau}^i Y_i \right)^3 d\tau$$

Raising both sides to the natural logarithm and re-arranging gives:

$$[3.13] \quad \phi = 1 - \exp \left[-\frac{4\pi}{3} \int_{\tau=0}^{\tau=t} I_{\tau} \left(\int_{\tau}^i Y_i \right)^3 d\tau \right]$$

Which describes the fraction crystallized with time. Kirkpatrick (1981) states that this equation is valid for any variation of the growth and nucleation rates with time. However, the assumptions made in this derivation, specifically 3.1.1 (I), 3.1.1 (ii) and 3.1.1 (iii) are critical to the applicability of this equation.

3.1.2 Discussion of the Assumptions of the Analytical Model

There are several problems with the assumptions of the JMA model. Consider assumption (i) which requires that the nuclei are distributed randomly within the volume. This has no physical basis in most systems because heterogeneous nucleation on existing phases or substrates is commonly accepted as being of primary importance (Hort and Spohn, 1991, Uebele and Hermann, 1996).

Assumption (ii) requires that growth ceases at points of mutual impingement. The interaction between particles and a solid-liquid interface was studied by Uhlmann *et al.* (1964) for non-geologic samples. Uhlmann *et al.* (1964) showed that for particles greater than a few hundred microns in diameter viscous drag forces prevent pushing apart of the interfaces and therefore upon mutual impingement, growth ceases. In view of this, assumption (ii) appears to be valid.

Assumption (iii) that the growth rate is the same in a given direction for all crystals and depends only on time will be invalidated in a three-phase system composed of a liquid phase and two solid phases with different crystal morphologies (Gilbert, 1961), but it is also possible to invalidate the assumption in a two-phase system by assuming continuous nucleation and having a diffusion

controlled growth rate. This means that crystals nucleated at different times have different growth rates because the growth rate depends on the residence time within the melt. Therefore a fast-growing crystal may penetrate through an array of slow-growing crystals and become disconnected or a fast-growing crystal may appear inside an existing slow-growing crystal, overtake it, and surround it (Gilbert, 1961). These problems are a consequence of solving the interaction problem by using 'phantom' crystals and a rule to prevent these occurrences seems to entail analytical difficulties (Gilbert, 1961).

Finally, assumption (iv) that crystallization occurs in an infinite melt is an idealization so that edge-effects may be neglected, crystallization in the central region of a melt volume approximates to this.

3.2 3-Dimensional Numerical Simulation

To address the problems outlined previously a three-dimensional simulation of crystallization has been written in FORTRAN 77. The simulation uses a single physical assumption, equivalent to assumption 3.1.1 (ii) in the JMA derivation, that upon mutual impingement of crystals, growth ceases.

In the simulation, crystal centres are distributed within a three-dimensional simple cubic lattice composed of up to eight million unit cell-like elements or voxels (cubes). Each crystal centre is assigned a number and incremental layers are grown around these nuclei by the addition of voxels. The rate of addition of voxels (growth rate) depends on the problem being modelled (see section 4.1, for a specific example). The crystals are then grown until they interacted with each other to form a complex interlocking three-dimensional texture. The following sections will describe in more detail the construction of this model.

3.2.1 Spatial Partitioning and the Representation of Objects in Three-Dimensions

The representation of solid objects in three-dimensions is a complex topic in computer science and can be split into two broad categories, Boundary Representations and Space Partitioning Representations (Hearn and Baker, 1994). Boundary Representations describe a three-dimensional

object as a set of surfaces separating the interior of the object from its surroundings, Computer Aided Design (CAD) systems tend to use this approach. Alternatively Space-Partitioning Representations describe a three-dimensional object by dividing it into a set of small, non-overlapping, contiguous voxels. Medical imaging systems that require displays of object cross-sections commonly use this type of representation.

A major requirement of the simulation in this study was that measurements made on rocks, such as crystal-size, crystal centre and maximum crystal length could be made on the simulation. Space-partitioning representation is the natural choice for a model with these requirements because such quantities are easily calculated by counting voxels.

3.2.2 The Model Algorithm

A 3-D cubic lattice (see fig. 3.1, a & b) was created as a three-dimensional array of voxels, each with an associated x, y, z 'world' co-ordinate and an integer value. The state of a voxel (melt or crystal) is defined by the integer value, which is zero for melt and a positive integer when within a crystal. All voxels in the lattice were initially assigned the value zero to represent a volume of melt. A number of 'world' co-ordinates were then chosen to represent the centres of the crystals and these voxels were assigned numbers from one up to the maximum number of crystals. The spatial distribution of these crystal centres could be varied from randomly ordered to highly ordered depending on the problem being studied. Once a distribution of crystal centres was prescribed they could be grown into crystals by the addition of voxels in layers around the crystal centre.

The fundamental problem when simulating a crystallizing medium is the correct calculation of the impingement between individual crystals. In figure 3.2a two lath shaped crystals with their crystal centres lying in the same plane are shown impinging, crystal one should not grow through crystal two if the assumption that growth ceases upon mutual impingement was applied. The outline drawing shows the protruding part of crystal one if this assumption was relaxed and crystal one had been allowed to grow through crystal two. The insets show a two-dimensional analogue of this example. Figure 3.2b shows the same two crystals but in this example crystal two has a faster growth rate than crystal one and has grown around it. There is no correct two-dimensional analogue of figure 3.2b if the assumption that growth ceases upon mutual impingement is applied because a

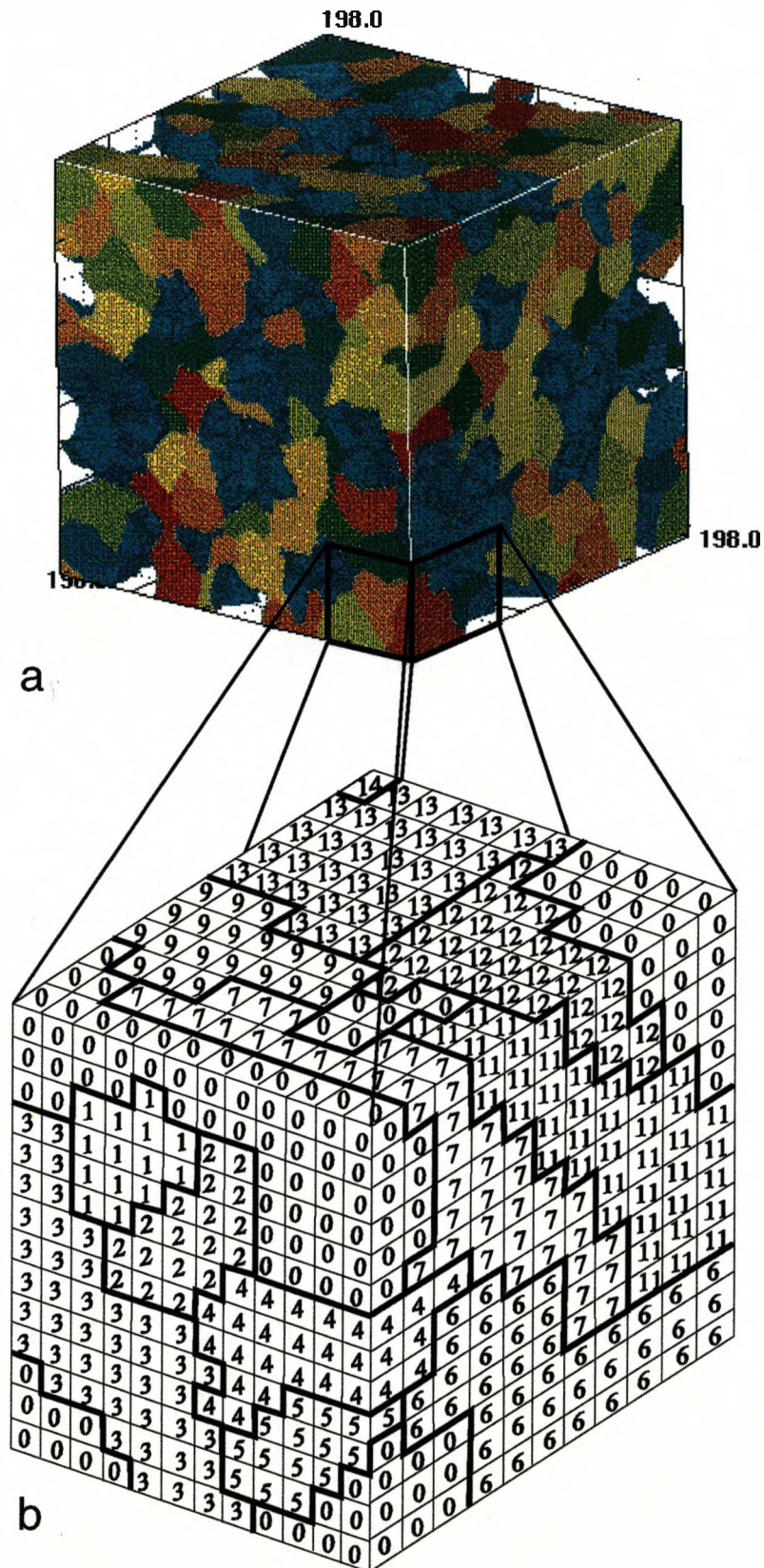


Figure 3.1a Visualization of the results of the model. The volume contains 900 crystals, whose ideal morphology is cube-shaped, that have interacted to form a complex microstructure in which individual crystals are represented by different colours. The volume has had some crystals removed to give an impression of the three-dimensional shape of the individual crystals. Figure 3.1b Schematic of a small region of the visualized volume (fig. 3.1a) showing individual voxels each with an integer value. The dark lines high-light the boundaries between individual crystals.

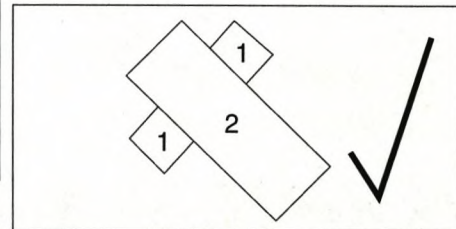
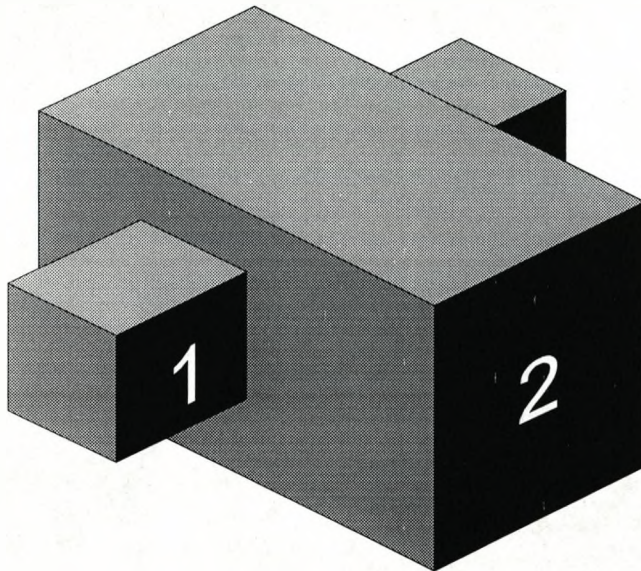
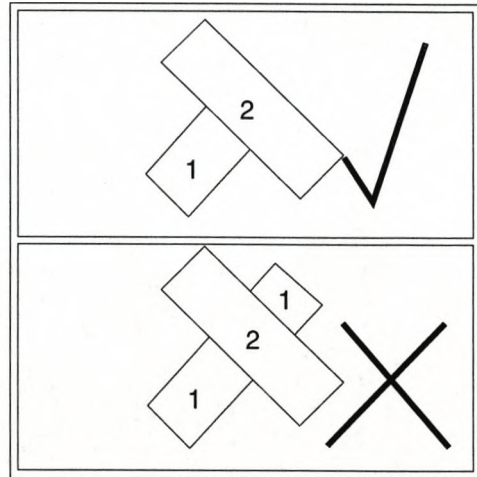
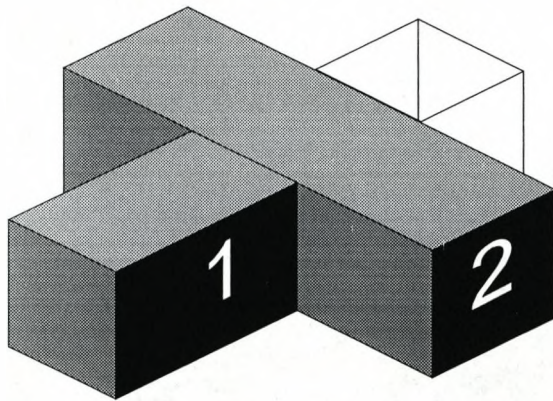


Figure 3.2a Diagram of the impingement between two lath shaped crystals with their crystal centres lying in the same plane. Crystal one will not grow through crystal two if growth ceases upon mutual impingement. The outline drawing shows the protruding part of crystal one if this assumption is relaxed. The growth rates of both crystals are equal. The inset shows a 2-D diagram of the same impingement relationship (tick mark indicates that growth ceases upon mutual impingement).

Figure 3.2b Diagram of the impingement between two crystals with their crystal centres lying in the same plane, where the growth rate of crystal two is greater than that of crystal one. Crystal two has therefore grown around crystal one in 3-D. The inset shows a 2-D diagram of the same impingement relationships (tick mark indicates that growth ceases upon mutual impingement).

section through the crystals (fig. 3.2b inset) would appear to be paradoxical when compared to the example shown in fig. 3.2a inset. This illustrates that the growth and interaction problem is inherently three-dimensional and that a two-dimensional simulation would be incorrect. Therefore a method for calculating the growth (section 3.2.2.1) and the cessation of growth upon impingement (section 3.2.2.2) is required in three-dimensions.

Growth and interaction between crystals can be conceived as competing processes. *Ceteris paribus*, a single crystal growing within a melt has, by definition, an *ideal morphology* (section 3.2.2.1), if other crystals are present then this morphology may be modified due to the constraints on space caused by the growth of the other crystals. The result of this competition between crystals leads to, by definition, a *space-filling morphology* (section 3.2.2.2).

3.2.2.1 Ideal Morphology

Consider the growth of a crystal with an ideal morphology. The crystal is defined mathematically in its own 'local' co-ordinate system with the central point representing the nucleus of the crystal. The shape of the crystal is then defined by generating the vertices of the crystal (see fig. 3.3), specified as points using standard spherical co-ordinates. Each axis of the crystal is initially scaled to produce the appropriate morphology, i.e. cube, plate, lath, etc. and the whole crystal is then scaled proportionally by the number of growth increments required. Scaling is a simple mathematical transformation (Hearn and Baker, 1994). For example, a uniform scaling simply changes the size of an object and can therefore be used to represent crystal growth and a non-uniform scaling can be used to change a cube to a plate or a lath.

The result of these processes is a representation of the crystal in terms of its nucleus and vertices whose central point could then be transformed (see Hearn and Baker, 1994, for details of transformations and rotations) to its corresponding 'world' co-ordinate position, a rotation being applied to the vertices in the 'world' co-ordinate system if required. The advantage of this approach is that each different crystal type is only defined once, as a centre and its corresponding vertices, in its own 'local' co-ordinate system, yet can have many orientations and locations within the 'world' melt volume (see fig. 3.4 inset). Next a three-dimensional wire-frame model (see fig. 3.4) of the

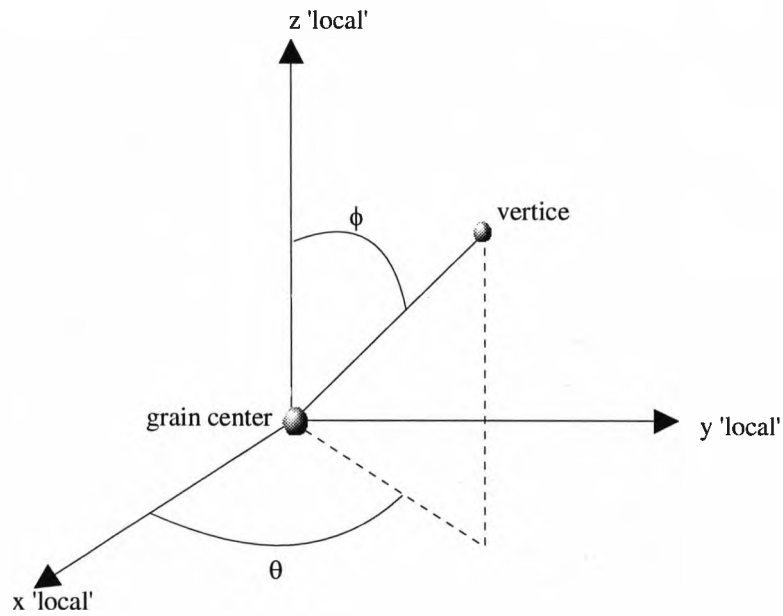


Figure 3.3 Relation of vertice to grain centre defined by standard spherical co-ordinates in a 'local' coordinate system.

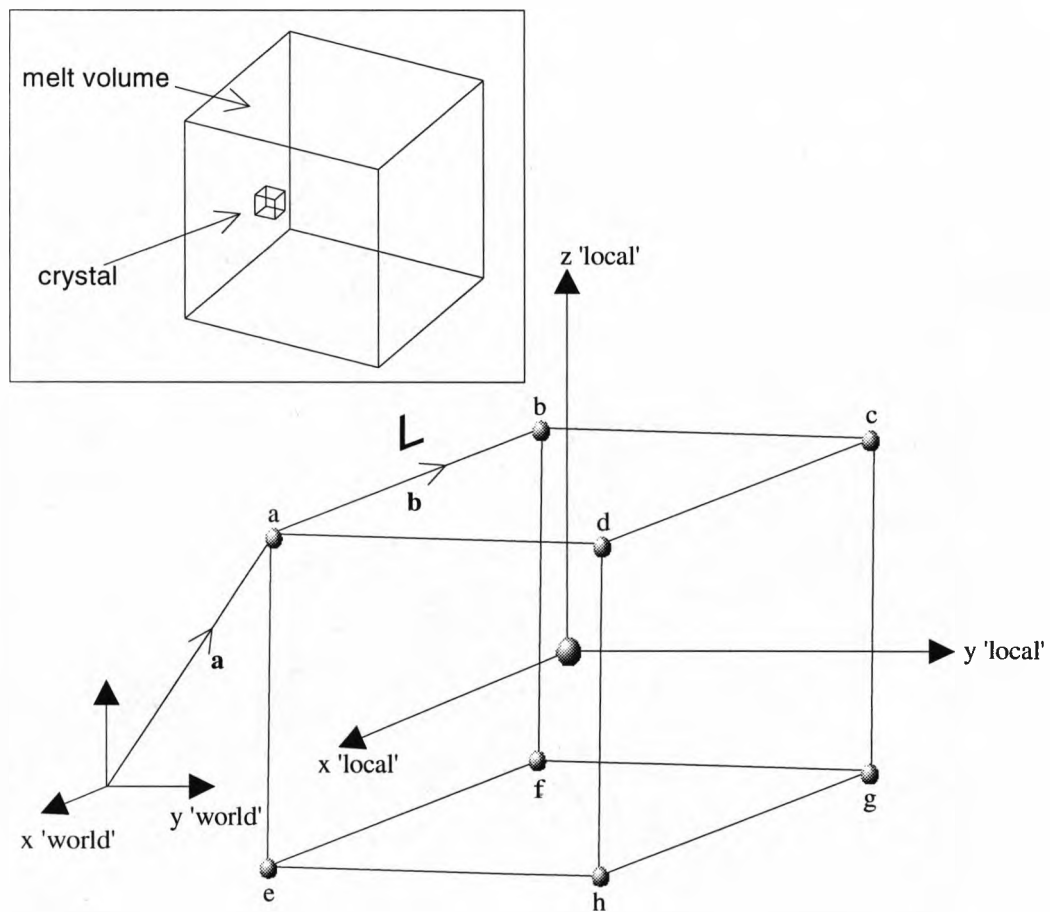


Figure 3.4 Three-dimensional wire-frame model of grain showing relation of 'local' coordinate system to 'world' coordinate system. Inset shows crystal within melt volume.

crystal in the 'world' co-ordinate system is created using parametric line equations to join the vertices (see eq.[3.14]).

$$[3.14] \quad \mathbf{r}(t) = \mathbf{a} + t\mathbf{b} \quad 0 \leq t \leq 1.0$$

Where $\mathbf{r}(t)$ is the position vector of a point on the edge L which joins the vertices 'a' and 'b', where \mathbf{a} is the position vector of the vertice 'a' relative to the 'world' co-ordinate origin and \mathbf{b} is the position vector of the vertice 'b' relative to vertice 'a'. The value t is called the parameter of the representation and defines the distance along vector \mathbf{b} from vertice 'a' (see figure 3.4). The other edges between pairs of vertices are defined similarly relative to the 'world' co-ordinate origin. This results in a wire-frame model of the crystal (figure 3.4) defined by the parametric line equations in the 'world' co-ordinate system (inset figure 3.4). Finally, a spatial-partitioning (solid) representation of the crystal was created by serial-sectioning the crystal and area-filling the resultant polygons (see fig. 3.5). This generated a three-dimensional crystal composed of voxels (see fig. 3.6) which in this example would have an *ideal morphology*. It should be noted that the use of parametric line equations reduces the complexity and increases the speed of the area-fill algorithms, as the parametric equations reduce the amount of processing required to de-limit the polygon shape. This is because it is possible to represent the wire-frame of an object (see fig. 3.4) as a series of line segments (see fig. 3.7a) with a unique number of vertices (see fig. 3.7c-e), as opposed to the standard method of defining line segments in terms of their end-points which mean that each vertice is defined twice (see fig. 3.7b). Figure 3.8 is a simple two-dimensional example of this. It can be seen that using the standard way of defining a line by the co-ordinates of its end-points' results in vertice A being specified twice, once on edge AB and once on edge AD. Therefore before area-filling this shape, the vertices must be sorted and duplicate points removed. Using the parametric line equations, however, it is possible to define the shape without duplication of the vertices. This is achieved by specifying the parameter t in by an inequality as shown in figure 3.7c-e.

The next section will consider how crystals interact with each other to form a *space-filling morphology*.

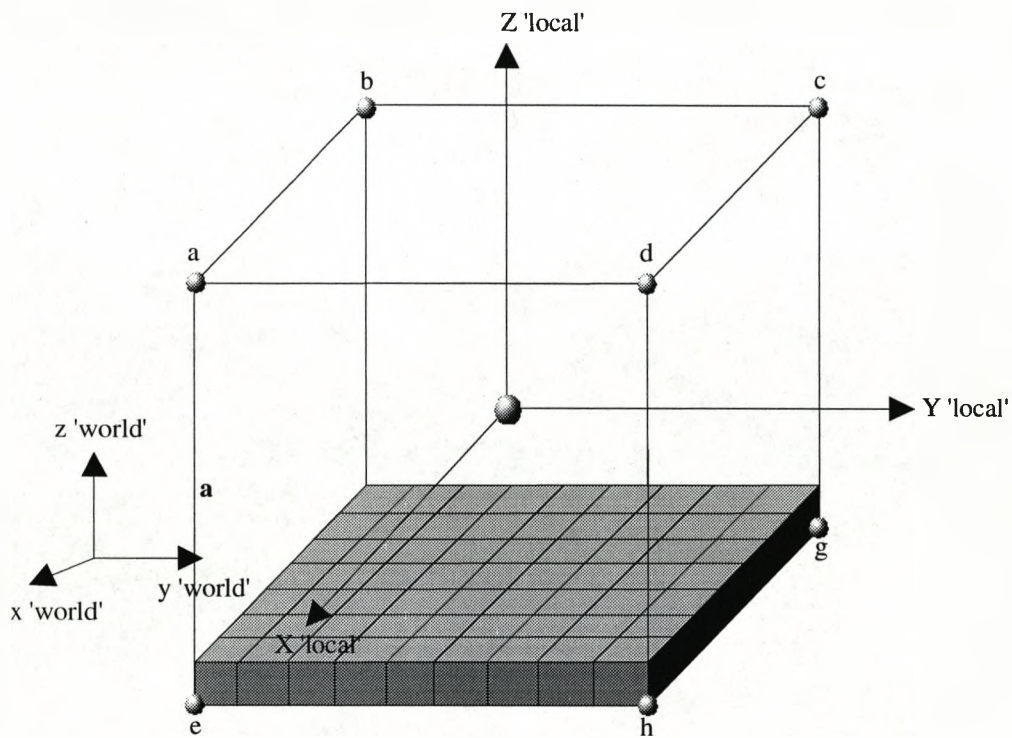


Figure 3.5 Area-fill of the polygon defined by the intersection of vertices with X-Y plane in the 'world' coordinate system.

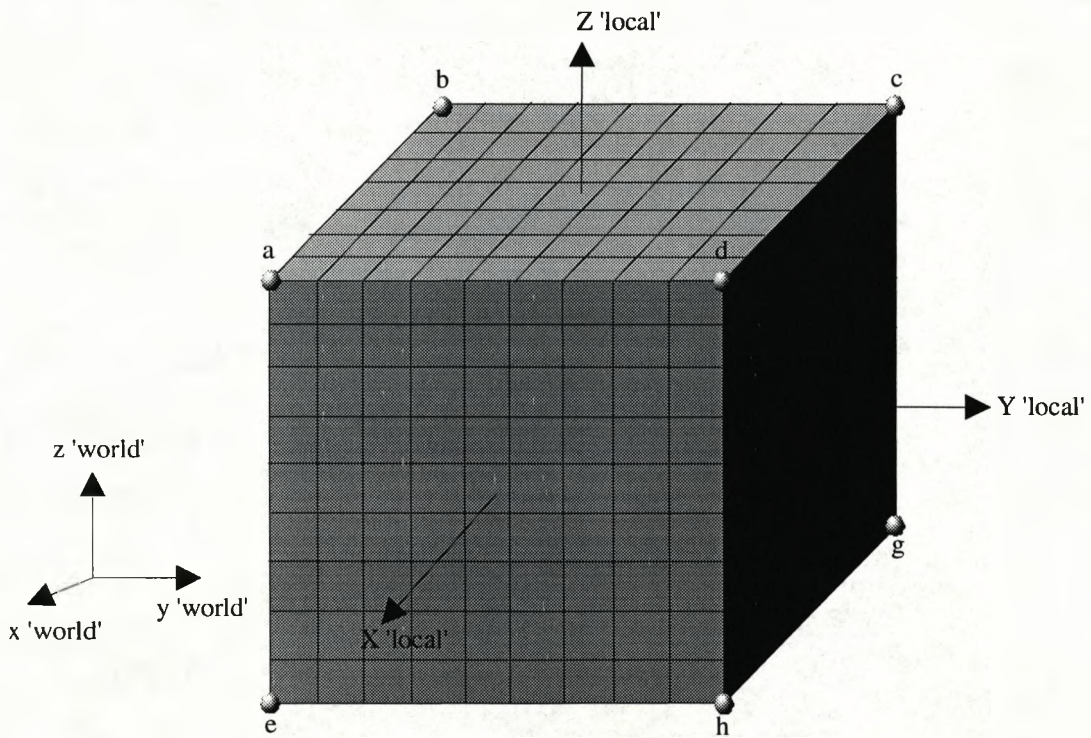


Figure 3.6 3-D grain volume composed of nine polygons generated by the area-fill method of fig. 3.5. This crystal has an *ideal morphology*.

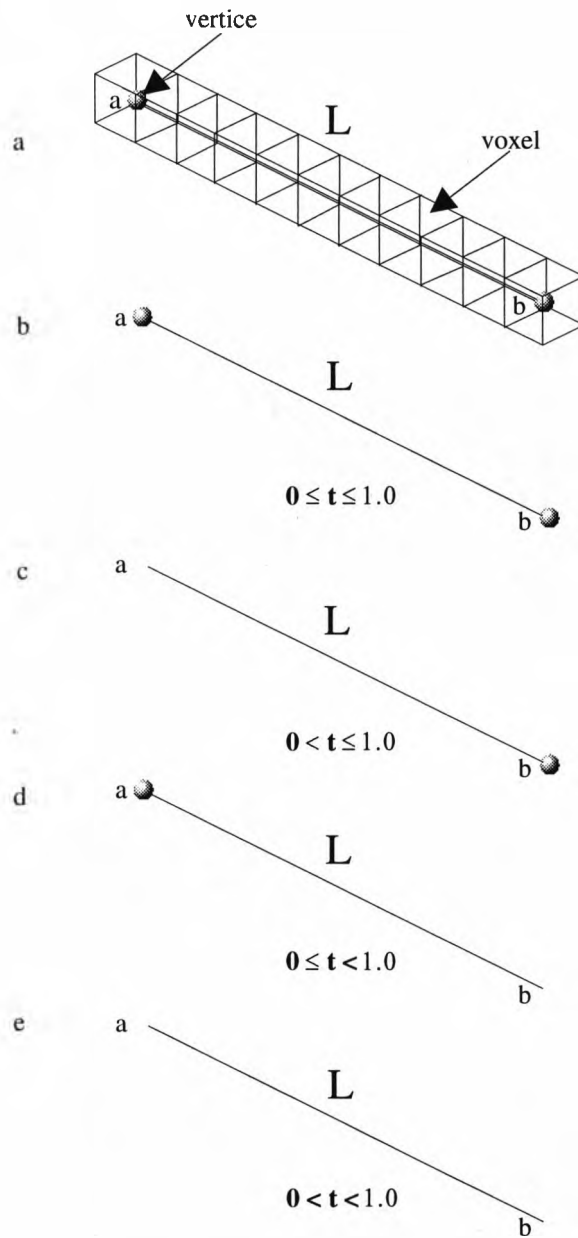
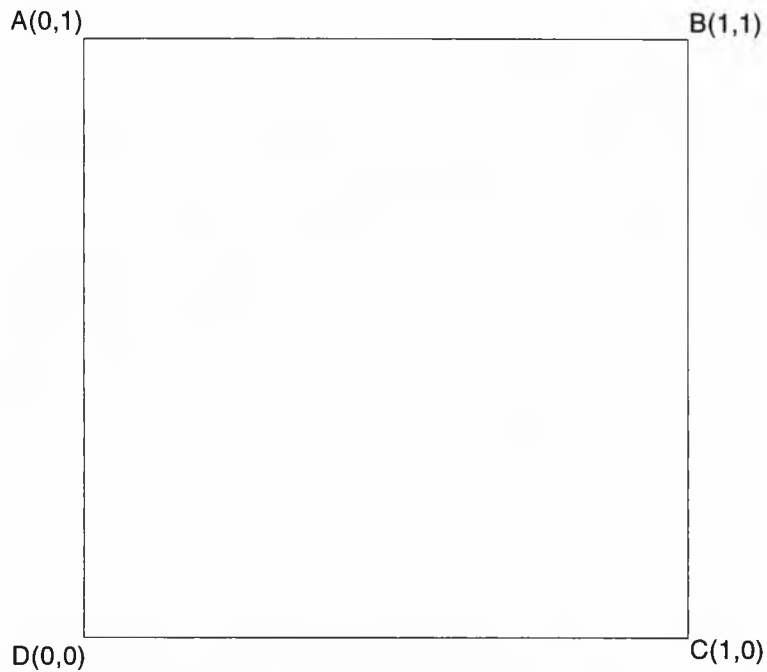


Figure 3.7a Line segment showing vertices and corresponding voxel representation of the line.

Figure 3.7b Standard representation of the line segment with two vertices allocated.

Figure 3.7c-e Line segments showing how variation of the parameter t can be used to allocate the number and location of vertices.



Edge List (standard notation)

A to B=(0,1) to (1,1)

A to D=(0,1) to (0,0)

note: point A defined twice in edge list

Edge List (parametric notation)

A to B= $r_{ab}(t)$ $0 \leq t \leq 1$

A to D= $r_{ad}(t)$ $0 \leq t \leq 1$

note: point A only defined once in edge list

Figure 3.8 Diagram showing the comparison between the standard and parametric notations for the edges of a shape.

3.2.2.2 Space-Filling Morphology

The best way to describe how the crystals interact with each other is to consider an analogy with the quantum mechanical phenomena of barrier tunnelling (Halliday & Resnick, 1988). If you look into a partially filled glass of water that is tilted so that total internal reflection is occurring at the surface of the glass. The glass wall looks silvery and nothing can be seen through it. If you press your moistened thumb against the outside of the glass, the ridges on your finger become visible. This is because the light waves are penetrating a few wavelengths beyond the interface because the incident wave needs to 'feel out' whether there is actually an interface there. Similarly, the ideal crystal morphology (see 3.2.2.1) is analogous to the 'feel out' of the wave; it describes the potential for the existence of the crystal and can be used to 'feel out' whether there are any other crystals within this region. To implement this, the algorithm calculates the ideal crystal morphology for the next increment about a crystal centre. This generates all the voxels that could potentially belong to a crystal about that crystal centre (see fig. 3.9) delimited by the wire-frame joining the vertices. Then, if the voxels that lie adjacent to the crystal centre are assigned the same value as the crystal centre voxels, a new layer is accreted around that crystal centre. Figure 3.9 shows the initiation of this accretion process. The process is repeated until either there are no more potential crystal voxels left (ideal morphology, see fig. 3.6) or any further accretion is impeded by other crystals (space-filling morphology, see fig. 3.10). To reduce the computation time growth increments on crystals (ideal morphology) that have no space in which to grow are not calculated, however, other crystals may still have space to grow and the accretion process is repeated for these crystals until the required degree of crystallization of the 'world' volume has occurred producing a three-dimensional, solid model of the interacting crystals.

The model 'world' melt volumes produced by this simulation are composed of eight million voxels. This means that each simulation generates approximately 32MB of binary output data. If the evolution of a crystallizing medium with one hundred growth increments was modelled this would generate 3.2GB of data for a single model alone. This poses considerable data storage problems and therefore to reduce the amount of data storage required, each simulation is run until the model volume is fully crystallized, to produce, by definition, a *Grain Volume* (see fig 3.11a). The grain

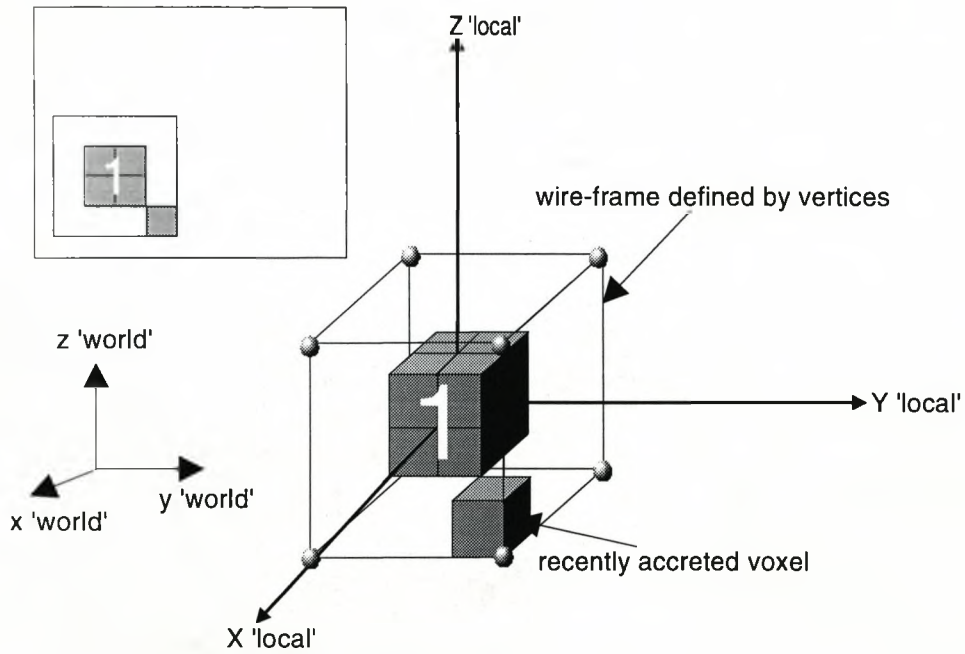


Figure 3.9 Diagram of crystal centre 1 with recently accreted voxel lying within potential crystal volume (*ideal morphology*) delimited by the wire-frame. Inset is view along Z-axis.

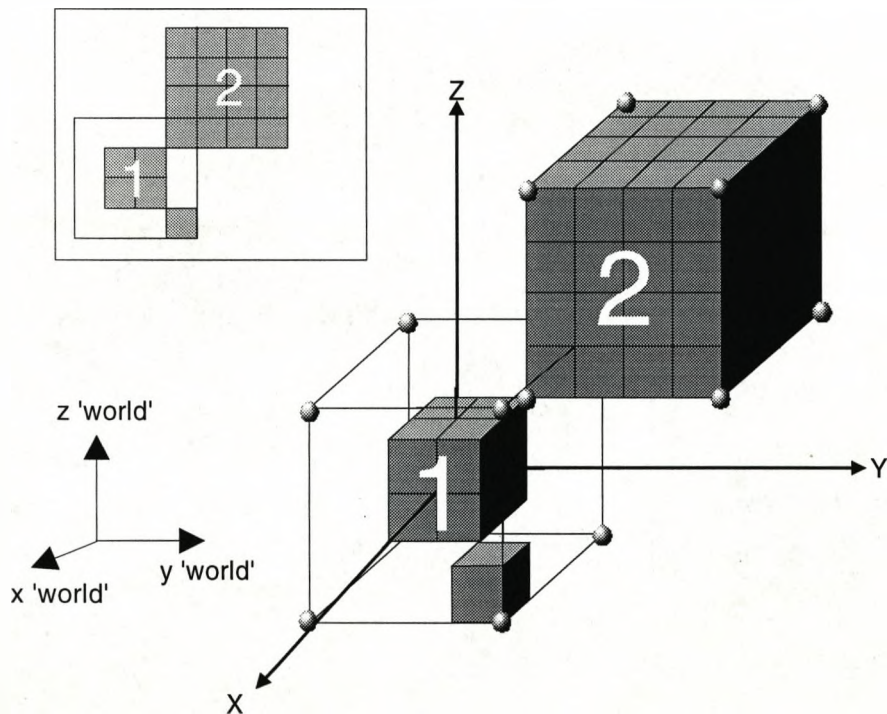


Figure 3.10 Diagram of the potential crystal volume of crystal centre 1 impinging on pre-existing crystal 2. This will result in an *ideal morphology* for crystal 2 and a *space filling morphology* for crystal 1. Inset is view along Z-axis.

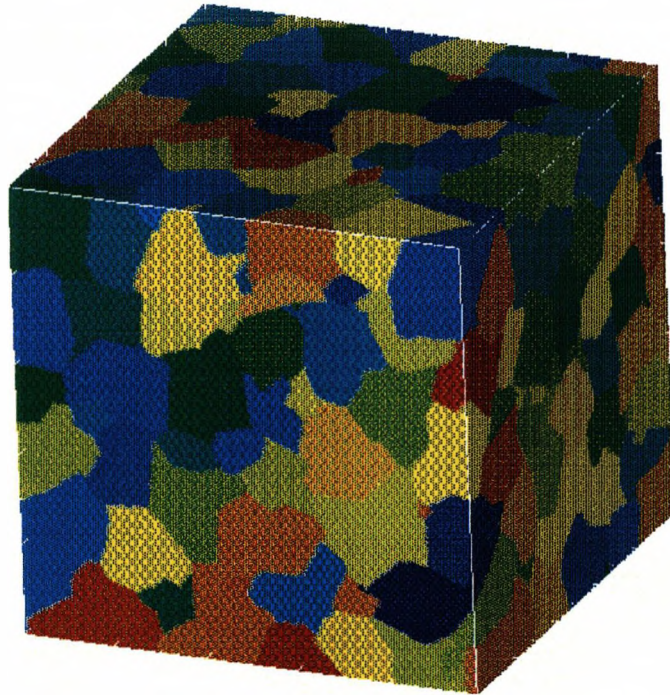


Figure 3.11a Visualisation of a fully-crystallized model (*Grain Volume*). This volume contains 395 crystals with a cube-shaped ideal morphology with individual crystals displayed as different colours (differentiation of crystals in image is restricted due to limited colour palette on workstation).

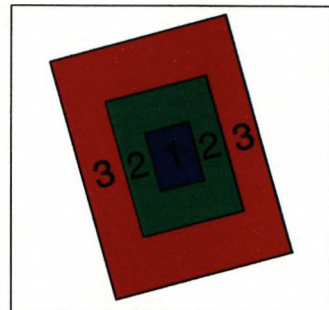
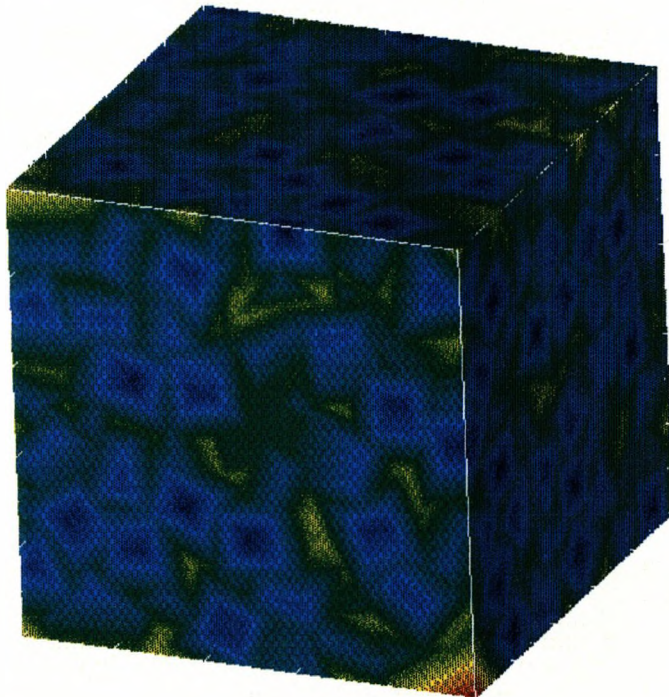


Figure 3.11b Visualisation of a fully-crystallized model (fig. 3.11a) with 100 growth increments (*Increment Volume*). Blue colours represent early growth increments near the centre of crystals and red colours represent late growth increments. Limited colour palette on workstation prevents display of individual increments. Inset shows labelled increments for a single crystal.

volume records all the interaction surfaces of all the crystals during the simulation. Each crystal being defined by a region of voxels of constant positive integer value, as shown previously in figure 3.1b. A modified version of the simulation, which numbers all the growth increments at a given time on all the crystals with the same positive integer value is then applied to this grain volume. This results in, by definition, an *Increment Volume* (see fig. 3.11b) which holds all the increment growth information of each of the crystals within the simulation. The inset in figure 3.11b shows a two-dimensional example of the labelled increments for a single crystal for clarity. Combination of the information from the grain volume and the increment volume allows the recreation of the evolution of the whole crystallizing medium. This reduces the data storage requirements from 3.2GB to 64MB for each model.

3.2.3 Problems with the Model

A major problem with this model is that it is impossible to represent the real world exactly with a digital representation (Serra, 1982). In practice, however, the resolution or approximation to reality of a digital simulation can be improved by increasing the number of voxels per unit volume. This is equivalent to the process of increasing the resolution of a computer screen whereby the number of pixels per cm^2 is increased. For example, consider figure 3.12a this is a schematic showing growth increments on two impinging crystals. The 'w' shaped impingement interface caused by the interaction of the different growth vectors is shown by a dark-line. When the resolution within the simulation is low (fig. 3.12b) the interface is composed of a jagged line and much of the detail is lost. In comparison, figure 3.12c is a high resolution simulation of the interaction between the two crystals and it can be seen that the interface is a much closer representation of figure 3.12a.

Obviously, the amount of computer memory (RAM) constrains the total number of voxels and hence the resolution achievable within the simulation. On the heavily loaded shared resource of an Ultra-Sparc station at Liverpool University this effectively limits the number of voxels within the simulation to eight million (~64MB RAM). As a consequence the resolution of the simulation depends on the size chosen for the physical volume that is represented by the eight million voxels. Unfortunately, this means that there can be conflicts between measurements on the simulation that require high resolutions, such as the decrease in porosity with crystallization and measurements that

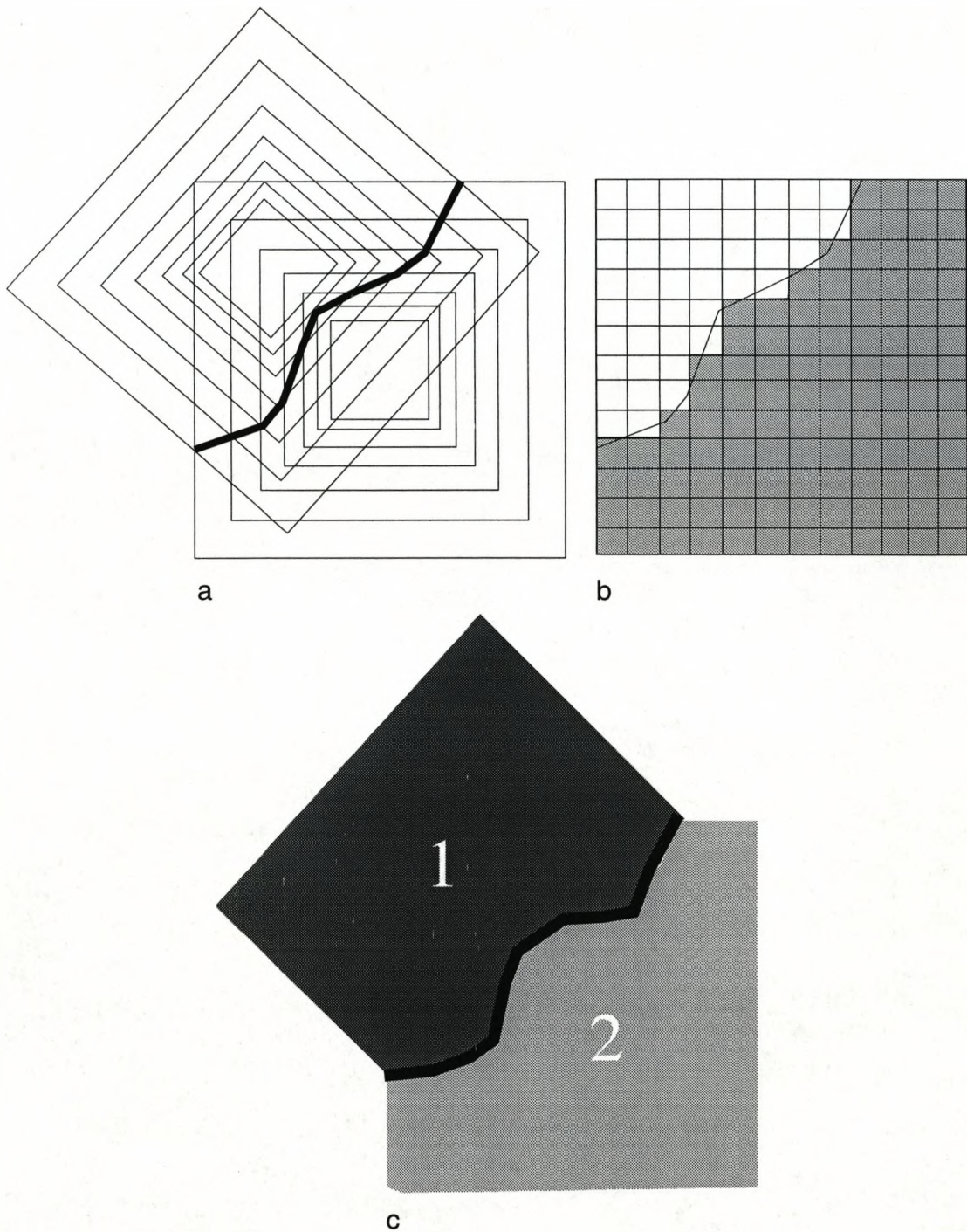


Figure 3.12a Diagram showing growth increments of both crystals. The thick dark line marks the impingement boundary between the crystals defined by the points of intersection between growth increments of similar age.

Figure 3.12b Low resolution digital representation of fig. 3.12a showing jagged interface between crystals.

Figure 3.12c High resolution simulation of fig. 3.12a.

require large physical volumes such as the measurement of porosity itself in a heterogeneous medium (see Chapter 6, section 6.1.1).

3.3 Application of the Model to the Crystallization of Rocks

The simulation described previously is a general model of crystallization based on the single assumption that crystal growth ceases at the points of mutual impingement. To simulate the crystallization of rocks it is necessary to make some further assumptions about the growth of crystals in rocks. The following paragraphs will outline these assumptions and discuss their validity.

3.3.1 Assumptions of the Model for Crystallizing Rocks




There are two additional constraints applied to the model to simulate the crystallization of rocks:

- i) Growth is faster than dissolution and re-precipitation and therefore the crystals are faceted.
- ii) The range of faceted crystal morphologies present in nature can be approximated by rectangular prisms of varying aspect ratio such as cubes, laths and plates.

These assumptions can be justified as follows;

- i) The majority of crystals present in rocks exhibit a faceted morphology.
- ii) The aspect ratios chosen cover the range of the most common rock forming minerals as shown in table 3.1. Although it is possible to model more realistic multi-faceted crystals using the simulation, this would currently increase C.P.U time prohibitively, but as faster computers become available this assumption can be relaxed.

Table 3.1 Aspect Ratios of Common Rock Forming Minerals

Mineral	Model representation	Graphic (not to scale)
olivine, quartz	cube	
plagioclase	lath	
mica	plate	

3.3.2 Removal of Edge-Effects

When making measurements on any finite sample, for example, a simulation or rock thin-section, care must be taken to prevent the finite size of the sample biasing the results. There are two approaches to this problem within the context of a simulation. Periodic boundary conditions can be applied to the model or a sub-set of the simulated volume that is unaffected by edge-effects can be used. The latter approach is followed throughout this thesis as it allows simulations where edge-effects are desirable, such as crystallization from a substrate to be modelled. It will be assumed that consideration of a sub-set of the total volume that is half a crystal length within the total volume for all boundaries (fig 3.13) is sufficient to reduce the edge-effects caused by the lack of crystallizing crystals external to the total 'world' volume. Further justification for this assumption is given in Chapter 6, section 6.1.1 in relation to the measurement of porosity.

3.4 Testing the Model

A major difficulty with the numerical simulation of problems is how to ascertain that the model is correct. There are two main approaches to this, comparison with an analytic solution and comparison with experimental data:

3.4.1 Comparison with an Analytic Solution

The JMA equation can be used for this test as it provides a numerical solution for the volume fraction crystallized with time for a random distribution of initial crystal centres. To compare the JMA equation to the simulated results, the fraction crystallized with time in a volume of the model that has had the edge effect removed was measured. Figure 3.14 is a plot of the simulated volume fraction crystallized with time for three models each composed of 900 crystals with a cube-shaped ideal morphology (coloured lines on plot). The crystals in each of the cases have a random spatial distribution of initial crystal centres that were all nucleated at time zero. All the models show a sigmoidal plot of volume fraction crystallized with time that closely matches the curve produced by the JMA equation (black solid line on plot) with similar initial conditions. The sigmoidal shape of

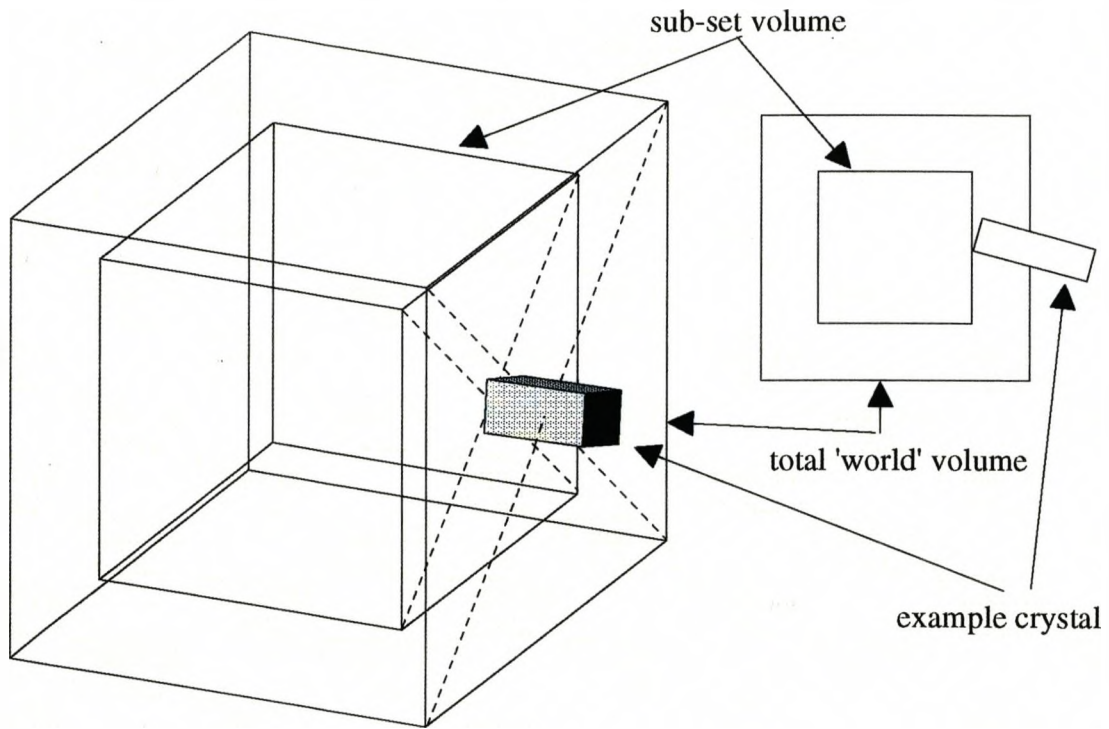


Figure 3.13 Diagram of the removal of edge-effects by considering a sub-set volume that is half a crystal length within the total 'world' volume for all boundaries. Inset shows plan view.

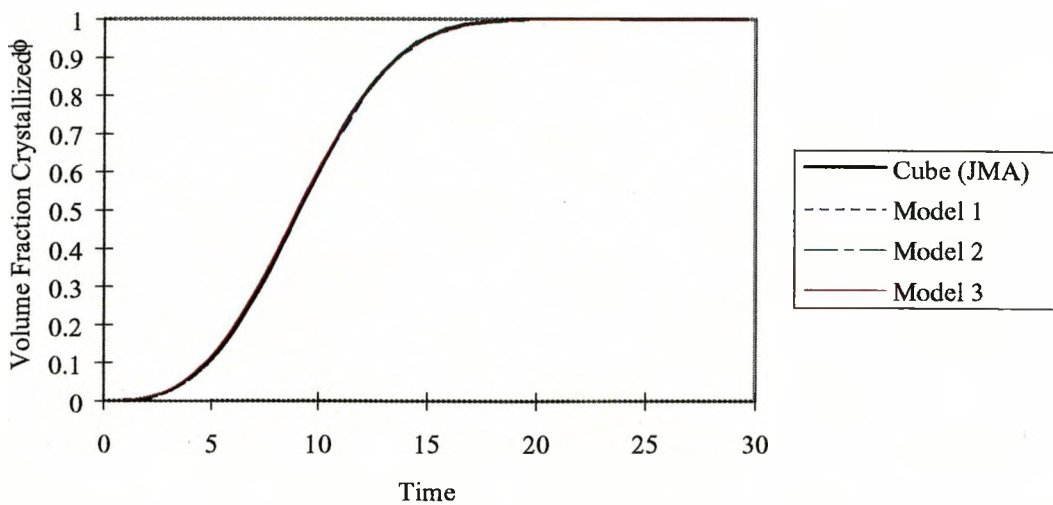


Figure 3.14 Plot of simulated volume crystallized with time compared with analytic solution (JMA equation) for the case of 900 crystals with a cube-shaped ideal morphology and a random distribution of crystal centres nucleated at time zero.

the plot is due to the combination of two effects, in the case of instantaneous nucleation. The rate of crystallization is initially slow, but then increases rapidly because the volume of the crystals is proportional to the cube of the growth rate. However, eventually the rate of crystallization decreases as impingement between crystals dominates. The results show that the model correctly predicts the volume fraction crystallized with time for crystals with a cube-shaped ideal morphology and that any edge-effects have been minimized.

3.4.2 Comparison with Experiment

Chapter 4 presents a comparison of the results of the simulation with measurements on equilibrated rock textures (Elliott and Cheadle, 1997, Elliott et al., 1997) and Chapter 6 presents a comparison between permeabilities calculated for the simulation and experimental measurements.

3.5 Conclusions

A new three-dimensional model of the development of textures in crystallizing systems has been presented in this chapter. It is a significant improvement on previous analytic models because it produces a physical representation of the textures and can easily simulate many different crystallizing systems. The following is a summary of the major conclusions of this chapter:

- A new 3-D voxel-based simulation of the evolution of textures in unequilibrated crystallizing systems has been developed.
- Capable of modelling:
 - Any nuclei distributions.
 - Any nucleation rate.
 - Any crystal shape.
 - Anisotropic crystal growth rates.
 - Multiple phases of crystallization.

Chapter 4

Textural Equilibrium in Rocks

4.0 Introduction

The identification of textural equilibration in rocks can provide important information about the physical conditions and processes that affected the rocks during their formation (Hunter, 1987; Kretz, 1966). A texturally equilibrated rock is one in which the surface topology of its grains is in mechanical and thermodynamical equilibrium. If it is assumed that the constituent crystals of a monomineralic rock are isotropic in terms of their surface energy, then for it to be in textural equilibrium it must satisfy the following requirements. First, groups of three grains must intersect along an edge and four edges must intersect at a point. Second, at the junction of three grains, the angle between the tangents of the grain boundaries must equal 120° . This angle is called the dihedral angle (Smith, 1948) (see fig. 4.1a). Third, all grain faces must be minimum energy surfaces and therefore have constant mean curvature.

The current practice for assessing whether a monomineralic rock is texturally equilibrated is simply to ascertain if the dihedral angles are 120° (Hunter, 1987; Kretz, 1966). The dihedral angle is determined by measuring apparent dihedral angles in thin section (Smith, 1948). These apparent dihedral angles must vary between 0° and 180° because of the thin-sectioning process, which must inevitably cut randomly oriented grain edges at different angles. The measured angles are plotted as a cumulative frequency curve and compared to the curves expected for populations of constant dihedral angles (Riegger and Van Vlack, 1960; Harker and Parker, 1945). If the curves match, the rock is assumed to be texturally equilibrated, and if not, it is assumed to be unequilibrated. However, if the curves do not match, little can be deduced about the degree of textural equilibration, because the shape of the curve expected for an entirely unequilibrated texture is unknown. It is possible that geometric effects due to crystal shape and nuclei distribution may generate an apparent dihedral angle curve for a completely unequilibrated texture that is similar to the curve expected for an

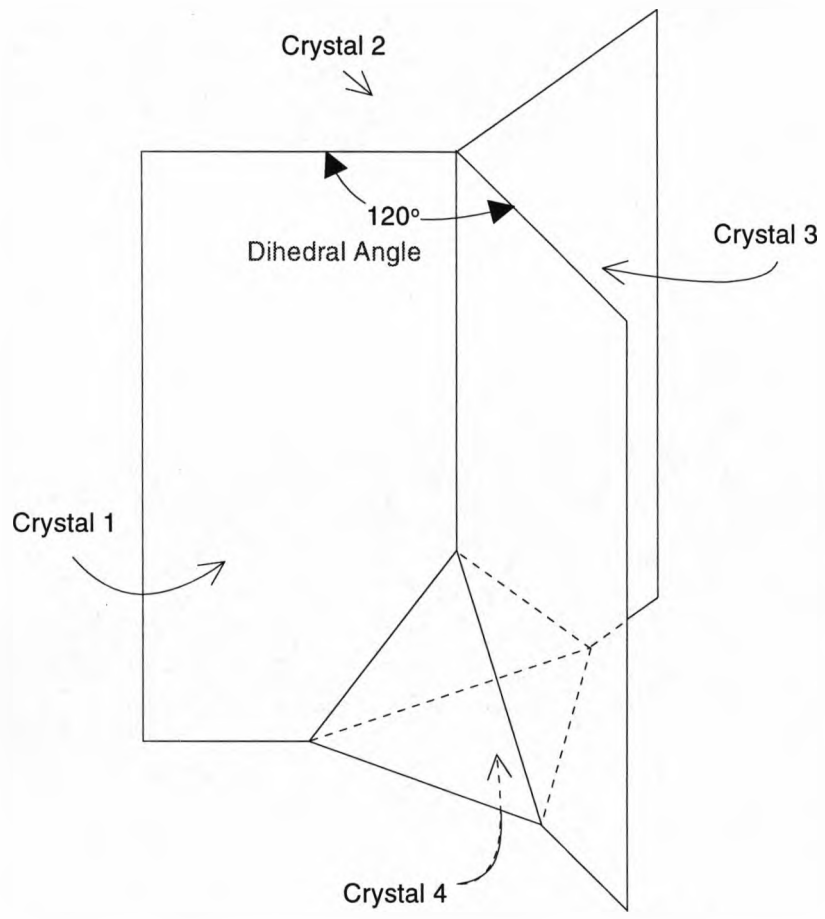


Figure 4.1a Diagram of the relationship between four isotropic crystals in a monomineralic rock showing an example of a 120° dihedral angle (after Cheadle (1989)).

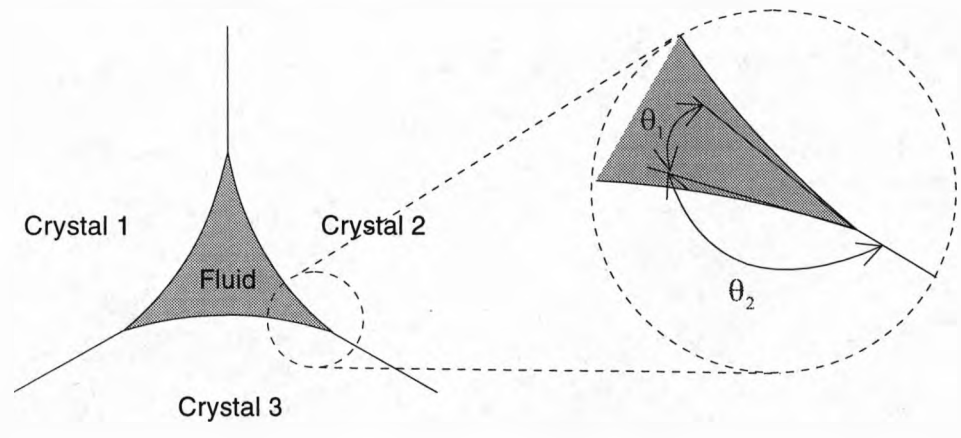


Figure 4.1b Diagram of the dihedral angles at a solid-fluid interface. θ_1 and θ_2 are the dihedral angles in the solid-fluid system, where θ_1 is the angle between tangents to the grain boundaries, measured in experimental determinations of fluid-solid dihedral angles.

equilibrated rock. If this is true, then the method of measuring dihedral angles to test for textural equilibration may be fundamentally flawed.

The first aim of this chapter is to present apparent dihedral angle curves for fully crystallized, monomineralic, totally unequilibrated textures. These curves together with the existing curves for totally equilibrated textures are the two end members that encompass the range of apparent dihedral angle curves that may be expected from textures that vary from totally unequilibrated through partially equilibrated to totally equilibrated. The relative position of a measured apparent dihedral angle curve within this range allows a quantitative statement to be made about the degree of equilibration in the rock from which the measurements were taken. This can be achieved by defining an index of fit (Stickels and Hucke, 1964) and assuming a continuum between the end-member cases.

The second aim of this chapter is to present apparent dihedral angle curves for partially crystallized, unequilibrated textures to compare with the corresponding curves for equilibrated textures. If the crystalline phase is assumed to be isotropic in terms of surface energy, then the presence of a fluid or second phase means that an equilibrated rock will exhibit three different dihedral angles; 120° at solid-solid-solid triple junctions, and two different dihedral angles at solid-solid-fluid triple junctions corresponding to the angle between the solid and fluid phases and the angle between the solid phases (see fig. 4.1b). The dihedral angle between the solid and fluid phase is often measured in experimental determinations of fluid-solid dihedral angles (Holness and Graham, 1991; Waff and Bulau, 1982; Watson and Brenan, 1987). Comparison of the curves for the apparent dihedral angles between the solid and fluid phases in an unequilibrated texture with the predicted curves for a corresponding equilibrated texture will show whether it is possible to mimic the effect of equilibration of the dihedral angle by purely geometric effects. This is likely because at a closed, triangular pore, bounded by three crystal faces, the apparent dihedral angles are constrained to add up to 180° (fig. 4.2a) and this constraint must affect the distribution of measured angles. The question of whether dihedral angles in unequilibrated textures can mimic those in equilibrated textures has important implications for the recognition of the ability of a rock to transport melt or other geologic fluids. For example, the modelling of the distribution of melt under isotropic equilibrium conditions (Beere, 1975; Von Bargen and Waff, 1986; Cheadle, 1989) suggests that if

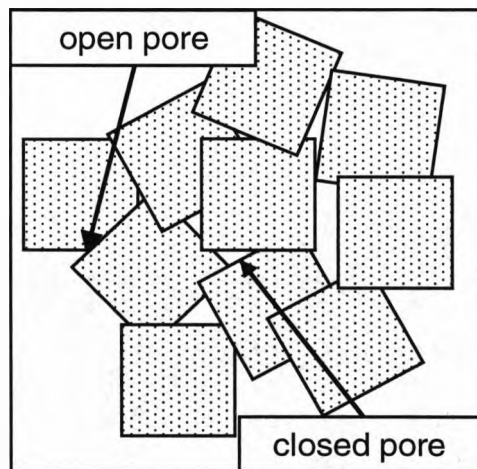


Figure 4.2 Two-dimensional schematic section of partially crystallized rock with square crystals, showing open and closed triangular pores.

the dihedral angle between the solid and liquid phases is less than 60° , then the rock is permeable down to vanishingly small porosities (see fig. 4.3 a and b).

4.1 Three-Dimensional Numerical Simulation

The best method to generate apparent dihedral angle curves for totally unequilibrated textures is to use three-dimensional numerical simulations of crystallizing rocks that permit no textural equilibration (see Chapter 3). These simulations are more useful than real rocks because the simulations allow controlled examination of the effect of parameters such as nuclei distribution and crystal shape and because of the difficulty in assessing whether a real rock is actually totally unequilibrated.

The three-dimensional numerical simulations reported here are simple computer models of growing, interacting crystals. To generate a three-dimensional texture, nuclei were distributed within a three-dimensional cubic lattice composed of 8×10^6 cell-like elements or voxels; the number of voxels is a compromise between adequate resolution and calculation time. Incremental layers of voxels were added to each nucleus, in a random order, to simulate a progressive, linear growth in the dimensions of the crystals. This was equivalent to assuming that the rate of volume growth of the crystal was proportional to its surface area. The crystals were grown until they interacted with each other to form a complex, interlocking three-dimensional texture (fig. 4.4a). Three main assumptions are implicit in the simulation; the first is that the crystal morphology could be approximated by rectangular prisms of various aspect ratios. This assumption was made to reduce the computational complexity of the simulation, but can be justified because after a certain amount of crystal impingement has occurred very little of the original crystal morphology is apparent. The second assumption is that when the crystals impinged on each other, growth at the contact was stopped. This is likely to be realistic because the diffusion rate of atoms to the contact would be decreased because of restricted access to the melt. The third assumption is that no equilibration of the texture occurred. This simply means that the growth rate of the crystals is assumed to be faster than the rate of solution and reprecipitation. This assumption was required to produce an unequilibrated texture and means that dissolution effects are neglected.

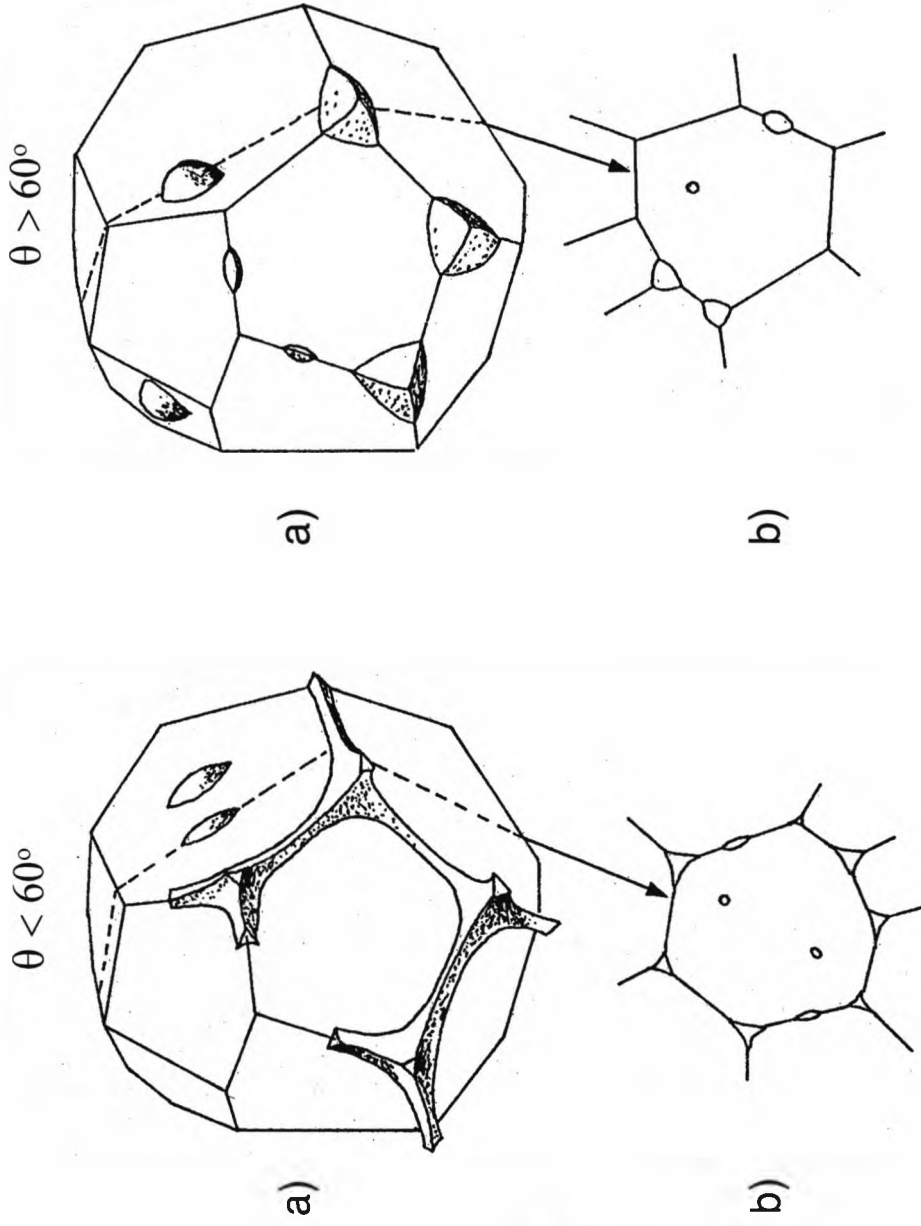


Figure 4.3a Examples of texturally equilibrated three-dimensional fluid topologies around a single crystal. Isolated fluid pores on the crystal faces are equilibrium geometries, but are metastable relative to the pores at crystal corners. For convenience, the figure for $\theta < 60^\circ$ only shows fluid on some of the edges. All of the edges would in fact, be covered.

Figure 4.3b Two-dimensional sections through these topologies (after Cheadle, 1989).

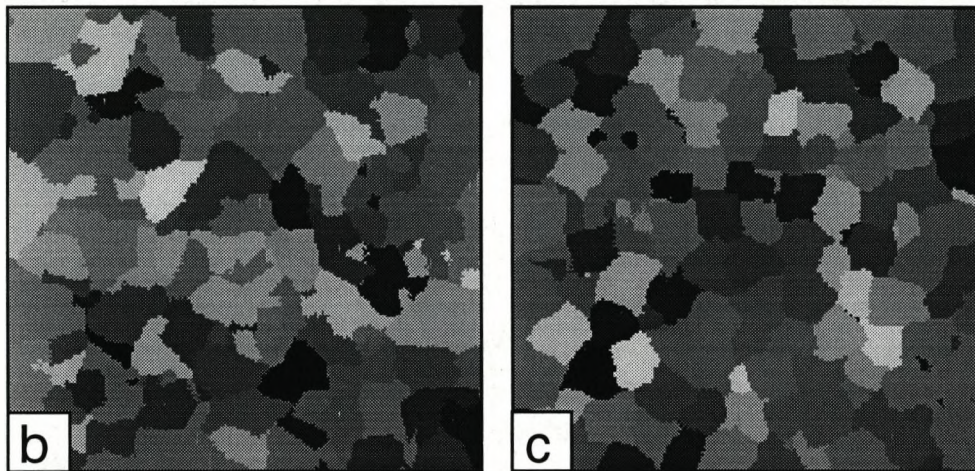
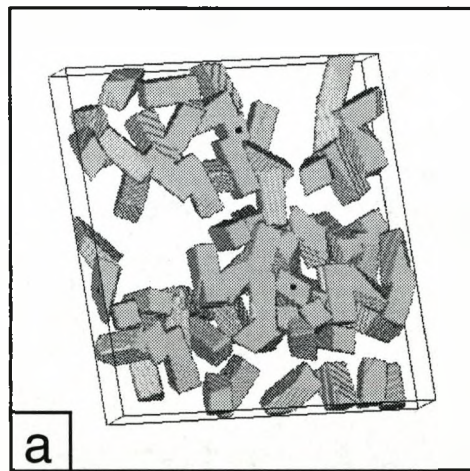


Figure 4.4 a: Example of three-dimensional cross-section showing lath shaped crystals produced by the numerical simulation. b: Two-dimensional section through three-dimensional simulation of fully crystallized texture with clustered nuclei distribution. c: Two-dimensional section through three-dimensional simulation of fully crystallized texture with dense randomly packed gravitationally settled nuclei distribution.

The simulation allows control over all the major factors involved in the textural evolution of an unequilibrated rock, such as nuclei distribution, nucleation rate, growth rate, and crystal morphology, and therefore allows the effects of these factors on the apparent dihedral angle distributions to be quantified. The simulation contained 200 crystals and was run with 4 different nuclei distributions; i.e. a random nuclei distribution with an instantaneous nucleation event, a random nuclei distribution with a linear nucleation rate, a clustered nuclei distribution which was generated by removing clumps of nuclei from a dense, randomly packed distribution of touching spheres (Finney, 1968), and a settled nuclei distribution corresponding to a dense, randomly packed distribution of touching spheres (Finney, 1968): both of these last two with an instantaneous nucleation event. The aspect ratio of the crystals was varied from cubes (1:1:1) to laths (3:1:1) because most crystal forms lie within this range. Growth rate was kept constant in all the simulations because, as the crystals were growing simultaneously, variation in the growth rate would have no effect on the interference boundaries between crystals.

The three-dimensional simulations were sectioned to allow comparison with measurements made on rock thin sections. A three-dimensional cross section through a volume of the simulation can be seen in figure 4.4a. This cross section and the two-dimensional sections (fig. 4.4, b and c) were created by calculating the intersection of a randomly oriented plane with the crystals within the three-dimensional simulation. Close examination of the two-dimensional sections shows that the crystal boundaries are jagged, being defined by a series of squares, each of which is a two-dimensional section through a three-dimensional voxel. The apparent dihedral angles were determined by assuming that the crystal boundaries were smooth curves joining the midpoint of the side of each voxel that is adjacent to a voxel of another crystal. It was assumed that the expected random error due to measurement was insignificant (Stickels and Hucke, 1964).

4.2 Results

4.2.1 Fully Crystallized Textures

Measurements of the apparent dihedral angles in the two-dimensional sections from the simulations were plotted as a graph of cumulative per cent frequency versus apparent dihedral angle. The results for the fully crystallized (0% porosity) textures can be seen in figure 4.5. The thin grey s-

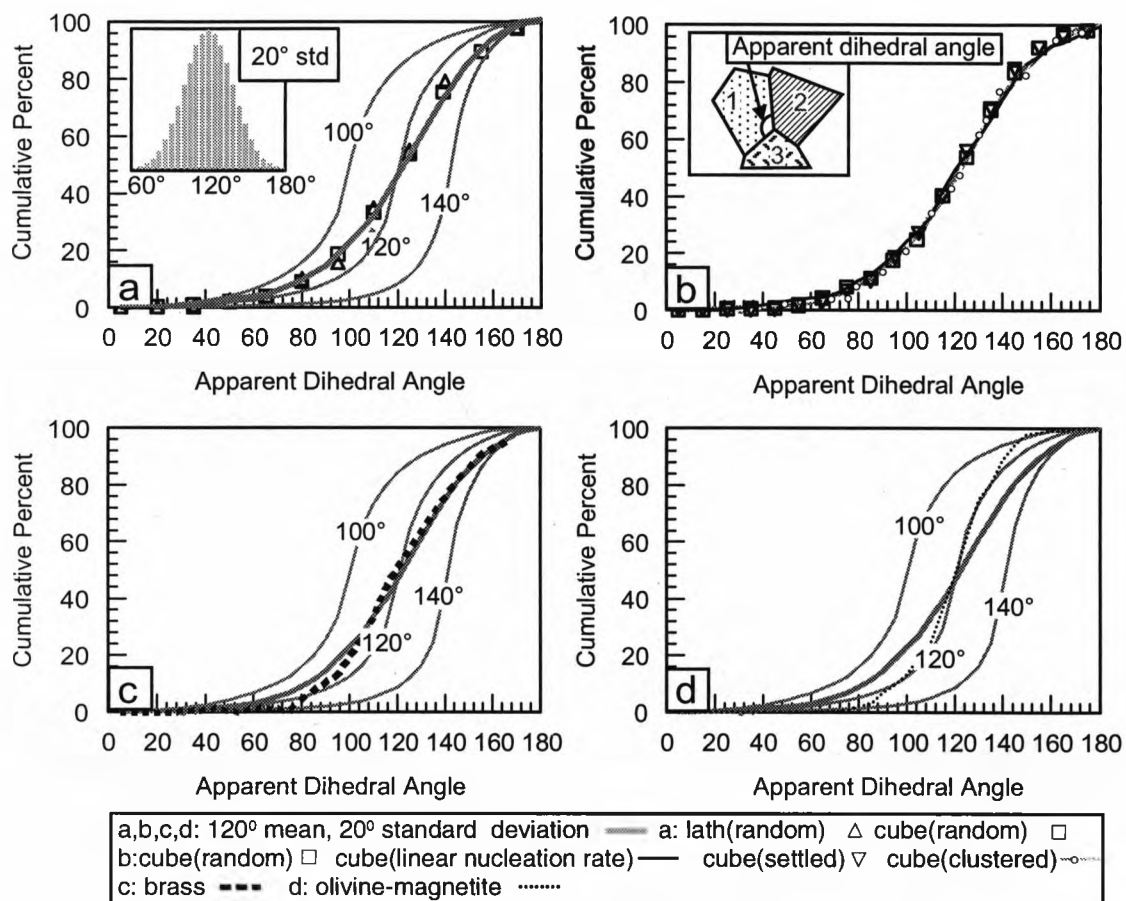


Figure 4.5 Apparent dihedral angle distributions for fully crystallized textures. In all plots, the labelled light grey curves are theoretical apparent dihedral angle distributions for equilibrated textures. Inset in a is bar chart showing normal distribution of true dihedral angles with mean of 120° and standard deviation of 20° to indicate variation in true dihedral angles corresponding to curve shown on cumulative percent frequency plots of apparent dihedral angles. Inset in b is schematic of apparent dihedral angle. Other curves are labelled in the key.

shaped curves are the theoretical distributions of apparent dihedral angles in thin section corresponding to a given dihedral angle as calculated by Riegger and Van Vlack (1960).

Figure 4.5a shows the apparent dihedral angle distributions for textures formed from growing cube (1:1:1) shaped crystals and by growing lath (3:1:1) shaped crystals with an initial random distribution of nuclei. These curves are almost identical and are similar to curves produced by sectioning a normal distribution of dihedral angles with a standard deviation of 20° about a median dihedral angle of 120° (thick grey line; inset in fig. 4.5a). The apparent dihedral angle curves for textures generated by growing cube shaped crystals with differing nuclei distributions are shown in figure 4.5b. They all have a median dihedral angle of 120° and are very similar, showing that the distribution of apparent dihedral angles is largely independent of the nuclei distribution and the nucleation rate. Figure 4.5c shows a comparison between the best fit line to the curves for the unequilibrated textures (thick grey line) and 100 apparent dihedral angle measurements made on a specimen of brass annealed for 1 hour at 500°C (Harker and Parker, 1945). This short period of annealing means that equilibration had only just begun and therefore that this sample is a good natural example to compare to the simulated unequilibrated textures. The curve for the brass corresponds to a curve for a normal distribution of dihedral angles with a mean of 120° and a 20° standard deviation, and shows the same general trend as the curve for the unequilibrated texture reported here. This result confirms that the numerical simulation reproduces realistic unequilibrated textures. The minor differences between the curve for the brass sample and for the simulated unequilibrated textures may be due to a small amount of equilibration that may have occurred in the brass sample.

Figure 4.5d shows a comparison between the apparent dihedral angle curves for equilibrated textures, and unequilibrated textures and the measured apparent dihedral angle distribution from an apparently equilibrated rock sample. This sample is an olivine-magnetite adcumulate from the Freetown complex, Sierra Leone (fig. 4.6) and 160 dihedral angle measurements were made on olivine-olivine-olivine triple junctions in order to reduce the errors associated with measurement (Riegger and Van Vlack [1960] reported that 100 measurements gave an accuracy of $\pm 4^\circ$). The adcumulate shows some deviation from the curve for an equilibrated texture with a dihedral angle of 120° , apparently having too few low and high angles. This apparent truncation of the distribution is

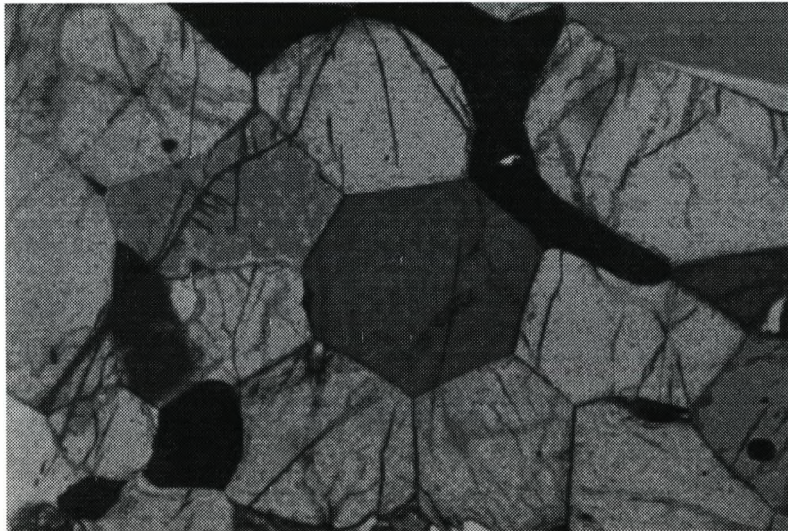


Figure 4.6 Photomicrograph of olivine-magnetite adcumulate from Freetown complex, Sierra Leone. Single-phase boundaries between olivine grains are clearly visible. Horizontal field of view is 4 mm (Courtesy of R. Hunter).

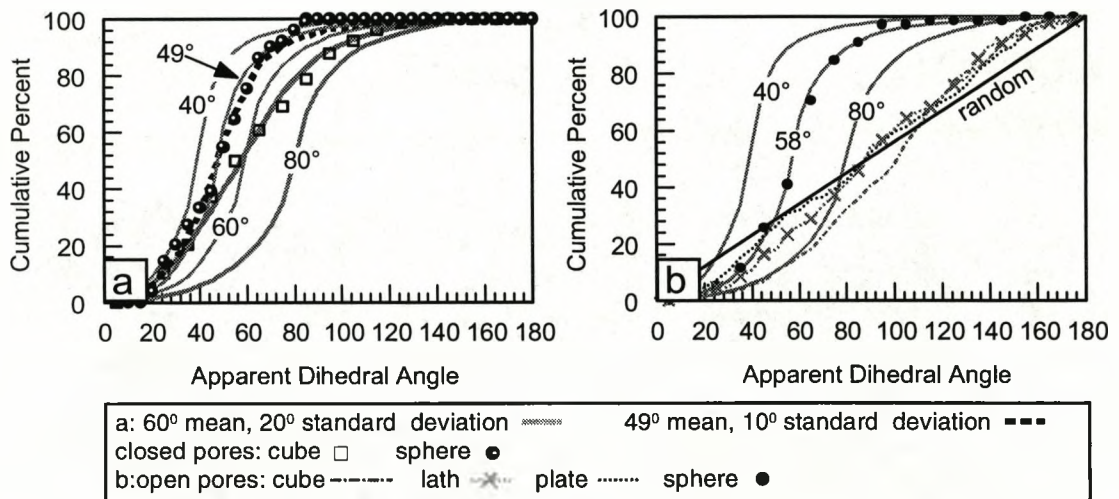


Figure 4.7 Apparent dihedral angle distributions for partially crystallized textures. a shows curves for closed pores and b shows curves for open pores. In all plots, the labelled light grey curves are theoretical apparent dihedral angle distributions for equilibrated textures. The curve in b, labelled random, is apparent dihedral angle curve for randomly orientated sections through randomly distributed intersecting planes. Other curves are labelled in key.

often seen in reported apparent dihedral angle curves (Hunter, 1987; Holness and Graham, 1991), and is a consequence of the difficulty of recognizing these angles in thin section. The low and high angles are difficult to recognize because they result from highly oblique sections across the three grain junctions. In these cases one of the crystals will be extremely small and thus easy to miss, and the grain boundaries will be extremely blurred, because the section is several micrometers thick. Despite this, the similarity of the curve for the natural sample to the predicted curve for an equilibrated texture appears to confirm that equilibrated textures can be distinguished from unequilibrated textures by dihedral angle measurements provided careful measurements are made. It should be noted, however, that the ability to measure the high and low angles is not a problem if measurements are made using the universal stage microscope (Kretz 1966; Vernon, 1968, 1970, Elliott *et al.*, 1997a, Elliott and Cheadle, 1997b). Unfortunately, this approach has been neglected recently, probably because it is very time consuming.

4.2.2 Partially Crystallized Textures

The partially crystallized textures were generated using a random distribution of nuclei; crystallization was stopped once the porosity had been reduced to 30%. The effects of different nuclei distributions were not examined, because nuclei distribution was thought to be relatively unimportant based on the results for the fully crystallized textures, and because crystallization was not allowed to go to completion. Grain shape was varied and several simulations were run for crystal shapes ranging from spheres to plates.

The results for the partially crystallized simulations were split into two groups because there were two different solid-fluid geometries: those associated with closed triangular pores bounded by three crystal faces and those associated with larger open pores bounded by four or more crystal faces (fig. 4.2a). In figure 4.7a the thin, grey s-shaped curves are the distribution of apparent dihedral angles in thin section for equilibrated textures, calculated by Riegger and Van Vlack (1960), and the thick grey curve is the apparent dihedral angle curve for a normal distribution of dihedral angles with a 20° standard deviation about a mean of 60°. The squares denote the apparent dihedral angle distribution measured at closed (triangular) pores in a simulated texture composed of 200 randomly distributed 1:1:1 aspect ratio (cube shaped) crystals. It can be seen that the curve corresponding to a

normal distribution with a mean of 60° and a 20° standard deviation is a reasonably good fit to the data. The open circles denote the results for triangular pores between spherical crystals. The median of the curve is 49° and it is very similar to the corresponding curve for an equilibrated texture. It can be modelled by a normal distribution of dihedral angles with a mean of 49° and only 10° standard deviation.

The curves given in figure 4.7b are from measurements made on (open) pore spaces bounded by more than three crystal faces for simulations using different crystal shapes. The straight line labelled random was generated by calculating dihedral angles from randomly oriented sections through randomly distributed intersecting planes. This generated the expected distribution of apparent dihedral angles from open pore spaces, if no geometric factors were introduced by the shape of the growing crystals. Three of the curves in figure 4.7b are for apparent dihedral angles measured at solid-fluid junctions in open pores for different aspect ratio rectangular prisms. The curve for cubic crystals (1:1:1) shows the greatest deviation from the random line. The other curves approach the random line as the aspect ratio of the crystals increases through lath-shaped (3:1:1) crystals to plate-shaped crystals (30:30:1). A curve of apparent dihedral angles measured from open pore spaces generated by the impingement of spherical crystals is also plotted in figure 4.7b and it is very similar to the curve for an equilibrated texture with a dihedral angle of 58° .

4.3 Discussion

4.3.1 Fully Crystallized Textures

The most important result of this study is that apparent dihedral angle distributions measured from both simulated and natural unequilibrated monomineralic textures are similar to, but are distinguishable from, the predicted apparent dihedral angle curve for equilibrated textures with a dihedral angle of 120° . Hence, in theory, careful measurements of apparent dihedral angles can be used to recognize textural equilibrium. However, the curves for unequilibrated textures have median values of 120° , illustrating that measurements of the median dihedral angle from apparent dihedral angle curves are insufficient to determine whether a sample is texturally equilibrated. The curves for unequilibrated textures are more similar to those for equilibrated textures than to the curve for

randomly oriented grain edges, because each growing crystal has a particular shape with fixed angles between faces and with edges that are not randomly distributed. Hence the geometry of the impinging crystals reduces the potential variability of the dihedral angles. The similarity of the curves for unequilibrated textures and equilibrated textures also illustrates the danger of assuming that measured curves which only slightly deviate from the predicted curves for equilibrated textures are explained by a range of true dihedral angles due to crystalline anisotropy, or by the sample not quite having reached equilibrium. This study clearly shows that such curves may be measured from totally unequilibrated textures, in which case they provide no information about the value of the equilibrium dihedral angle for a rock.

The results of the simulation also show that the measured distribution and median values of the apparent dihedral angles in unequilibrated textures are largely independent of the nuclei distribution and the nucleation rate, although these factors have a fundamental influence on the final appearance of the texture. For example, the clustered nuclei distribution (fig. 4.4a) generates a large variation in grain size and is therefore a less-equilibrated texture than the equigranular texture generated using the more ordered distribution of nuclei (fig. 4.4b). This example of two textures showing different degrees of textural equilibration at the crystal size scale, yet having the same dihedral angle distribution, illustrates another problem with using dihedral angles to determine textural equilibration. Small-scale textural re-equilibration at crystal junctions leading to a constant dihedral angle is likely to be a more rapid process than whole-scale Ostwald-Ripening; thus a rock may be texturally equilibrated at different length scales, and dihedral angle measurements only reveal equilibrium at a relatively small scale.

4.3.2 Partially Crystallized Textures

The apparent dihedral angle curves for closed, triangular pores in unequilibrated textures are s-shaped and similar to those for triangular pores in equilibrated textures (fig. 4.7a). The curves are crystal-shape-dependent, with curves derived from measurements made on spherical crystals producing smaller median angles and a much closer fit to the curves for equilibrated textures than similar curves derived from measurements made on cube-shaped crystals. This is to be expected because a spherical crystal has a more texturally equilibrated shape than a rectangular prism, but it

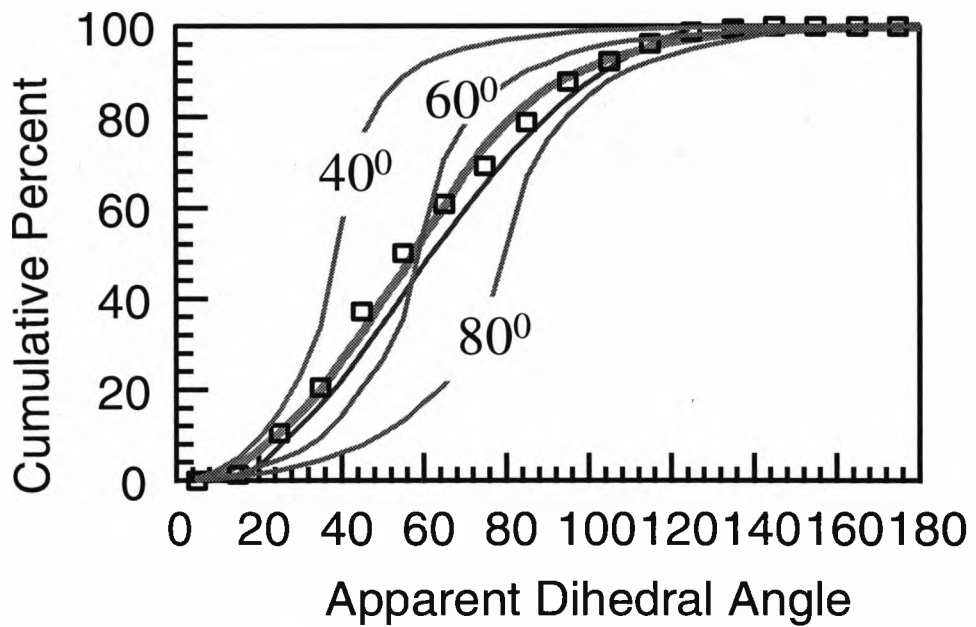
also suggests that the more faceted and equant the crystal shape, the closer the measured curve will approach the curve for an equilibrated texture.

The results obtained from examining open pores (those bounded by more than four crystals) further illustrate the influence of crystal shape on the apparent dihedral angles of unequilibrated partially crystallized textures. The apparent dihedral angle curve for spherical crystals approximates the expected curve for an equilibrium texture with a dihedral angle of 58° , but the curves for prismatic crystals are less s-shaped and become closer to approximating an entirely random distribution of angles as the crystals become more plate like. In a natural unequilibrated rock, multifaceted equant crystals would produce apparent dihedral angle curves that are more similar to those for equilibrated textures.

An important result is that the apparent dihedral angle curves for closed (triangular) pores and for open (non-triangular) pores in unequilibrated textures are significantly different, the curves for closed pores being more similar to the predicted curves for equilibrated textures. This reveals that, unless the rock is totally equilibrated, the measurement of closed (triangular) pores will give results different from the measurement of open (non-triangular) pores because of geometrical factors due to crystal shape. Watson and Brenan (1987) measured the dihedral angles of triangular pores in the systems quartz+H₂O and olivine+H₂O and assumed that these systems represented equilibrium melt geometries in the crust and mantle respectively. However, comparison of their data with the results from measuring dihedral angles in closed pores in a simulation composed of cube-shaped crystals show a marked similarity (fig. 4.8). This suggests that the systems under consideration may not have been equilibrated.

4.4 Conclusions

This chapter has investigated some of the controls on the apparent dihedral angles of fully crystallized, unequilibrated monomineralic rocks and partially crystallized rocks using a three-dimensional numerical simulation to generate suitable textures. The main conclusion is that totally equilibrated textures produce apparent dihedral angle distributions that cannot be mimicked by unequilibrated textures. However, the unequilibrated textures produce apparent dihedral angle curves that are similar to many reported curves previously suggested to indicate equilibrated textures with



Model \square

Quartz + H₂O ---

Olivine + H₂O ---

} Watson & Brenan, 1987

Figure 4.8 Apparent dihedral angle distributions for partially crystallized textures. This plot is a comparison between a simulated (model) un-equilibrated texture and two 'equilibrated' textures from Watson and Brenan (1987). The grey curves are the theoretical apparent dihedral angle distributions for equilibrated textures with mean dihedral angles labelled on the plot.

some small variation in dihedral angle due to, for example, crystalline anisotropy. This similarity means that care must be taken when using apparent dihedral angle curves to identify textural equilibration. Additional observations, such as on the curvature of the crystal boundaries, or the use of the universal stage to make measurements in the case of fully crystallized samples are also required. The following is a summary of the major conclusions of this chapter:

- A 3-D simulation of crystallizing unequilibrated systems has been used to investigate the distributions of apparent dihedral angles expected for unequilibrated rock textures for comparison with those expected in equilibrated rock textures.
- The results of this investigation for fully crystallized, unequilibrated, monomineralic rocks were:
 - The distribution of apparent dihedral angles is similar to that expected from an equilibrated rock.
 - The distribution of apparent dihedral angles is largely independent of nuclei distribution and crystal shape.
- The results of this investigation for partially crystallized, unequilibrated rocks were:
 - Measurement of apparent dihedral angles at closed, triangular pores can produce results that mimic those of equilibrated rocks.
- Conclusion: care must be taken when interpreting textural equilibrium from apparent dihedral angle distributions.

Chapter 5

The Simulation of the Permeability and the Electrical Conductivity of Porous Media

5.0 Introduction

The porous media considered in this thesis are composed of a solid matrix (solid-fraction) and void-space (void-fraction or porosity) which consists of *pore bodies*, in which most of the porosity resides, and *pore throats*, which are the channels that connect the pore bodies (Dullien, 1992, Sahimi, 1993).

In a geologic context porous media are important because their structure controls the flow of magma in partially molten rocks, water in metamorphism, oil in oil reservoirs and water in aquifers, the flow through these media being quantified by the bulk property of permeability. Permeability characterizes the resistance of a porous medium to flow through it and can be calculated from flow rate measurements using Darcy's Law, an empirical relationship found by Darcy (1856). Darcy's Law states, that for laminar flow in a porous medium, the flow rate is linearly proportional to the applied pressure gradient and inversely proportional to the viscosity of the fluid. The one-dimensional form of Darcy's law is:

$$[5.1] \quad u = -\frac{k}{\eta} \frac{dp}{dx}$$

Where u is the flow rate per unit area (m s^{-1}) known as the *Darcy velocity*, η is the fluid viscosity ($\text{kg m}^{-1} \text{s}^{-1}$), dp/dx is the applied pressure gradient ($\text{kg m}^{-2} \text{s}^{-2}$) and k is the permeability (m^2). The

constant of proportionality, permeability (k), can be considered to be related to the drag on the fluid caused by the micro-structure of the medium through which it is flowing (King, 1987).

Permeability is generally plotted as a function of porosity (ϵ), where porosity is the total void-space fraction of the medium and permeability has some relation to the inter-connected fraction of the total void-space (effective porosity). Figure 5.1a shows a plot of log permeability against total porosity for various materials (Cheadle, 1989, Zhang *et al.*, 1994). The different curves show permeability values for the theoretical calculations of the permeability of texturally equilibrated two-phase aggregates for a dihedral angle of 50° (Cheadle, 1989), experimental measurements made on Fontainebleau sandstone (Bourbie and Zinszner, 1985), BeO and metals (Kingery, 1963) and hot-pressed calcite aggregates (Zhang *et al.*, 1994). The differences in the absolute values of the permeability in figure 5.1a are due to a number of factors, such as variations in the pore-space geometry and the grain-size of the different results. No attempt has been made to scale the results to the same grain-size as the grain-size information has not been published for the majority of the results plotted. Therefore the following discussion of the results shown in figure 5.1a is purely qualitative.

All the curves in figure 5.1a, except for the textural equilibrium example, show a similar decrease of permeability with decreasing porosity with a change in the slope of the permeability/porosity trend occurring at porosities of less than approximately 0.1ϵ . Therefore distinct power-laws are required to correlate permeability with porosity and this was shown to be due to the blocking of pore-throats (Bourbie and Zinszner, 1985, Bryant *et al.*, 1993) at porosities less than 0.1ϵ in the Fontainebleau sandstone. In addition all the curves except the textural equilibrium example exhibit a percolation threshold which is defined by the porosity at which the samples become impermeable (0.03ϵ porosity in the case of the Fontainebleau sandstone).

In the case of textural equilibrium all the pore bodies are connected by throats down to vanishingly small porosities for dihedral angles less than 60° (Cheadle, 1989). Therefore the permeability/porosity relationship is solely due to the reduction in the diameter of the flow channels and can be described by a single power-law down to porosities of 0.01ϵ for the porosity range shown in figure 5.1 and there is no percolation threshold.

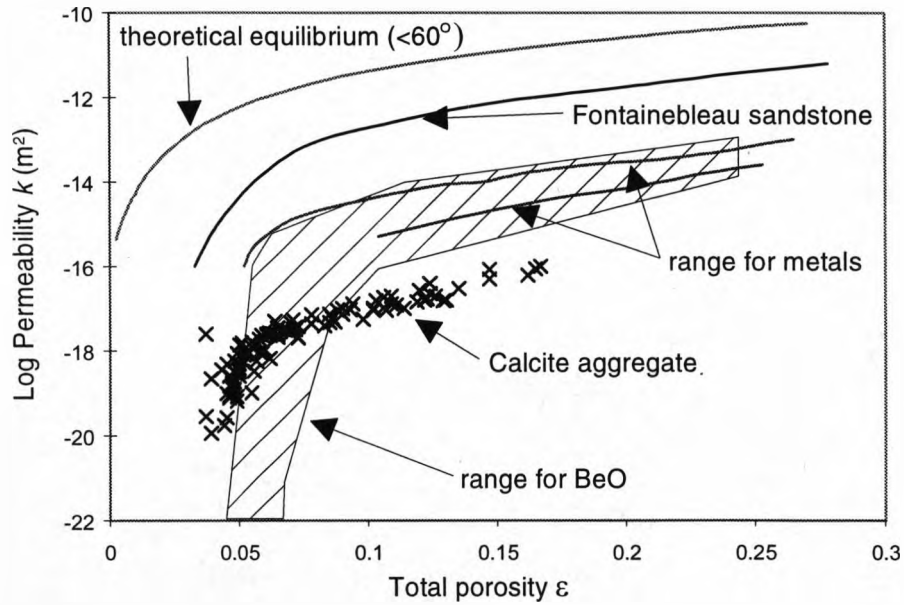


Figure 5.1a The relationship between log permeability and total porosity for various materials. Data from Cheadle (1989) for the theoretical equilibrium case, Bourbie and Zinszner (1985) for the sandstone, Kingery (1963) for BeO and the examples of metals and Zhang et al (1994) for the calcite aggregate (adapted from Zhang et al, 1994). Note: The results have not been normalised for grain-size.

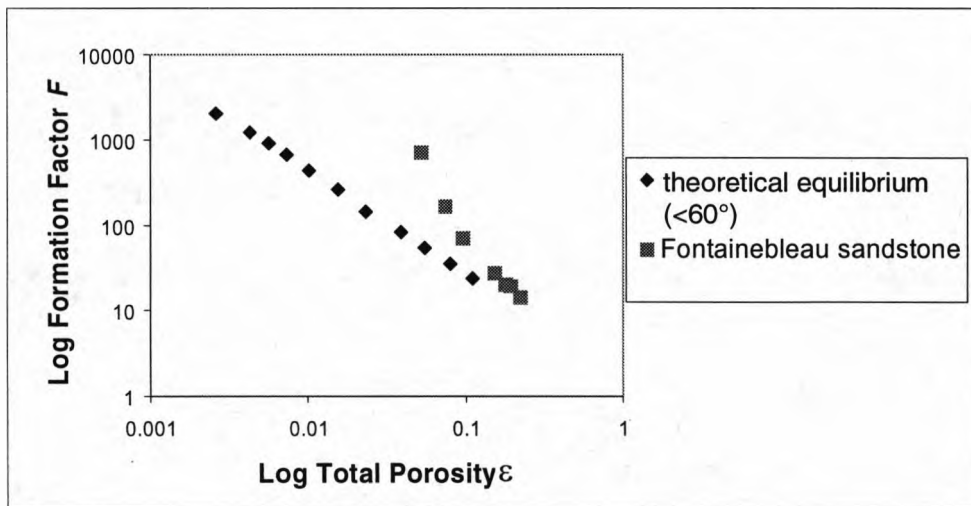


Figure 5.1b A plot of log Formation Factor against log total porosity for a theoretical equilibrium dihedral angle of $<60^\circ$ (Cheadle, 1989) and for Fontainebleau sandstone (Doyen, 1988).

In addition to permeability, the closely related bulk physical property of electrical conductivity is often measured for porous media. This is important because knowledge of the relationship between porosity and electrical conductivity for fluid-bearing rocks can, in principle, be used to interpret the results of magnetotelluric studies and thus constrain the volumes of fluid within the earth.

Electrical conductivity of a rock depends mainly upon its void-structure and is reported in terms of the Formation Factor, F , given by equation 5.2:

$$[5.2] \quad F = \frac{\sigma_w}{\sigma_o}$$

Where σ_w is the conductivity of the conducting fluid (Ωm^{-1}) and σ_o is the conductivity of the porous medium filled with the conducting fluid (Ωm^{-1}). This neglects the contribution of the solid-matrix to the electrical conductivity of the rock, which is valid for 'clean' rocks because the conductivity of the fluid ($1-10 (\Omega\text{m})^{-1}$) in the pores is usually much larger than that of the solid-matrix ($10^{-2} - 10^{-6} (\Omega\text{m})^{-1}$). A 'clean' rock is one in which the void-space does not contain additional material, such as clay, which has a high surface conductivity. Figure 5.1b shows a plot of log Formation Factor against log porosity for Fontainebleau sandstone (Doyen, 1988) and the theoretical, textural equilibrium curve predicted by Cheadle (1989) for a dihedral angle of $< 60^\circ$. The curves in figure 5.1b show a similar behaviour to the permeability curves of 5.1a. The Fontainebleau sandstone Formation Factor/porosity relationship shows two distinct power-law behaviours with the change in slope occurring at a porosity of about 0.1 ϵ . Similarly the textural equilibrium Formation Factor/porosity relationship can be described by a single power-law as before. The similarity of the two permeability/porosity relationships is expected as both bulk quantities depend upon the geometry of the void-space. This has led to the common assumption that there is a simple relationship between permeability and electrical conductivity, however, recent research has shown that fluid-flow and electrical current flow follow different paths through a porous medium (Zhang and Knackstedt, 1995, David, 1993). This is because local hydraulic conductances scale as the local pore radius raised to the power four whereas

electrical conductances scale as the square of the local pore radius. Therefore local variations in the pore structure of the porous medium will create different paths for fluid flow and electrical current flow. This means there is no direct relationship between the two quantities, even though their behaviour is similar.

The preceding paragraphs show that the relationship of permeability and electrical conductivity to porosity are important and that currently there are no measurements available for these properties in crystallizing systems. Therefore, in this chapter a method will be proposed for exploring the permeability/porosity and electrical conductivity/porosity relationships for partially molten systems. This is based upon measurements made from the three-dimensional numerical simulation of crystallizing systems described in Chapter 3.

5.1 The Calculation of Permeability

There are six main approaches to calculating permeability and/or electrical conductivity that have been attempted in previous work (Sahimi, 1993);

- i) Exact results and rigorous bounds
- ii) Effective-medium approximations
- iii) Percolation methods
- iv) Field-theoretic and perturbation methods
- v) Lattice-gas cellular automata
- vi) Network simulations

Some of these methods are applicable to determining both permeability and electrical conductivity, while others are applicable to only one or the other. These methods will be reviewed and the use in this work of network simulation as the method to calculate permeability and electrical conductivity will be justified.

i) Exact results and rigorous bounds

Exact results are based on a reformulation of Darcy's law that allows the permeability to be calculated if two unknown functions can be calculated. Solutions to these unknowns are only available for a limited number of void-space morphologies, defined by either periodic arrays of

spherical particles of radius r placed at the nodes of a regular lattice (Hasimoto, 1959, Larson and Higdon, 1989) or for two-component mixes of spheres and matrix (see Bonnacaze and Brady, 1990, for references). These models are therefore idealizations of porous media and are of limited applicability to real porous media because they cannot represent the actual pore geometry, which is the fundamental controlling factor on permeability.

Rigorous bounds, in comparison, are calculated from various statistical properties of the porous media and so are applicable to real porous media. They were first used to estimate the permeability of rock-like materials (Prager, 1961, Berryman and Milton, 1985, Rubinstein and Torquato, 1988), but the results obtained were usually an order of magnitude too large when compared to measured permeability values. This is probably because they ignore the effects of disconnected porosity, which does not contribute to the permeability. Blair *et al.* (1996) have since combined this method with the use of approximate formulas for permeability to produce results within a factor of two of the measured permeability values. However, these methods contain adjustable parameters within the approximate formulas for permeability, the values of which can only be found empirically by fitting the results to measured data (Blair *et al.*, 1996). This reduces the amount of physical insight into the processes that are controlling the permeability (Bryant *et al.*, 1993). In addition, these methods have only been applied to relatively simple sandstones with effective porosity equal to total porosity, they probably do not apply for media where this condition does not hold true (Blair *et al.*, 1996).

ii) Effective-medium approximations

Effective-Medium Approximation (EMA) is a method for transforming a many-body problem into a single-body problem (see Landauer, 1978, for a history of EMA's). In the case of porous media, the heterogeneous void-space of a real porous medium is transformed into a homogenized void-space with unknown physical constants which can then be solved for using spatial averages. The EMA approach has been applied to sandstones by Koplik *et al.* (1984) who predicted permeability with an order of magnitude difference from the measured values and by Doyen (1988) who could predict permeability within a factor of three and electrical conductivity within a factor of

two. However, both these approaches assume that throat radii are not spatially correlated in order to generate their governing equations. This means that although the throat-radii have a similar size distribution to a real sample, they are distributed randomly within the void-space. This is unlikely to be the case in the majority of porous media (Bryant *et al.*, 1996) leading to results that neglect an essential aspect of the physics of these media.

iii) Percolation methods

Percolation theory, in regard to real porous media, considers the probability that flow or conduction can occur through a medium. If flow does not occur then the medium is impermeable (and does not percolate) and if flow does occur then the medium is permeable (and therefore percolates). The point of transition between these two states is the percolation threshold and is the porosity at which a sample spanning flow path has occurred. Using the percolation method of Katz and Thompson (1986, 1987) it is possible to estimate permeability to within a factor of two, however, additional information from mercury porosimetry is required to evaluate one of the parameters within their equations. Unfortunately, it is not possible to make such measurements on numerically simulated media!

iv) Field-theoretic and perturbation methods

These methods use the fact that disorder is equivalent to a physical field, therefore it is possible to model transport properties of disordered (inhomogeneous) media. They were first developed by King (1987) and use a probabilistic approach to calculate permeability. This means that a guess of the probability distribution of permeability within the medium (for example log-normal) is used to generate the effective permeability value for the whole medium. This method has reproduced several known exact results, but has not been applied to more complex, real porous media, it is also not valid for media with zero permeability at some finite value of porosity (percolation threshold) (King, 1987). The existence of a percolation threshold in non-equilibrium crystallizing systems (Faul, 1997) precludes the use of this technique.

v) Lattice gas cellular automata

Lattice gas cellular automata are methods for approximating the solution of the Navier-Stokes equation for fluid-flow (D'Humières *et al.*, 1986, Olson, 1995) and the Laplace equation for conductivity (Zhang and Knackstedt, 1995) within complicated void-space geometries in three-dimensions. They use large lattices with each site occupying one of several discrete states to model fluid-flow/conductivity, by simulating the interaction of particles representing the fluid/electric charge. The particles are abstractions and in no way reflect real particles within the fluid, however, it is still possible to recover the equations of hydrodynamics/electromagnetism from the average motions of these particles. Unfortunately, lattices of greater than several hundred thousand sites currently require the use of supercomputers, therefore their implementation for this work is impracticable as the lattices used in this work consist of eight million sites.

vi) Network simulations

Network simulations are the main numerical method of estimating the permeability of an inhomogeneous void-space. To calculate the permeability, a pore-throat shape and flow regime are assumed. For example, assuming cylindrical throats and Poiseuille flow we can calculate a relationship between the pressure and flow rate within each pore. Assuming that the net flow for each pore body is zero an equation for the mass balance at each pore body can be written. This generates a set of simultaneous equations for pore pressures from which the pressure distribution throughout the medium can be calculated and this can then be used in the permeability calculation. Most previous work has been carried out by assuming a specific micro-structure for the network (Fatt, 1956, Dullien, 1975, Koplik *et al.*, 1984, Doyen, 1988). However the permeability (Bryant and Blunt, 1992) and electrical conductivity (Bryant and Pallatt, 1996) have been calculated for a random close packing of equal-sized spheres (Finney, 1968) using a network simulation that did not assume a specific micro-geometry. This generated permeability/conductivity results that agreed very well with experimental data. Network simulation has been shown to be a physically rigorous (no adjustable parameters) method for calculating permeability/conductivity, that does not suffer from the problems of the other approaches (Bryant and Blunt, 1992). However, it is only applicable if full three-dimensional information on the void-space is available and correctly characterized.

5.2 The Characterization of Void-Space

Permeability and electrical conductivity, as discussed in section 5.0, are fundamentally controlled by the micro-geometry of the void-space through which fluid/electric charge flows. Variations in flow being caused, for example, by maxima and minima in hydraulic radius (i.e. pore bodies and throats) and topology (connectivity or genus). To correctly calculate permeability/conductivity using a network simulation detailed information about these factors is required. The following sections will describe previous attempts that have been made to solve this problem and introduce a new method for characterizing the void-space in three-dimensions. A similar approach has been recently published independently by Baldwin *et al.* (1996). However, they only apply their method to the characterization of sphere packs and make no attempt to calculate the permeability.

5.2.1 Previous Methods for Characterizing the Void-Space

There are four approaches which have previously been used to characterize the micro-structure of the void-space of an inhomogeneous medium (Baldwin *et al.*, 1996);

- i) Digitized Serial-Sections
- ii) Tessellation of the Void-Space
- iii) Two-Dimensional Erosion
- iv) Morphological Thinning

They all require the partitioning of the void-space into individual *pore bodies*, which account for most of the porosity, that may be connected together by *pore throats*, which are the channels that connect the pore bodies (Sahimi, 1993). The number of pore throats that connect to a pore body is the *coordination* number of that pore body (see fig. 5.2).

i) Digitized Serial-Sections

Digitized serial-sections were used to characterize the pore space of real porous media by Kwiecien *et al.* (1990), Zhao and Macdonald (1993) and Zhao *et al.* (1994). Pore throats were identified by examining multiple randomly oriented sections through a three-dimensional volume,

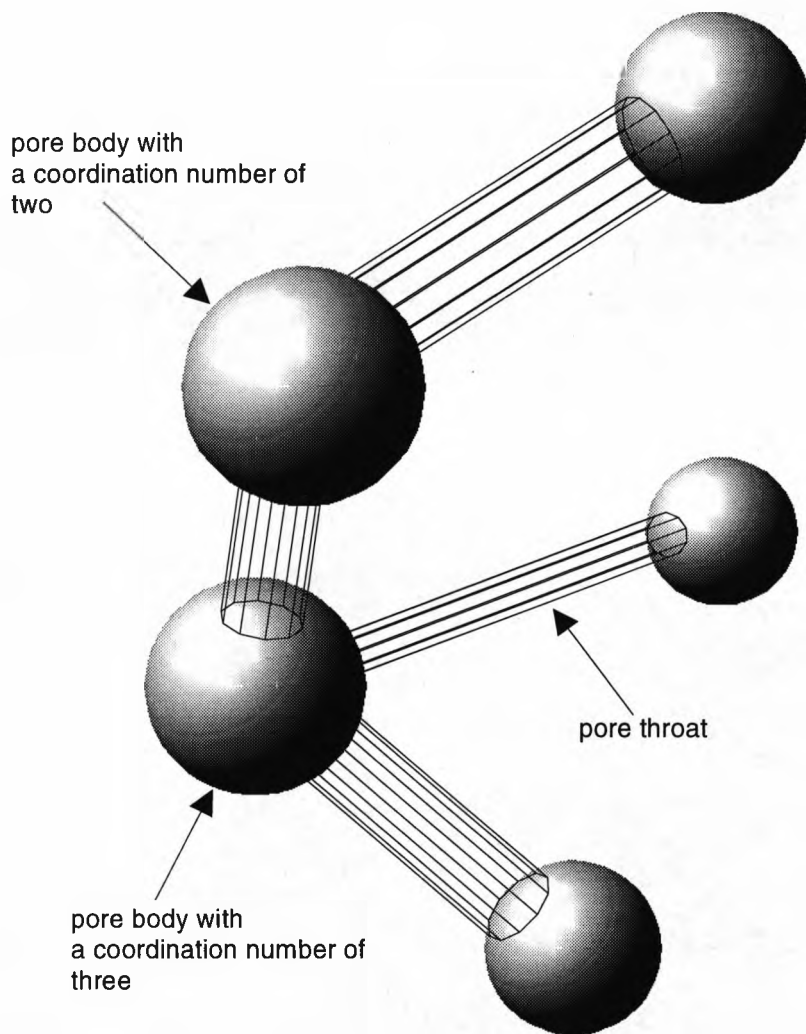


Figure 5.2 Ball (pore body) and stick (pore throat) representation of the void-space.

but many throats can be missed or misidentified unless a sufficient number of oriented sections are examined when characterizing the void-space of the volume (Zhao *et al.*, 1994).

ii) Tessellation of the Void-Space

This approach has only been applied to sphere-packs (Chu and Ng, 1989, Bryant and Blunt, 1992) and consists of tessellating the void-space into an *a priori* shape, such as the tetrahedron. The vertices of the tetrahedra are at the sphere centres and the interiors of the tetrahedra enclose the pore bodies. Each face of a single tetrahedron contains a pore throat and therefore each pore body has a coordination number of four. This method has several problems, first, as the packing of spheres becomes less dense the pore bodies and pore throats become less well defined (Baldwin *et al.*, 1996) reducing the accuracy of flow calculations which depend upon these quantities. Second, the *a priori* choice of a single tessellation geometry imposes an artificial geometry upon the void-space. For example, if a tessellation geometry based on a tetrahedron was applied to an ordered cubic sphere packing, a significantly different geometry would result compared to the application of a tessellation geometry based on a cube (Chu and Ng, 1989). This would result in two representations of the same media having significantly different spatial correlation of pore bodies and pore throats. Bryant *et al.* (1993) have shown that this can have a significant effect on the calculated permeability/conductivity. In addition, it has been shown that any method that is based on tessellating the void-space is unsuitable for obtaining flow networks in poorly sorted sandstones (Schwartz and Banavar, 1989).

iii) Two-Dimensional Erosion

Two-Dimensional Erosion is one of the many erosion methods (Pratt, 1991) that can be used to reduce the void-space of a medium, represented as two-dimensional sections, to a minimally connected network. Figure 5.3a shows the erosion of a two-dimensional section through a void, in which each layer that is removed by the erosion is numbered. In this example the total erosion of the void-space would end with a point numbered three, roughly at the centre of the void. This point belongs to the set of points that form a minimally connected network. The three-dimensional minimally connected network of the void-space of a medium can therefore be approximated by connecting all the points found from the erosion of the voids in consecutive two-dimensional sections

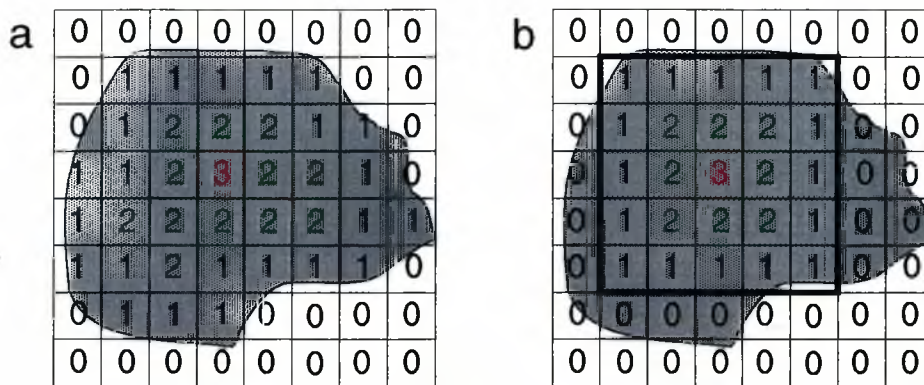


Figure 5.3a Diagram of the erosion of a void-space (shown in grey). The numbers indicate each layer that is eroded from the void-space with each pass of the erosion function. Figure 5.3b Diagram of the dilation (shown by black line) of the void-space eroded in figure 5.3a in an attempt to re-construct the void-space (shown in grey). The numbers indicate each layer that is added to the void-space with each pass of the dilation function. Note that dilation (shown by black line) is not the reverse of erosion and hence the re-constructed void-space differs from the original.

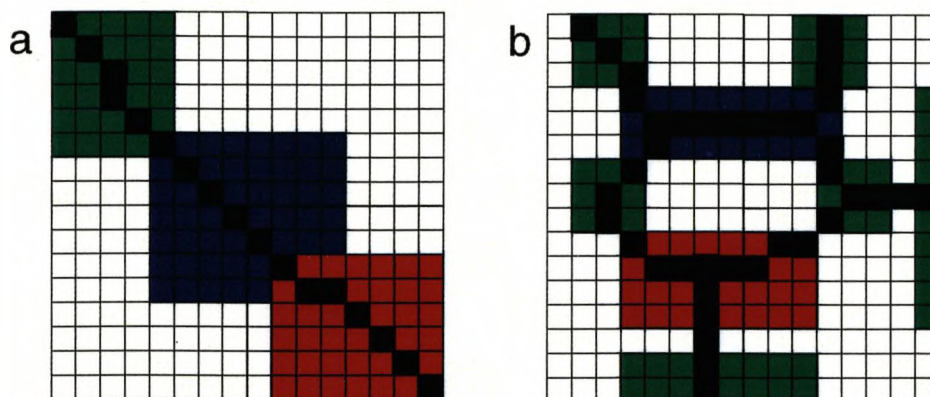


Figure 5.4a Diagram of the void-space split into three pore bodies. The skeleton (shown in black) fails to identify a two-coordinated pore (blue). Figure 5.4b Diagram of the void-space split into a three-coordinated pore (red) and a four-coordinated pore (blue). The skeleton (in black) for the red pore contains one three-coordinated point where the skeleton branches, which is correct. However, the four coordinated pore (blue) has a skeleton composed of two three-coordinated points, which is incorrect. (After Baldwin *et al.*, 1996).

(Doyen, 1988, Pratt, 1991). To re-create the void-space the network can then be dilated. Figure 5.3b illustrates a two-dimensional example of the dilation of the void-space from the point numbered three (generated by the erosion of figure 5.3a). The numbers represent each layer that is added by each pass of the dilation function. Unfortunately as dilation is not the exact reverse of erosion (Pitas, 1993) the resultant void-space is topologically, but not geometrically, equivalent to the void-space of the medium. This is a major drawback to this method as it produces a void-space geometry that is inherently model-dependent.

iv) Morphological Thinning

Morphological thinning is a variant of the erosion methods described above. It produces a skeleton representation of the void-space in three-dimensions. It was first proposed by Lin and Cohen (1982) and first implemented by Thovet *et al.* (1993). The first application to real porous media was by Spanne *et al.* (1994). They applied morphological thinning to various tomographic (3-D) images of sandstones and produced a network representation of the void-space. Unfortunately, morphological thinning suffers from the same problems as erosion. The topology of the void-space is correct, but the geometrical information is lost. To address this problem Thovet *et al.* (1993) attempted to partition the void-space into pore bodies and pore throats based upon the vertices and edges of the network, however, their method leads to ambiguities in the network and misidentified pores (Baldwin *et al.*, 1996). This can be seen in figure 5.4a where the skeleton has failed to identify the presence of a two-coordinated pore and in figure 5.4b where it has misidentified a four-coordinated pore as two, three-coordinated pores.

The above discussion of previous methods for characterizing the void-space of porous media shows that they are inadequate and that it is necessary to adopt a different approach to correctly obtain both the topological and geometrical data required for a network calculation of permeability.

5.3 Calculation of Permeability/Electrical Conductivity using a Network Simulation and its Relation to the Characterization of the Void-Space

The key requirements for a void-space characterization algorithm, that can be used to generate the data required by a network simulation of permeability/electrical conductivity, are that it partitions the void-space of the medium into rigorously defined pore bodies and pore throats, whilst retaining all topological (connectivity, coordination number, etc.) and geometrical (pore body separations, throat diameters, etc.) information.

The method for calculating the electrical conductivity is essentially the same as that of permeability except that there are some differences in the governing equations. Therefore the methodology that follows (section 5.3.1) will be described in terms of the calculation of permeability and the alternative equations for the electrical conductivity will be given later, in section 5.3.4.

5.3.1 Calculation of Permeability using a Network Simulation

As outlined in 5.1vi to calculate permeability using a network simulation the void-space must be partitioned into individual pore bodies connected by pore throats. This can be visualized as a ball (pore body) and stick (pore throat) representation of the void-space (fig. 5.2) from which permeability may be calculated using a similar approach to Bryant and Blunt (1992). This approach is then adapted and combined with the void-space characterization method to produce a general method for calculating permeability in porous media.

Considering a single pore body and associated throats, mass conservation requires that the flow into and out of the pore body through its associated throats must be zero assuming that the pressure throughout the void-space is in a steady-state. Therefore the flow rate through the pore throats between connecting pore bodies needs to be calculated. Neglecting the pressure across the pore body where pore throats meet¹, for steady incompressible flow the following relationship is valid;

¹ Neglecting momentum loss at the pore body where pore throats meet tends to balance the multiple-counting of momentum loss in the flow paths where they over-lap at the centre of the pore bodies (Bryant *et al.*, 1993).

$$[5.3] \quad Q = g\Delta P$$

Where Q (m^3s^{-1}) is the flow rate, g ($\text{kg}^{-1}\text{m}^4\text{s}$) is the hydrodynamic conductivity and ΔP ($\text{kgm}^{-1}\text{s}^{-2}$) is the pressure difference between the pore bodies. Assuming that flow through the real pore throat can be modelled by Poiseuille flow (Bryant and Blunt, 1992) in a cylinder of radius r and length l then g is defined as;

$$[5.4] \quad g = \frac{\pi r^4}{8\mu l}$$

Where μ ($\text{kg s}^{-1}\text{m}^{-1}$) is the fluid viscosity. It is then possible to write a mass balance equation for this hypothetical pore body and associated throats. Assuming that pore body, i , has k throats connecting it to j other pores, then for the k^{th} throat;

$$[5.5] \quad Q_k = g_k \Delta P_{ij}$$

Where $\Delta P_{ij} = P_i - P_j$ and invoking mass conservation;

$$[5.6] \quad \sum_k Q_k^i = 0, \text{ for throats } k \text{ connected to pore } i.$$

So far consideration has only been given to a single pore body and its associated throats, however, there are many of these pore bodies and throats forming an inter-connected network. To calculate the permeability of this network the i simultaneous equations given by equation [5.6] must be solved with suitable boundary conditions (this will be discussed in 5.4.3.2).

It can be seen from the above equations that to calculate the permeability of a porous medium, three quantities are required; the values of the radius, r of the hydrodynamically equivalent pore throat between two pore bodies; the length, l of the hydrodynamically equivalent flow channel

(dependent on the geometry of the void-space) and the degree of inter-connection of the pore bodies and throats (dependent on the topology of the void space). Figure 5.5 shows a two-dimensional diagram of the flow channel with the radius and channel length marked. The topology of the void-space is not shown as this is a three-dimensional quantity. As discussed earlier (section 5.1vi) the method used by Bryant and Blunt (1992) to extract these quantities has limited application. The next section will outline a more general method applicable to any three-dimensional porous medium.

5.3.2 The Three-Dimensional Numerical Characterization of Void-space

The technique that follows is based on a new algorithm that characterizes the void-space of porous media. This has been independently developed by the author, although the method is similar to Baldwin *et al.* (1996). Comparison is made with their work where necessary.

A pore throat can be defined as a plane erected normal to where the hydraulic radius of the void-space exhibits a local minima (Bear, 1972, Dullien, 1991), where the hydraulic radius, R_H (m), can be defined as;

$$[5.7] \quad R_H = \frac{A}{P}$$

where A (m^2) is the cross-sectional area normal to the constriction and P (m) is its wetted perimeter. The theory of hydraulics then defines the channel radius, R_c (m), governing the flow through a conduit as;

$$[5.8] \quad R_c = 2R_H$$

Figure 5.6 shows conceptually how this definition can be used to partition the void-space into pore bodies separated by pore throats defined by local minima in the hydraulic radii of the void-space.

An alternative method for allocating the radius of the hydrodynamically equivalent channel is to use the cross-sectional area at the local minima in the hydraulic radius of the void-space. Equation 5.8 then becomes:

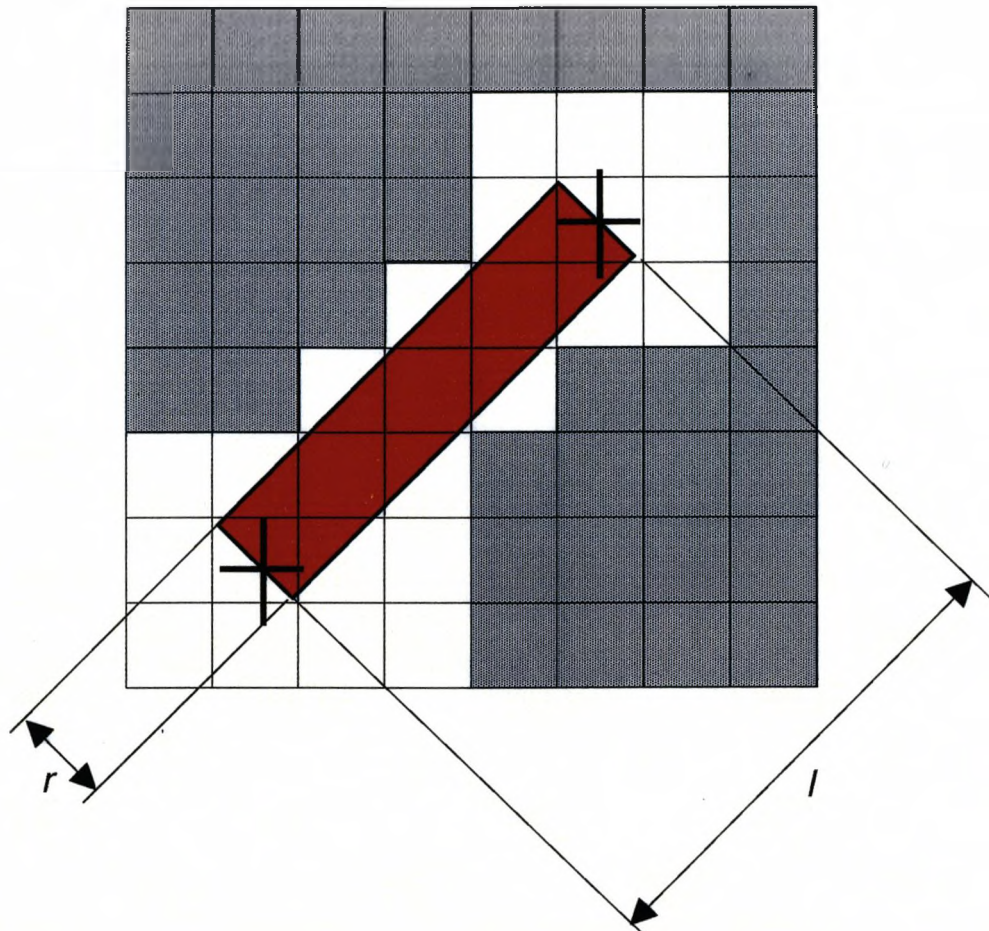


Figure 5.5 Two-dimensional diagram of the equivalent flow channel (shown in red) where r is the radius of the narrowest cross-section of the void-space (shown in white) and the matrix is shown in grey. The black crosses mark the centres of the pore bodies and l is the distance between the centres of the connected pore bodies.

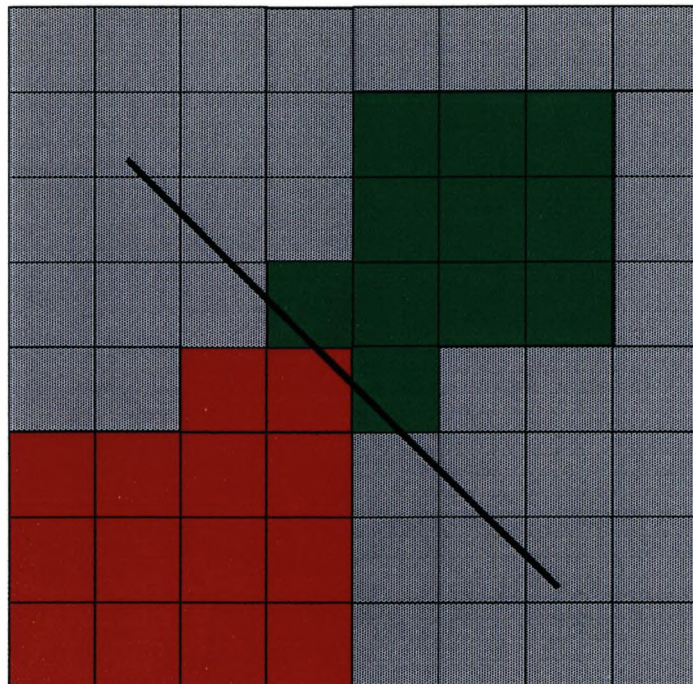


Figure 5.6 Diagram of two pore bodies (red and green) defined by an interface erected at the minima of the hydraulic radius between the two pore bodies (black line).

$$[5.9] \quad R_c = \left(\frac{A}{\pi} \right)^{\frac{1}{2}}$$

Recent experimental work by Sederman *et al.* (1997) shows that the volume flow rate (in a sphere pack) scales as the cross-sectional area of the constriction squared, which justifies the above approach (eq. 5.9).

To apply the above definition of a pore throat to the void-space of a medium, the algorithm used to characterize the void-space must partition the void-space into pore bodies connected by pore throats that have planes erected at the minima of the hydraulic radii. Thereby enabling the cross-sectional area normal to the constriction and the wetted perimeter to be calculated. In addition, the calculation of l (in eq. [5.4]), the length of the pore throats, requires that the centres of all pore bodies are known and the connections between pores must also be known in order to calculate the topology of the network.

These quantities are calculated by partitioning the void-space into individual pore bodies using a voxel-based approach, similar to that used in the numerical simulation of crystallization (Chapter 3). Conceptually, if the centres of the pore bodies (as defined above) can be found, then it is possible to partition the void-space by dilating (section 5.2.1 iii) the pore centres and competing for the void-space. Figure 5.7 shows a simple two-dimensional example where the pore body centres have been allocated the number one. It can be seen that two passes of the dilation function result in the minima in the hydraulic radius of the void-space being defined by the interface between the red and green pore bodies. When calculating this for a real example each dilation of each pore centre would be assigned a different integer value, so that individual pore bodies could be identified. This is a natural extension of the modelling carried out in Chapter 3 relating to the growth and competition between crystals.

5.4 Partitioning of the Void-Space in Three-Dimensions

To identify the pore bodies within the void-space it is partitioned in such a way that the definition of a throat between two connecting pore bodies follows that of Dullien (1992) (section

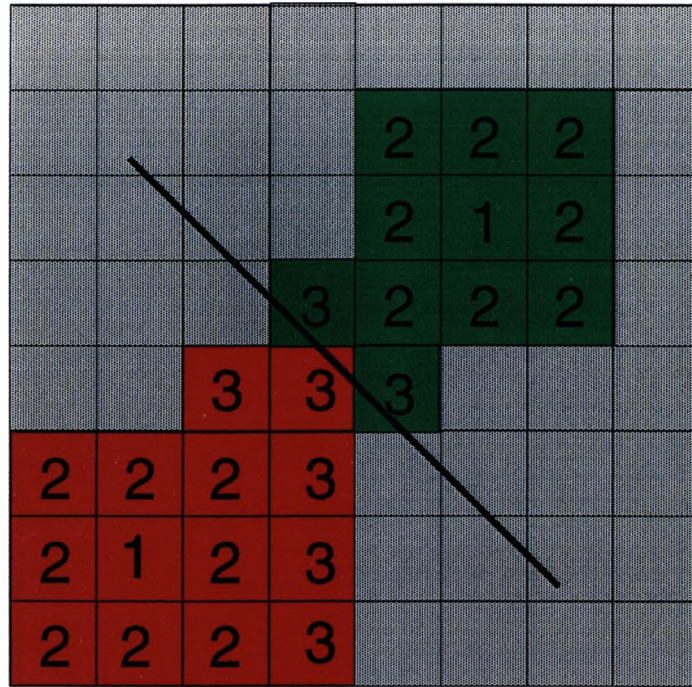


Figure 5.7 Diagram of the dilation of two pore bodies. Assuming the centre of the pore bodies has been found the minima in the hydraulic radius of the void-space (black line) can be found by dilating the pore bodies from their centres. The interface between the two pore bodies represents a plane erected normal to the constriction of the void-space.

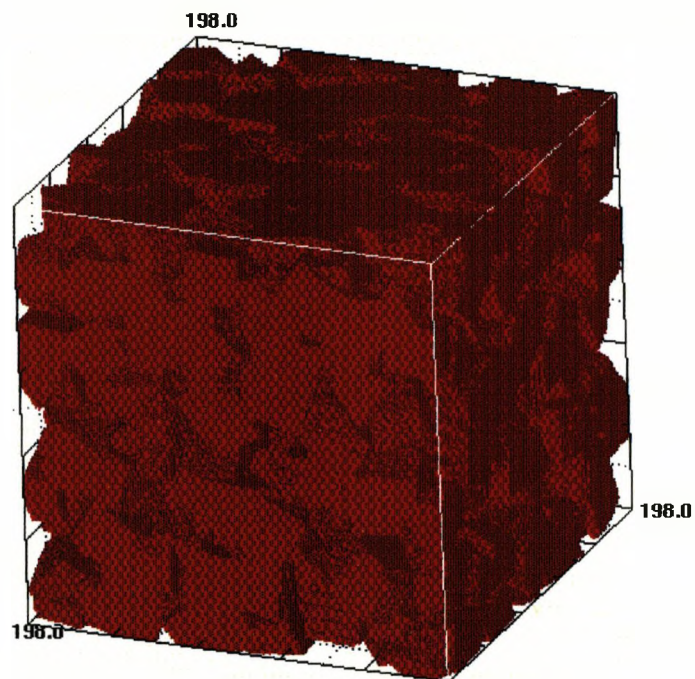


Figure 5.8 Binary image of a model volume containing 900 crystals which originally had a cube-shaped ideal morphology. The solid-matrix is shown in red and the void-space is not displayed.

5.3.2). The first step as shown in figure 5.7 requires the centres of the pore bodies. These can be found by using an iterative, three-dimensional erosion (Doyen, 1988) of the void-space.

5.4.1 Erosion of the Void-Space in Three-Dimensions

The erosion technique locates the centres of the pore bodies because they are local maxima in the void-space and are therefore locally the last region to be eroded. The technique requires that the porous medium be represented by a binary three-dimensional image, where the void-space is represented by ones and the solid matrix by zeros. This binary image (see fig. 5.8) can be extracted from the Increment Model (as defined in Chapter 3.2.2.2) by applying a cut-off filter described by the following inequalities;

$$[5.10] \quad \text{if } V_{im} > i_c \text{ then } V_{bin} = 1 \text{ and if } V_{im} \leq i_c \text{ then } V_{bin} = 0$$

Where V_{im} is the value of a particular voxel in the increment model, V_{bin} is the equivalent voxel in the binary image and i_c is the cut-off value of a voxel at a particular growth increment within the Increment Volume. This results in a binary image with all the voxels at or below the cut-off value representing the matrix and all the voxels above the cut-off value representing the void-space. The porosity in the resultant binary image is related to i_c by some non-trivial function of the growth rate and nuclei distribution as discussed in section 3.6.1.

The first pass ($n=1$) of the three-dimensional erosion function proceeds by identifying all the voxels within the void-space whose first, second and third nearest neighbour voxels (see figure 5.9) lie next to matrix voxels (with value $n-1$), these voxels are then assigned the value n . This is analogous to the two-dimensional erosion described in section 5.2.1iii. The algorithm then proceeds iteratively to erode the rest of the void-space, the process finishing when there are no more voxels to erode. This results in a three-dimensional image where the void-space is composed of layers of eroded voxels whose values represent the number of the iteration at which they were eroded (see fig. 5.10). Figure 5.11 a-f illustrates the n erosion layers for a model volume containing a few voids where the solid-matrix has not been displayed. Figure 5.11a contains all the erosion layers, ranging from an erosion value of one for the dark blue layer, to the highest visible (in the figure) erosion

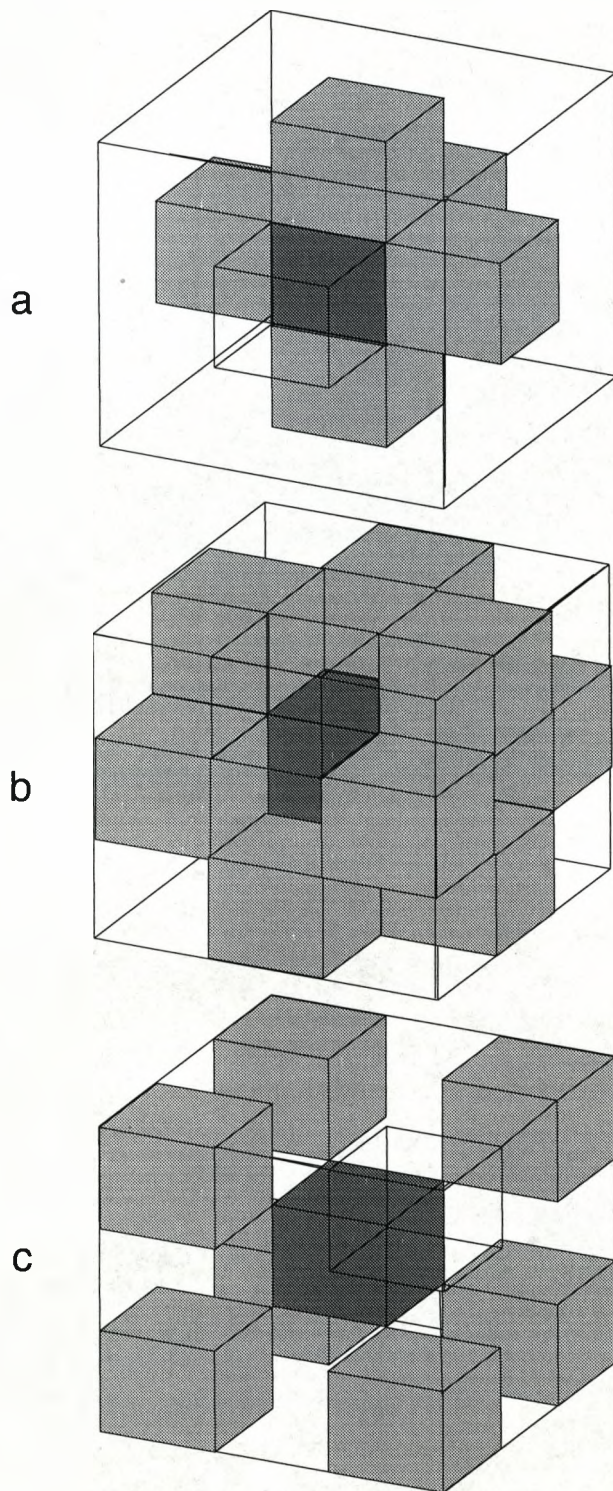


Figure 5.9 Diagram of first (a), second (b) and third (c) nearest neighbour voxels of the voxel shown in dark grey. In each case one of the nearest neighbour voxels has been rendered transparent for clarity of presentation.

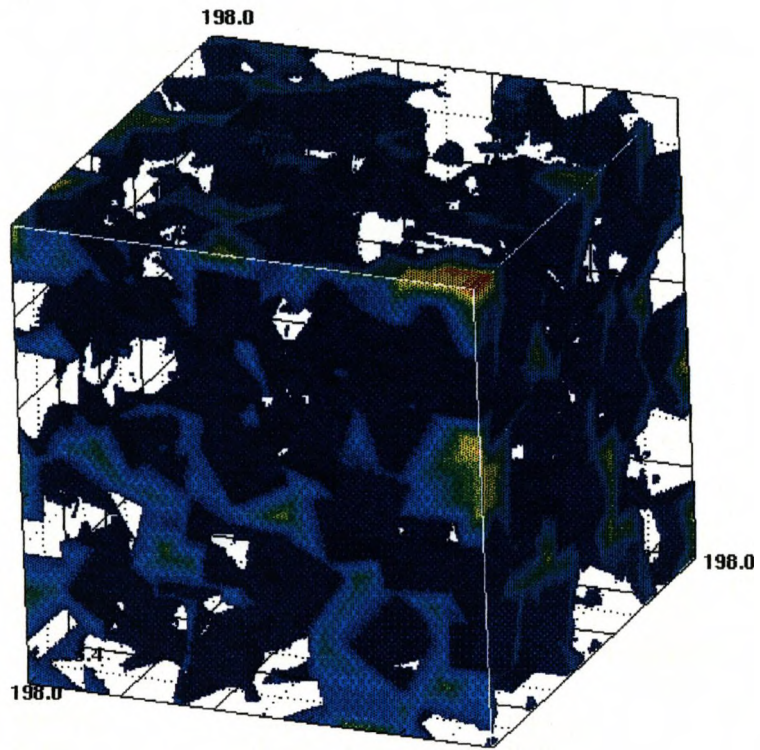


Figure 5.10 Image of the erosion of the void-space of fig. 5.8 with the solid-matrix not displayed. Colours represent the degree of erosion from low (dark blue) to high (red).

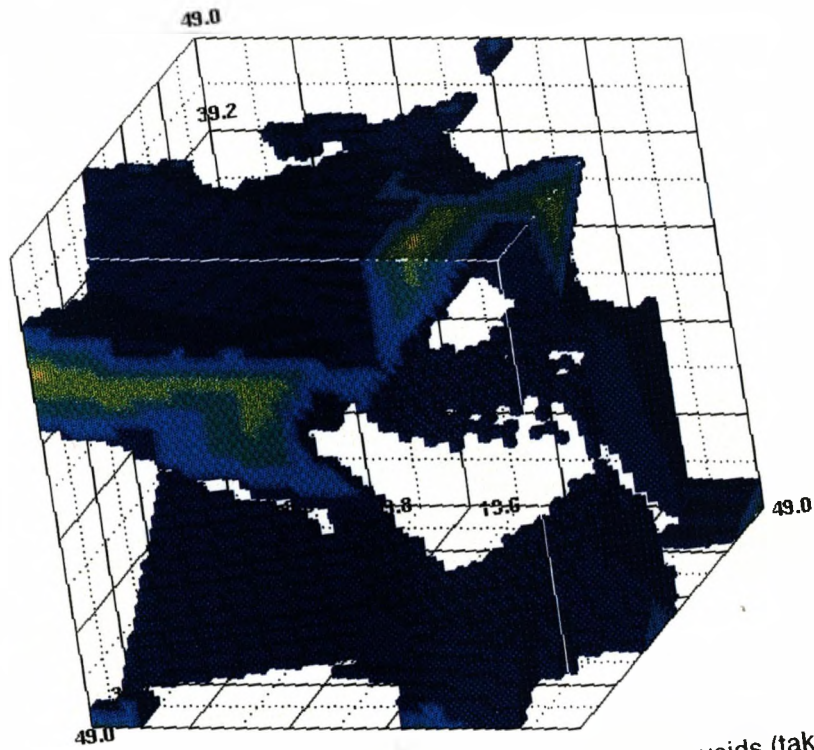


Figure 5.11a Detailed view of the erosion of the void-space of a few voids (taken from fig. 5.10). All six erosion levels present.

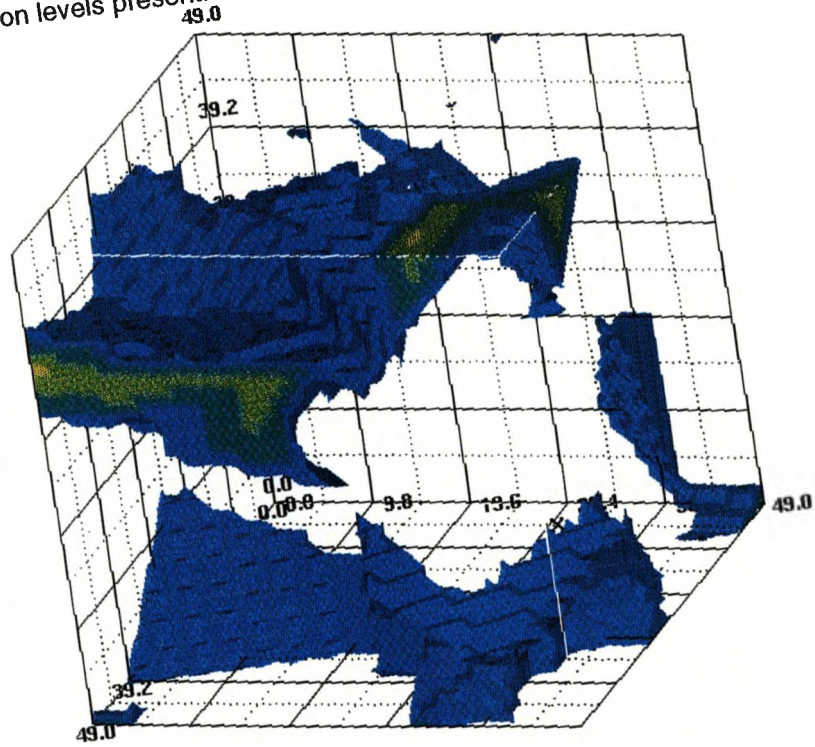


Figure 5.11b Detailed view of the erosion of the void-space of a few voids. Erosion level one has been removed.

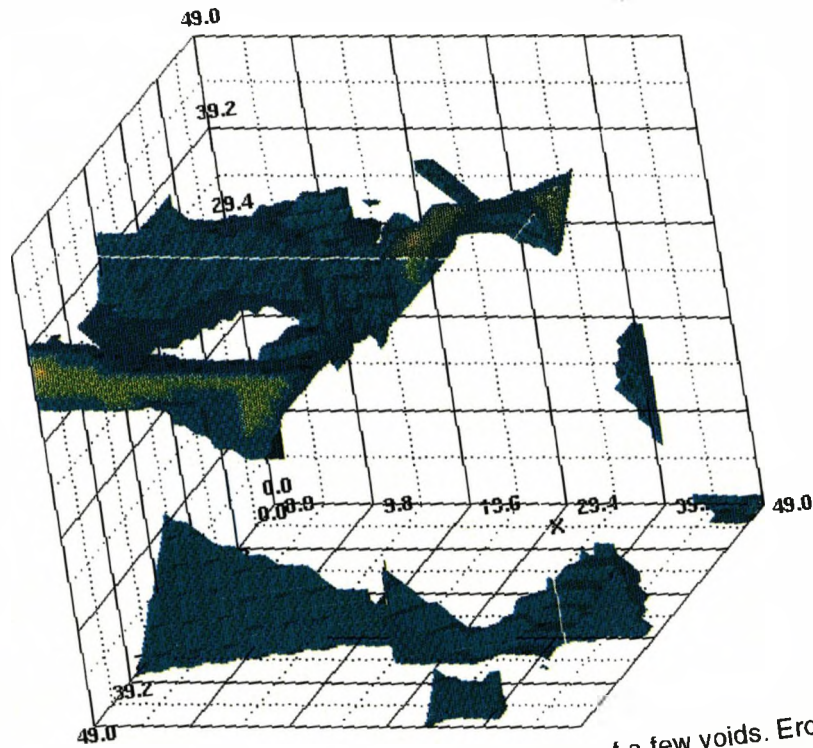


Figure 5.11c Detailed view of the erosion of the void-space of a few voids. Erosion levels one and two have been removed.

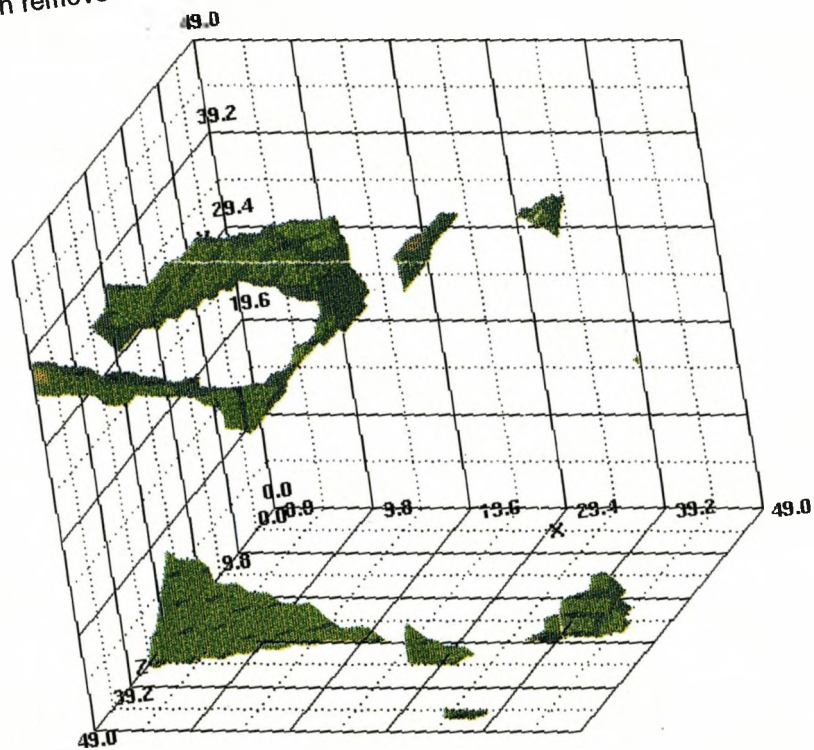


Figure 5.11d Detailed view of the erosion of the void-space of a few voids. Erosion levels one, two and three have been removed.

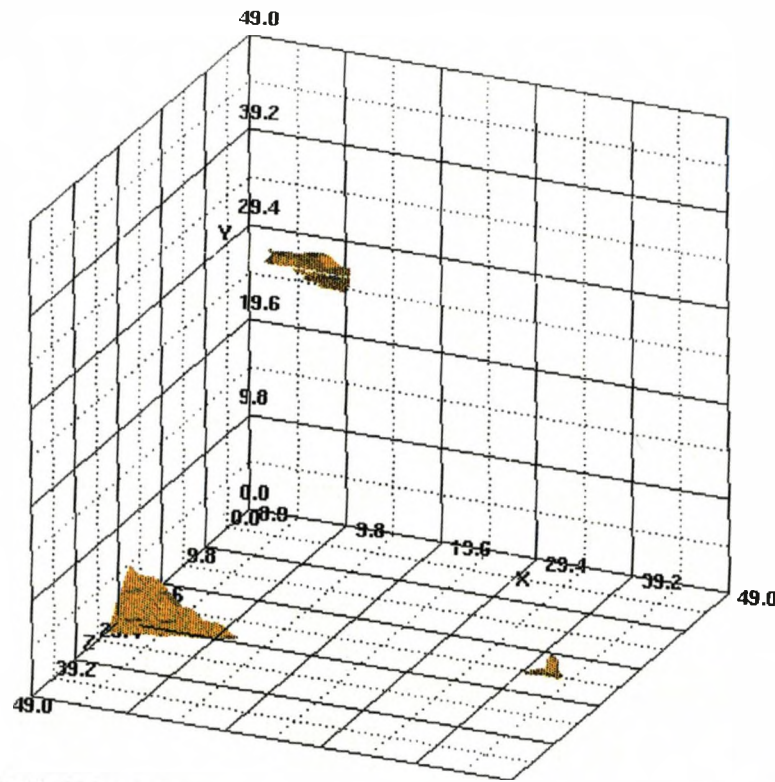


Figure 5.11e Detailed view of the erosion of the void-space of a few voids. Erosion levels one, two, three and four have been removed.

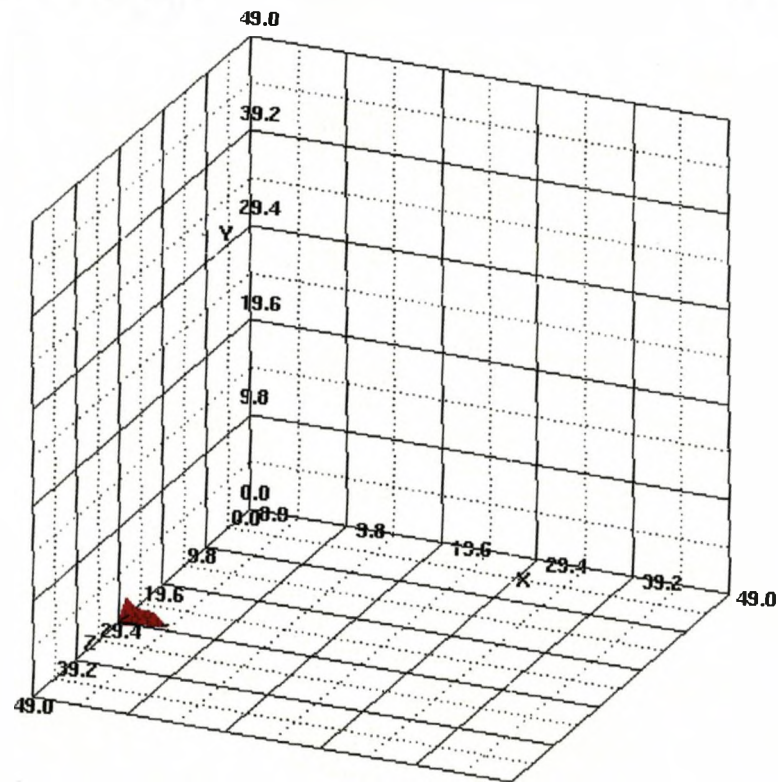


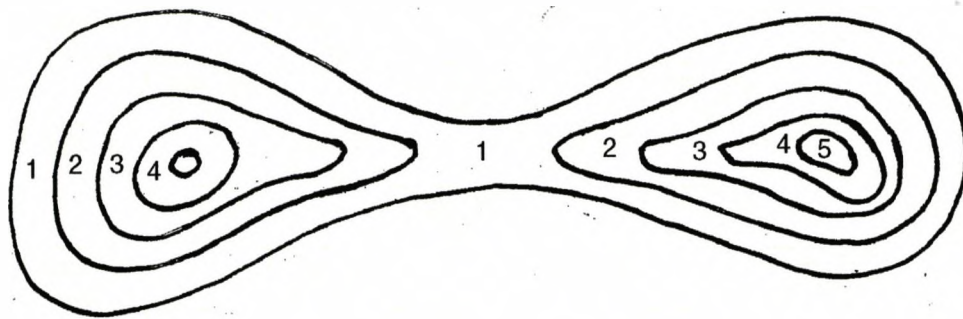
Figure 5.11f Detailed view of the erosion of the void-space of a few voids. Erosion levels one, two, three, four and five have been removed.

layer of four (orange) in the top near right of the volume. The subsequent figures 5.11b through to 5.11f show removal of each erosion layer. If we consider the large void in the bottom near left of the volume and follow its erosion through figures 5.11a-f it can be seen that the void becomes a distinct pore in figure 5.5d and that the pore centre is defined by erosion level six in figure 5.5f. Pore centres therefore correspond to regions of local maxima (high iteration number) and pore throats to regions of local minima (low iteration number). Figure 5.12a illustrates this for the erosion of a dumb-bell shaped void, the numbered contours representing different erosion levels within the void for a two-dimensional section through the dumb-bell. Unfortunately, it is impossible to simply search for the local minima within the void-space because the minima form topologically complex surfaces in three-dimensions. This is shown in figure 5.12b where the erosion level at the minima is shown as a three-dimensional surface for the dumb-bell shaped void.

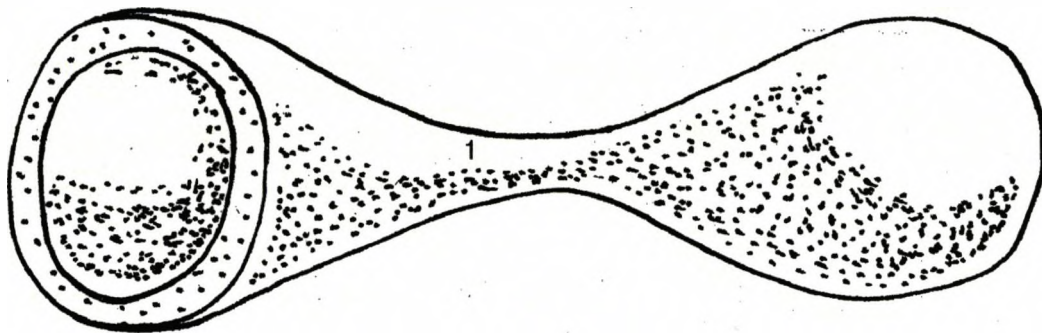
5.4.2 Partitioning of the Void-Space in Three-Dimensions

The void-space is now composed of regions of local maxima (pore bodies) and local minima (pore throats). The local maxima are identified at each iteration value within the image and then grown to form pore bodies by finding the first, second and third nearest neighbour voxels that are connected to the local maxima for all iteration values equal to or below the maxima value. This approach is the same as that adopted by Baldwin *et al.* (1996), however, they used an erosion function that only considers the first nearest neighbour voxels. This can cause the creation of false local maxima as shown in figure 5.12c where the erosion function used by Baldwin *et al.* (1996) is applied to two pores connected by a throat. Figure 5.12d shows the same two pores eroded with a function that uses the first, second and third nearest neighbour voxels as applied in this thesis. It can be seen that the pore maxima are correctly identified in this case. Using only the first nearest neighbour voxels (fig. 5.12c) in the erosion fails because the surface of the eroded layer (shown in blue) does not exactly follow the surface of the void-space (shown in grey) as can be clearly seen in figure 5.12c.

Once all local maxima are grown to form pore bodies by dilation the void-space is fully partitioned with each pore body being assigned an integer value.



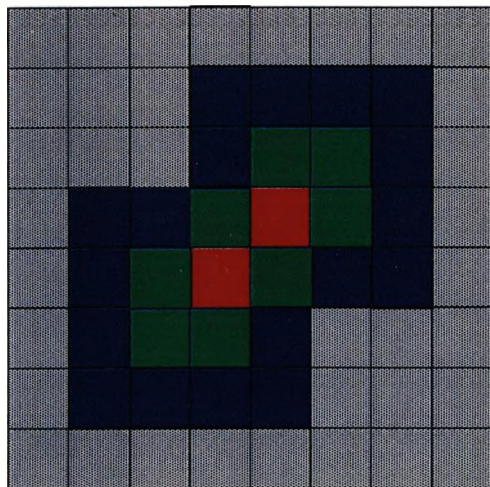
a



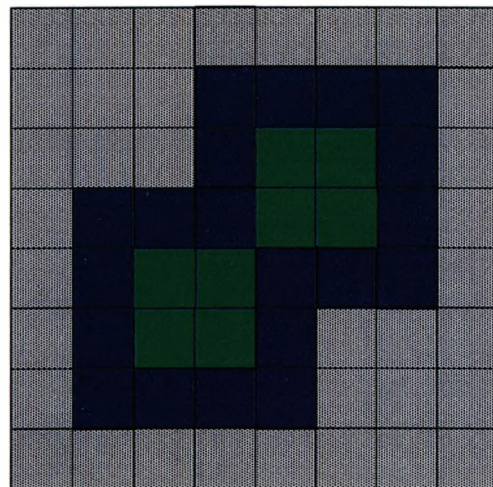
b

Figure 5.12a Two-dimensional section through a dumb-bell shaped void showing the erosion contours. High value erosion contours occur at the centres of pore bodies and low values at the pore throats (necks).

Figure 5.12b Three-dimensional contour of the lowest erosion level of the dumb-bell shaped void (with one end truncated for clarity). This illustrates the complex topology of the minima.



c



d

Figure 5.12c Diagram of the erosion of two pore bodies by the method of Baldwin *et al.* (1996). The colours represent different erosion levels within the image (the maximum erosion level is shown in red). This method has identified the two pore bodies by a single maxima located at the pore throat which is clearly incorrect.

Figure 5.12d Diagram of the erosion of the two pore bodies by the method used in this thesis. Two maxima have been identified (green) and are correctly associated with the pore centres.

5.4.3.1 Combining the results of the Pore-Characterization Algorithm with the Network Simulation Algorithm

The fully partitioned void-space model (fig. 5.13a) can now be analyzed to produce the data required by the network simulation. As discussed in section 5.3.1 the quantities required are the separation between pore bodies, l , the pore throat radius, r , and the topology of the network formed from the inter-connected pore bodies. As the model is voxel-based these quantities are relatively easy to calculate. The centre of a pore body can be calculated by assuming that it is given by the mean of the co-ordinates that compose the pore body, this is a reasonable approximation as in general pore bodies are convex objects. The topology of the network (see fig. 5.13b) can be extracted by searching the image for pore bodies that have pore throat interfaces lying next to each other. Once the topology and the centres of the pore bodies are known, the separation of inter-connected pore bodies, l , can be calculated. As discussed in section 5.3.2 the pore throat radius, r in equation 5.4, can be given by the channel radius, R_c , eq.[5.8]. The values of the area and wetted perimeter of a pore throat in eq.[5.7] are calculated by counting voxel surface areas. Combining equations 5.4, 5.7 and 5.8 then produces an equation for the hydraulic conductivity, that incorporates the parameters derived from the void-space characterization (where all symbols are as previously defined);

$$[5.11] \quad g = 2\pi \frac{\left(\frac{A}{P}\right)^4}{\mu l}$$

Alternatively equation 5.9 can be used with equation 5.4 to produce the following equation for the hydraulic conductivity, g :

$$[5.12] \quad g = \frac{A^2}{8\pi\mu l}$$

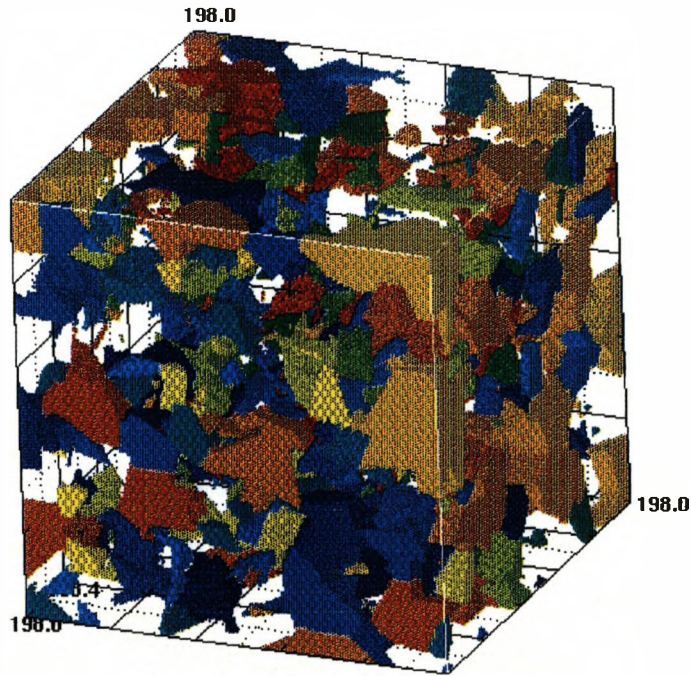


Figure 5.13a Fully partitioned void-space model (original void-space shown in fig. 5.10) . Different colours represent different pores within the void-space. The solid-matrix has not been displayed.

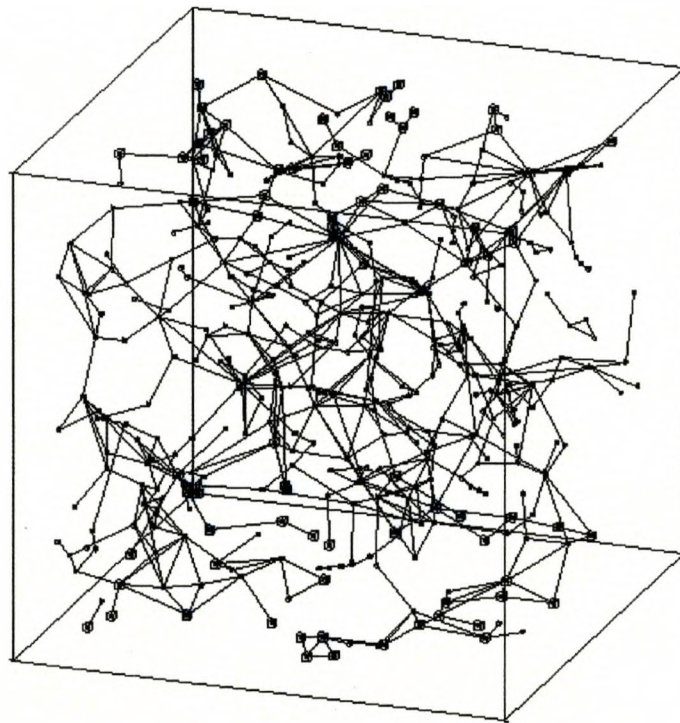


Figure 5.13b Topological network description of the void-space derived from the void-space partitioning model (fig. 5.13a). The small cubes represent pore-centres (nodes) in the network and the large cubes represent the centres of pores that are connected to either the upper or lower faces of the volume.

5.4.3.2 Calculating Absolute Permeability

It is now possible to solve the simultaneous equations specified by eq.[5.6] for the whole of the void-space network using Gauss-Seidel iteration (Kreyzig, 1993), if a steady-state pressure gradient is assumed.

The model volumes are rectangular prisms, therefore to specify the boundary conditions one face of the prism is assigned the pressure unity and the opposing face is assigned the pressure zero. The absolute permeability of the network, k , in eq. [5.1] is then given by;

$$[5.13] \quad k = \frac{Q_{total} \mu \Delta l}{A \Delta P}$$

Where Q_{total} (m^3s^{-1}) is the steady flow through the sample (equal to the flow out of the inlet face), A (m^2) is the cross-sectional area of the inlet and outlet faces, μ is the viscosity ($\text{kg}\text{s}^{-1}\text{m}^{-1}$), Δl (m) is the length of the sample and ΔP ($\text{kg}\text{m}^{-1}\text{s}^{-2}$) is the pressure difference across the sample (in this case, unity).

Unfortunately, the network representation of the void-space described previously contains dead-end branches (see fig. 5.14) which cause the permeability to be over-estimated in the calculations. This is because the pressure solutions converge to a weighted average of the initial pressure at the node at the beginning of the dead-end branches. To correct for this the dead-end branches must be removed.

5.4.3.3 Removal of Dead-End Branches in the Network Topology

The removal of dead-end branches from a network (pruning) is a topic in mathematical morphology (Serra, 1982). Unfortunately, although it is possible to create an algorithm that will remove dead-end branches from the void-space networks generated for porous media (Thovert *et al.*, 1993) the algorithms tend to fail at loops in the dead-end branches (see fig. 5.14). This can be illustrated by figure 5.15 where a pruning algorithm is applied to an image of a daisy. The algorithm correctly removes the dead-end branches (fig. 5.15 a-c) but terminates upon the closed loop at the top of the stalk (fig. 5.15 d). The solution implemented in this thesis is to remove the dead-end branches

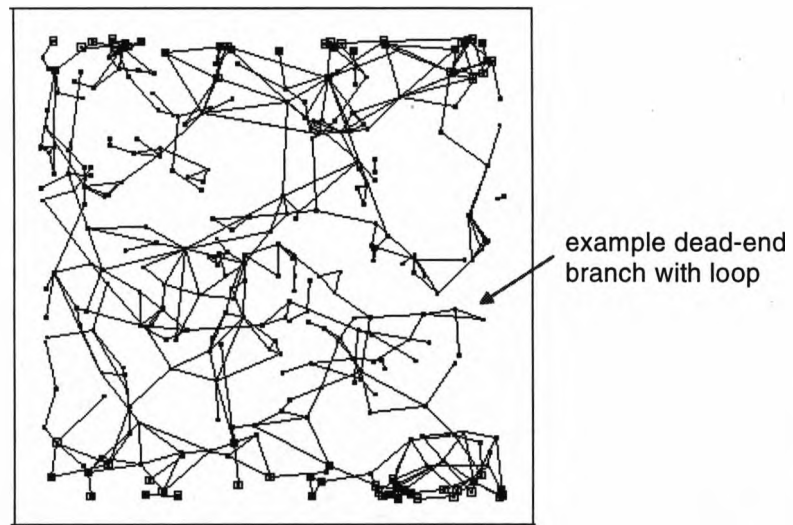


Figure 5.14 Network topology of the void-space (for clarity projected onto the x-z plane of the volume). This network clearly shows the presence of dead-end branches (example marked by arrow).

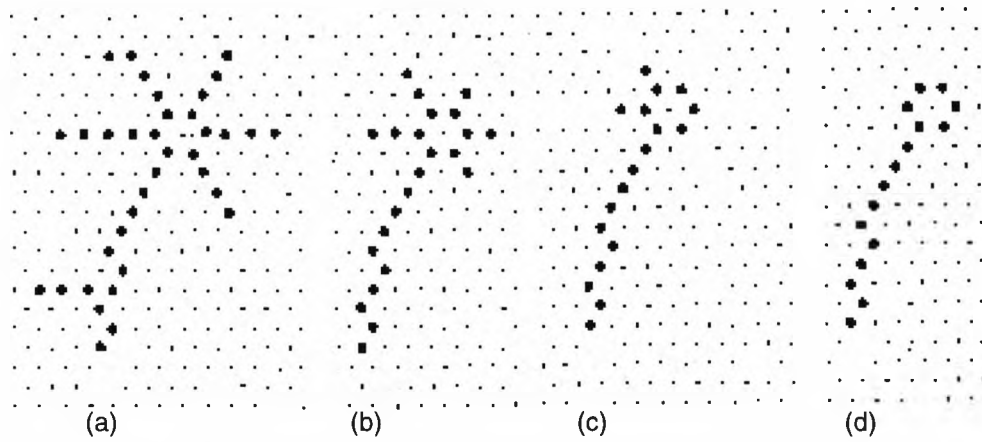


Figure 5.15 Removal of the dead-end branches on a daisy. Figures a-c show different steps in the iterative removal of points on the dead-end branches. Figure d shows termination of removal at the loop at the top of the stalk of the daisy (after Serra, 1982).

by modifying the network geometry. Each pore-throat connection is removed sequentially and the solution to the steady-state pressure field is calculated in the remaining pores. If a dead-end branch has been disconnected the pressure within the branch will fall to zero. It can therefore be identified and removed. This approach is rigorous and does not fail at loops in the dead-end branches. Unfortunately it is very demanding in C.P.U time due to the repeated calculation of the matrix of simultaneous equations describing the network. The algorithm is implemented in three main stages. Stage one (see fig. 5.16 a) is to calculate the steady-state pressure field with boundary conditions of zero on the upper face of the sample and unity on the lower face. All the dead-ends associated with the upper face can then be found by removing all the pores and associated throats in the network where the pressure field is zero. In stage two (see fig. 5.16 b) the boundary conditions are reversed so that the upper face is unity and the lower face is zero. The network has now had all the dead-end branches associated with either boundary face removed, but dead-end branches within the sample still remain. Stage three (see fig. 5.16 c) requires that the boundary conditions are changed to unity on the lower face and two on the upper face. A pore-throat within the network is then removed and the pressure field solved. If the removal of a pore-throat disconnects a dead-end branch the pressure within the pores of that branch falls to zero and therefore it can be removed from the network. Iteration over all the pore-throats in the network therefore results in the removal of all dead-end branches. Figure 5.17 a & b show a simple network generated from a simulated sample with a porosity of 0.13 ϵ before (a) and after (b) removal of the dead-end branches for flow in the z-direction. The permeability of the reduced network can now be calculated correctly using equation 5.13.

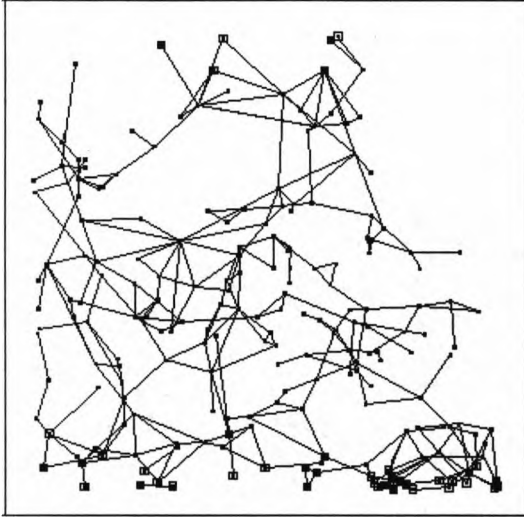
5.4.4 Calculation of the Electrical Conductivity

The calculation of the electrical conductivity of the porous medium is analogous to the calculation of the permeability except the governing equations are different.

Equation 5.3 for the flow rate between pores becomes;

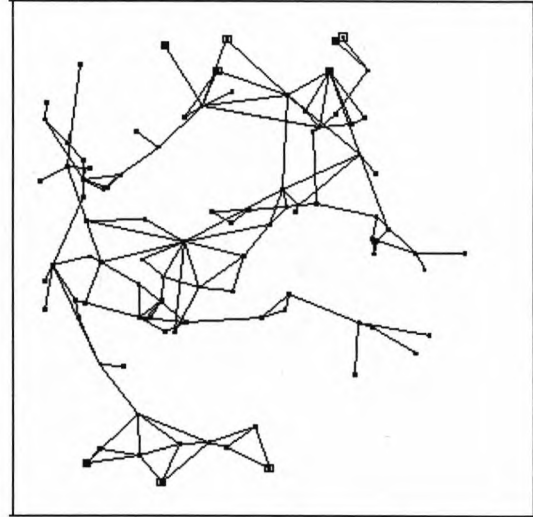
$$[5.14] \quad I = g\Delta V$$

Z axis - upper boundary condition is zero



a

Z axis - upper boundary condition unity

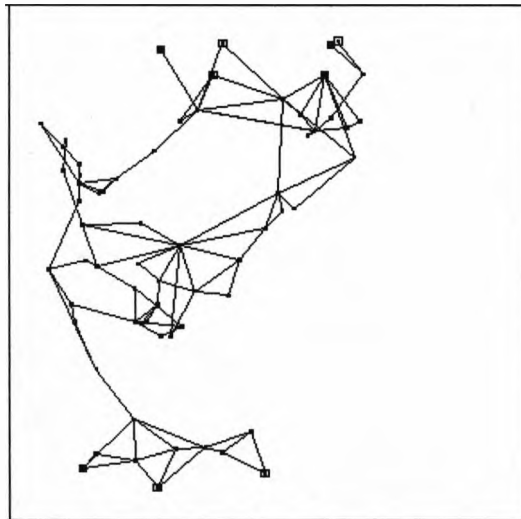


b

Z axis - lower boundary condition is unity

Z axis - lower boundary condition zero

Z axis - upper boundary condition is two



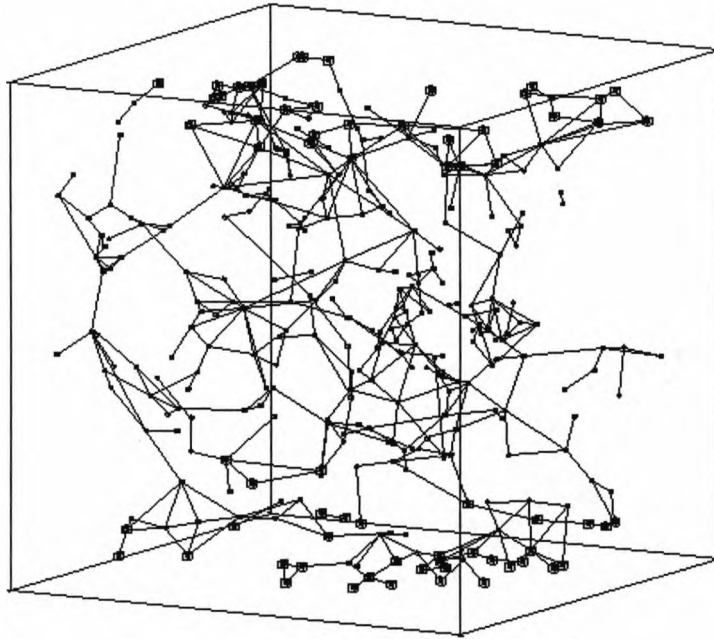
c

Z axis - lower boundary condition is unity

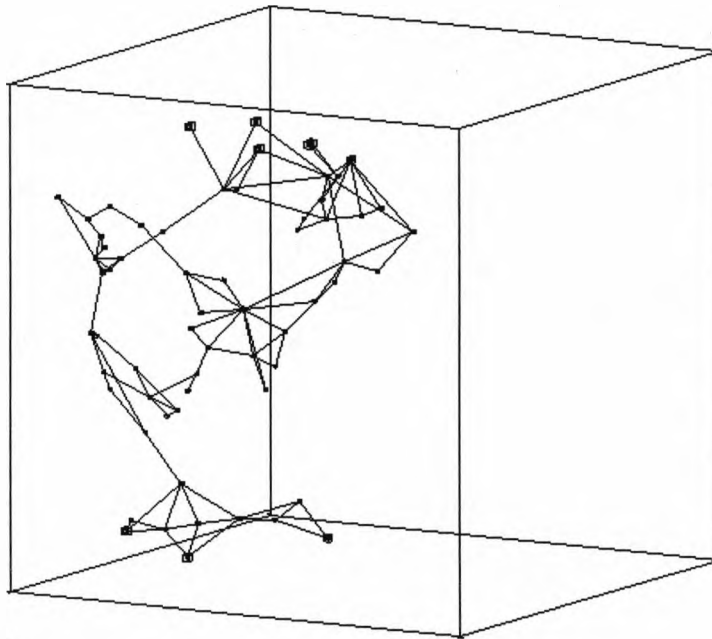
Figure 5.16a Network topology after stage one of the pruning process. Dead-end branches on the upper boundary have been removed.

Figure 5.16b Network topology after stage two of the pruning process. Dead-end branches on the lower boundary have been removed.

Figure 5.16c Final network topology after stage three of the pruning process. Dead-end branches on the network have been removed.



a



b

Figure 5.17a Network topology for a model porous medium with 0.13ε porosity before pruning.

Figure 5.17b Network topology for a model porous medium with 0.13ε porosity after pruning.

Where I (A) is the current, g is the bond conductance (Ω^{-1}) and ΔV (V) is the potential difference between the pore bodies.

To simplify the calculation of the bond conductance g , it is assumed that the matrix is insulating and therefore no conduction occurs on the surface of the matrix grains (as justified in section 5.0). This results in the following equation, for the bond conductance g ;

$$[5.15] \quad g = \frac{A\sigma_w}{l}$$

Where A (m^2) is the area of the constriction at a minima in the void-space, σ_w ($\Omega^{-1}m^{-1}$) is the conductivity of the fluid and l (m) is the separation between pore body centres. The form of this equation is based on the work of Roberts and Schwartz (1985) who showed that the resistivity of a pore body-throat-pore body sequence is dominated by the cross-sectional area of the narrowest section of the throat.

Finally, Darcy's law for the medium (equation 5.13) must be replaced by Ohm's law,

$$[5.16] \quad \sigma_e = \frac{\Delta l I_{total}}{A \Delta V}$$

Where σ_e ($\Omega^{-1}m^{-1}$) is the conductivity of the porous medium filled with conducting fluid, Δl (m) is the length of the sample between opposing faces, ΔV (V) is the potential difference across the sample (in this case, unity), A (m^2) is the cross-sectional area of the inlet and outlet faces and I_{total} is the steady current flow through the network (equal to the total current flow out of the inlet face).

The electrical conductivity and hence the Formation Factor can therefore be calculated using the same networks as the permeability calculations.

5.5 Testing the Algorithm

The algorithm naturally partitions into two calculations, that of the void-space characterization and that of the permeability/conductivity calculation. They can be tested in two ways. First, by checking whether the algorithms are self-consistent and second, by comparing the results calculated from the algorithms with experimental data.

5.5.1 Self-Consistency

The algorithm for void-space partitioning was tested by visual inspection of the results at each stage of the algorithm.

The algorithm for permeability/conductivity calculation was tested by comparing the results with simple networks, whose results could be calculated by-hand.

Once it was ascertained that each half of the algorithm worked separately they were then combined and used to investigate the permeability/conductivity of a natural sample with known properties.

5.5.2 Comparison with Experimental Results

Recent experimental advances in fields such as electron microscopy (Flegler, 1993), laser scanning confocal microscopy (Fredrich *et al.*, 1995), synchrotron-based X-ray tomography (Flannery *et al.*, 1987, Deckman *et al.*, 1989, Dunsmuir *et al.*, 1991, Kinney and Nichols, 1992) and nuclear magnetic resonance imaging (Baldwin *et al.*, 1996) have enabled high-resolution three-dimensional images of porous media to be obtained, which contain detailed information about the matrix and void-space micro-structural relationships of the samples. These methods are non-intrusive unlike, for example, serial-sectioning and therefore allow direct experimental measurement of quantities such as permeability/electrical conductivity to be carried out on the same samples.

5.5.3 Fontainebleau sandstone: case study

To compare the permeability/conductivity results derived from the void-space characterization with those measured experimentally, a sample of Fontainebleau sandstone was used. A three-dimensional image of this sample was obtained by using X-ray tomography (Schwartz *et al.*,

1994, Spanne *et al.*, 1994, Coker *et al.*, 1996) and was kindly provided by David Coker (Princeton). This sample was well characterized in terms of its permeability/conductivity by experimental measurements of permeability/conductivity (Schwartz *et al.*, 1994) and by theoretical attempts to calculate the permeability/conductivity; Spanne *et al.* (1994), calculated the permeability/conductivity using some unspecified technique and achieved reasonable comparison with the experimental values; Coker *et al.* (1996), used a statistical approach (see section 5.1 i) and calculated the permeability to within a factor of 1.6 of the measured value (see table 5.1 for summary) and the conductivity in terms of the Formation Factor to within a factor of 2.

The following paragraphs will describe the generation of the tomographic image used by the above researchers and its void-space characterization using the algorithm outlined in section 5.4.

Table 5.1 Summary of Calculated and Measured Permeability and Formation Factor (Electrical Conductivity) Values of a Fontainebleau Sandstone Sample

	Measured Value	Calculated Values from the Tomographic Image		
Reference	Schwartz <i>et al.</i> (1994)	Schwartz <i>et al.</i> (1994)	Spanne <i>et al.</i> (1994)	Coker <i>et al.</i> (1996)
Permeability, k (μm^2)	1.3	1.0	0.6-2.9	4.4
Formation Factor, F	22	38	26-54	11

X-ray tomography

The tomographic image of the Fontainebleau sandstone was generated using the National Synchrotron Light Source at the Brookhaven National Laboratory, USA (Flannery *et al.*, 1987). This consists of a highly collimated monochromatic 17 keV X-ray beam which is incident on the 3 mm diameter cylindrical specimen. This specimen was a core from a larger sample that had previously had its void-space filled with epoxy resin. A tomographic scan is achieved by rotating the sample in the X-ray beam and measuring the total attenuation for each ray passing through the sample. It is then possible using a suitable mathematical scheme to construct a map of the attenuation coefficients within a two-dimensional slice of the sample. These slices can then be stacked to produce a

three-dimensional tomographic image of the sample, composed of voxels with different attenuation co-efficients. However, as the attenuation co-efficients are a function of the average density within a given voxel within the sample, differentiating between matrix and void-space phases is not easy. This means that the attenuation histogram for a two phase material consists of an over-lapping bi-variate distribution. The peak at low attenuation co-efficients is caused by the air surrounding the sample, the middle peak is associated with the void-space and the peak at high attenuation co-efficients is related to the matrix. To extract a binary image from the tomographic image an edge-based segmentation algorithm (Coker and Lindquist, 1994) was used.

The result of the above procedures was to produce a binary volume image of the sample composed of $512 \times 512 \times 97$ $7.5 \mu\text{m}^2$ voxels with a value of one associated with the matrix and a value of zero with the void-space (fig. 5.18a).

Void-Space Characterization

To enable characterization of the void-space of the Fontainebleau Sandstone the largest possible rectangular volume was extracted from the binary image of the cylindrical sample. The void-space characterization algorithm was then applied to the sample (as discussed in section 5.3.2). Figure 5.18b is an image of the results of the void-space characterization of the Fontainebleau sandstone with individual pores assigned different colours and fig. 5.18c is a section through this image with the solid-matrix shown in blue.

Various parameters were extracted for comparison with previous measurements, such as the coordination number distribution, the throat-size distribution and the pore-size distribution. The coordination number distribution can be found by searching the void-space for all the interfaces between adjacent pore bodies. These interfaces represent the planes erected normal to the minima in the void-space (see fig. 5.7). Similarly, the throat-size distribution can be found by counting voxels at the interfaces between pore bodies. Determining the pore body size distribution is complicated by the fact that previous workers adopt different definitions of the pore radius (Bryant *et al.*, 1993, Doyen, 1988). However, in this work the definition of a pore radius, as the square root of the variance of the position vectors of the voxels within a pore body, as adopted by Baldwin *et al.* (1996) will be used as it is easily determined for a voxel-based model.

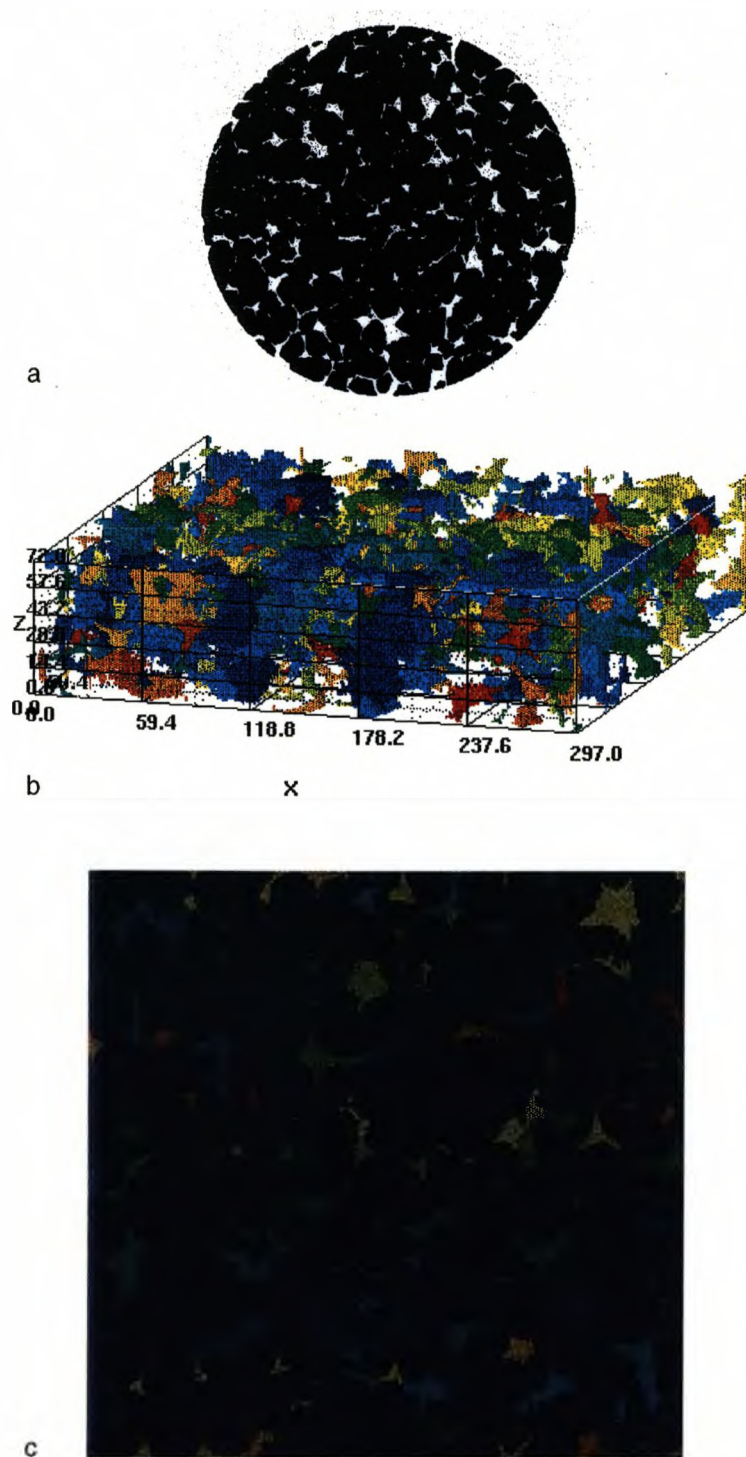


Figure 5.18a Binary image of solid-matrix of Fontainebleau sandstone with void-space removed. Diameter is 3 mm.

Figure 5.18b Void-space characterization of Fontainebleau sample with solid-matrix removed. The different colours represent different pores.

Figure 5.18c Section through the void-space characterization model of the Fontainebleau sandstone. Solid-matrix is in blue, individual pores are shown in different colours (NB: the similarity in colour of some of the pores is due to the limited colour palette on the unix workstation).

Unfortunately, the coordination number distribution has not previously been measured for Fontainebleau sandstone probably because available techniques for measuring the distribution, such as serial-sectioning and re-construction (Lin and Cohen, 1982) and multi-orientational scanning (Kwiecien *et al.*, 1990, Zhao and Macdonald, 1993, Zhao *et al.*, 1994) are very labour intensive. However, results from measurements made by Kwiecien (1987) on a Berea sandstone sample are available. As Berea sandstone is well-sorted and has a similar grain-size distribution to Fontainebleau sandstone it is probably an adequate analogue for qualitative comparison of coordination number distribution. Figure 5.19 shows a comparison between the coordination number distribution plot for Berea sandstone measured by Kwiecien (1987) and the results from the void-space characterization of the Fontainebleau sample. The average coordination number of the Berea sample is 2.9 and the average coordination number of the Fontainebleau sample is 3.4. No results are available for coordination numbers of zero and one, which represent dis-connected pores and dead-end pores, for the Berea sample. However, the results for a coordination number of zero for the Fontainebleau sample can be compared with a measurement of the difference between the total and effective porosity made on a Fontainebleau sample by Fredrich *et al.* (1993) as this represents the amount of disconnected porosity. The tomographic image of the Fontainebleau sample has of the order of three percent disconnected porosity. This is six times greater than that measured by Fredrich *et al.* (1993) and is due to the finite resolution of the tomographic image which means that pores below 7.5 μm cannot be resolved. Comparison of coordination numbers greater or equal to two show qualitatively similar distributions for the two samples with both samples exhibiting a small number of pores with very large coordination numbers. The void-space characterized tomographic image of the Fontainebleau sample generally has a greater number of high coordination pores and it has been suggested by Baldwin *et al.* (1996), that this is due to the strict definition of a pore throat (Dullien, 1991) adopted for the partitioning of the void-space. In fig. 5.20 one of these high coordination number pores (marked in figure) is visualized. It can be seen that the void-space in this region is complicated and this has led to the void-space being divided into a large number of pores resulting in the high coordination number measured. This is a result of the strict definition of a pore as defined by Dullien (1992) whether this is what the reader considers a pore or more importantly what the fluid

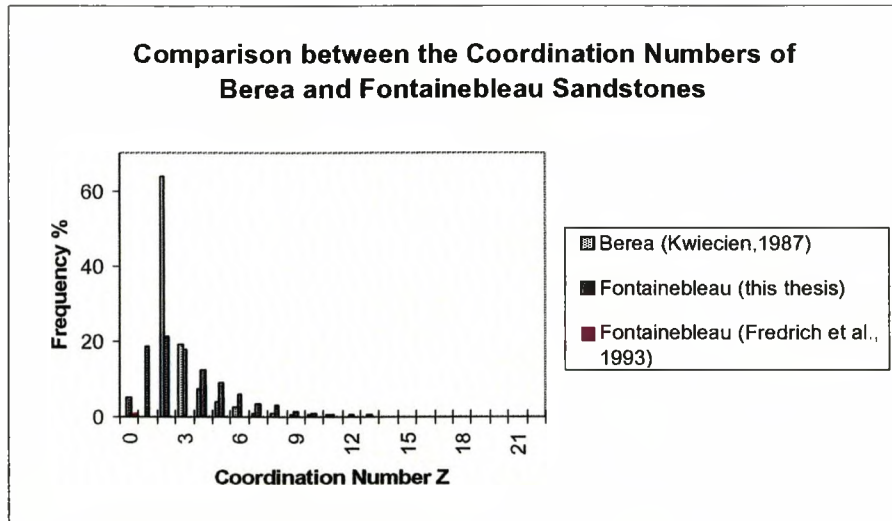


Figure 5.19 Comparison between the coordination number distributions of Berea (Kwiecien, 1987) and Fontainebleau sandstones (Fredrich *et al.*, 1993, this thesis).

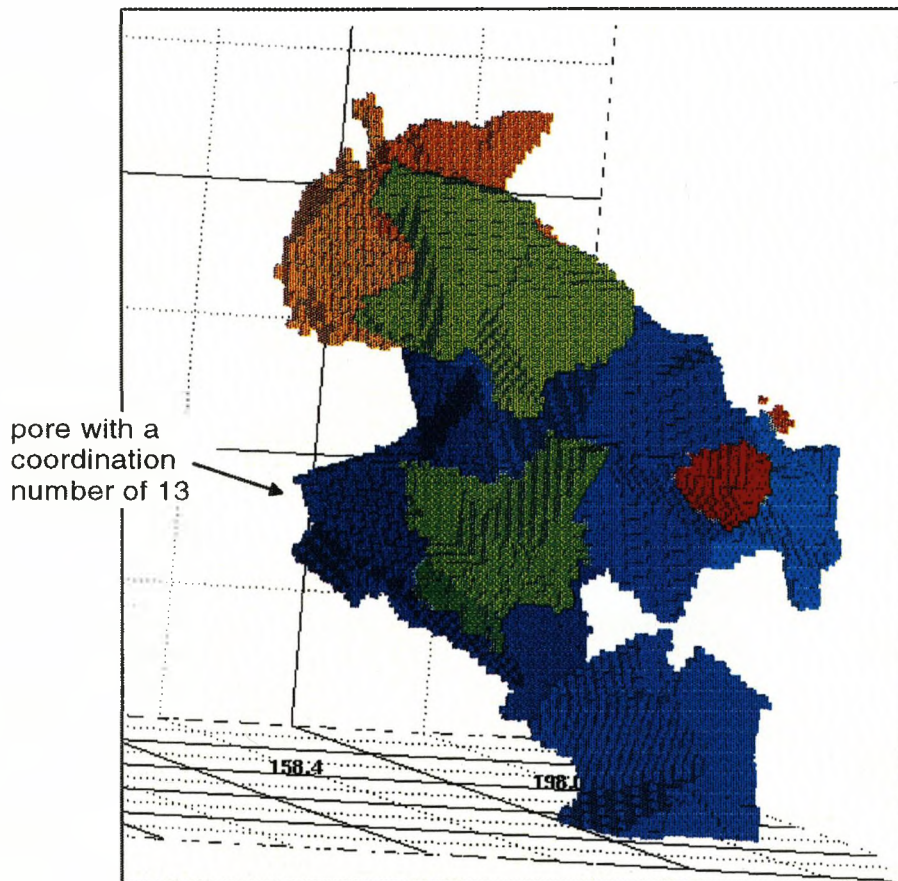


Figure 5.20 Visualization of a high coordination number pore extracted from a larger volume of the void-space.

flowing through the void-space considers a pore is open to conjecture! However, the results that follow suggest that it is a reasonable approximation.

Figure 5.21 shows a comparison between the distribution of pore radii generated from the square root of the variance of the voxels composing each pore after void-space characterization and the pore radii measured by Doyen (1988), on a series of thin-sections of Fontainebleau sandstone of slightly higher porosity (0.22 ϵ). Pore radii of $\leq 10 \mu\text{m}$ were neglected by Doyen (1988), as he considered them artifacts of his experimental preparation. Comparison of the available data shows a qualitatively similar distribution of pore radii with a slightly broader range for the higher porosity sample of Doyen as would be expected.

Finally, figure 5.22 shows a comparison between the distribution of pore-throat radii generated by the pore characterization algorithm and that measured by Doyen (1988). Both samples have a similar shaped distribution of pore-throat radii with the higher porosity sample having a broader distribution as would be expected. The above results indicate that the void-space characterization algorithm produces results consistent with previous measurements made on analogous samples.

Overall, although there are no directly comparable measurements of coordination number, pore-size distribution and pore-throat distribution available for the Fontainebleau sandstone sample used in this thesis by different techniques. It should be clear from the above comparisons with available measurements on different samples using different techniques that the results of the method used in this thesis are reasonable.

Network Simulation

A network simulation of the permeability/conductivity of the void-space characterized Fontainebleau sandstone sample was performed for each of the sample axes, the results of which are summarized in table 5.2.

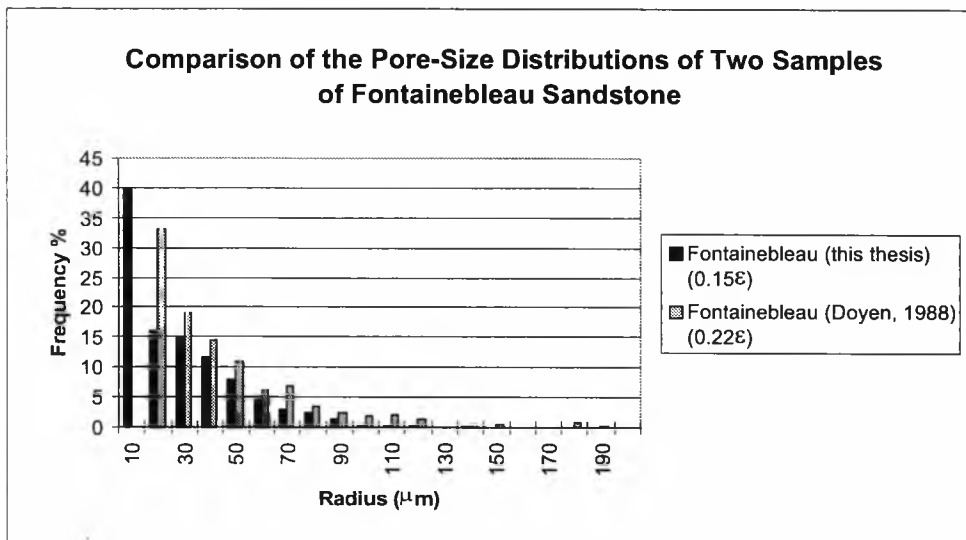


Figure 5.21 Comparison of the pore-size distributions of two samples of Fontainebleau sandstone.

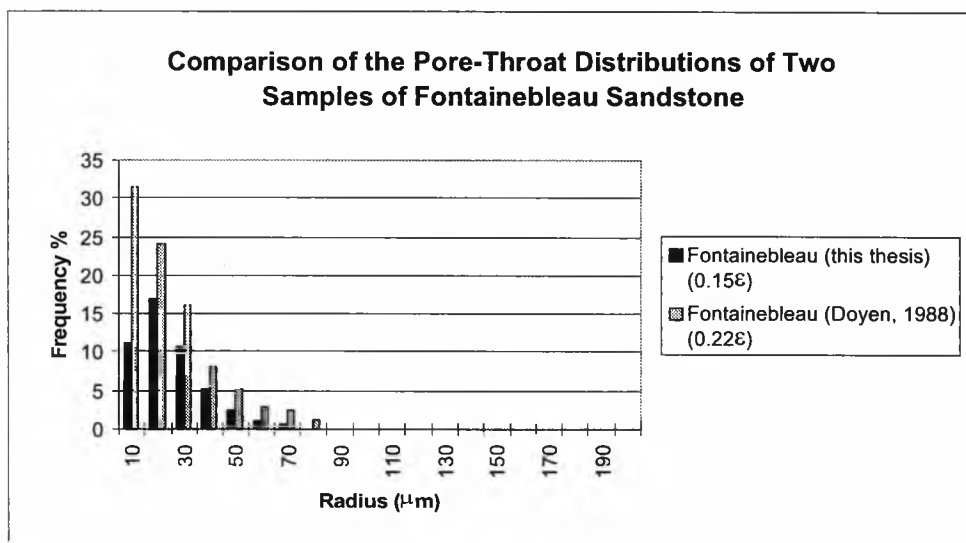


Figure 5.22 Comparison of the throat-size distributions of two samples of Fontainebleau sandstone.

Table 5.2 Summary of the permeability/Formation Factor calculated from the network simulation for different flow axes compared with the measured permeability/conductivity for a sample of Fontainebleau sandstone

Flow Direction	Calculated Values from the Network Simulation			Measured Value (Schwartz <i>et al.</i> , 1994)
	X axis	Y axis	Z axis	Unknown
Permeability, k (μm^2) using Eq. 5.11	0.05	0.06	0.03	1.3
Permeability, k (μm^2) using Eq. 5.12	1.1	1.4	0.7	1.3
Formation Factor, F	40	33	52	22

Using equation 5.12 (scaling flow with the area of the constriction squared) the x and y axes calculated permeability values show good agreement with the measured permeability value and are reasonably consistent considering the approximations involved in the calculation. They also compare favourably with previous work summarized in table 5.1. The z axis permeability is significantly lower than both other axes and the measured value. This is to be expected as the width of the sample is considerably shorter for the z axis. Using equation 5.11 (hydraulic radius) under-estimates the permeability by approximately two orders of magnitude and therefore is not an appropriate scaling for the hydrodynamic conductivity of the equivalent channels used in the permeability calculation. The results using equation 5.12 to scale the flow through the channels are corroborated by the experimental justification for equation 5.12 by Sederman *et al.* (1997) (section 5.3.2). The under-estimation of the measured permeability for the results calculated by using the hydraulic radius (section 5.3.2) as a scaling for the flow through a pore-throat is probably due to the shape dependency of the hydraulic radius for viscous flow (Happel and Brenner, 1973). In other words, pore-throat cross-sections that deviate significantly from circles result in an under-estimation of the flow rate through such throats.

The Formation Factor values show a similar agreement with previous work. However, it is interesting to note that all the direct simulations of the electrical conductivity (Schwartz et, 1994, Spanne *et al.*, 1994, this work) within the void-space tend to produce Formation Factors that are 1.5-3 times higher than the measured value. This means that the calculated conductivities are less than the measured values which suggests that surface conduction on the matrix grains may be significant in the Fontainebleau sample, possibly due to some clay content. However, the complication of modelling this effect is beyond the scope of this work and therefore the calculation of electrical conductivity will not be considered further.

5.6 Conclusions

A new method for characterizing the void-space of porous media and calculating their permeability and electrical conductivity has been presented in this thesis. Comparison with measured values for permeability from a sample of Fontainebleau sandstone suggests that the method produces comparable values for the magnitude of the calculated permeability. However, comparison of the measured values for electrical conductivity on the same sample of Fontainebleau sandstone with the calculated values produces a poor match. This may be due to the neglect of the surface conductivity of the grains in the simulation. Therefore the method will only be used to calculate the permeability of the simulated media generated by the algorithm described in Chapter 3. The results of the permeability calculations for several crystallization simulations are described in Chapter 6. The following is a summary of the major conclusions of this chapter:

- A new, general 3-D voxel-based method for characterizing the void-space of porous media has been developed.
- A network model for calculating the permeability/electrical conductivity has been combined with the void-space characterization method to produce a general method for calculating permeability/electrical conductivity in porous media. This method can be applied to much larger sample/model volumes than the only comparable method (Lattice Gas Automata).
- A 3-D tomographic image of a sample of Fontainebleau sandstone has been used to test the void-space characterization algorithm and permeability/electrical conductivity calculations. This

resulted in good agreement between calculated and measured permeability values and poorer agreement for electrical conductivity.

Chapter 6

The Permeability of Partially Molten Rocks

6.0 Introduction

A technique for determining the permeability of porous media has been described in Chapter 5 and in conjunction with the model of crystallization described in Chapter 3, it can be used to simulate the evolution of permeability in a wide variety of geological systems. For example, a knowledge of the evolution of permeability with porosity in texturally unequilibrated crystallizing systems is very important for understanding the evolution of magma chambers (Naslund and McBirney, 1996, Campbell, 1996, Hunter, 1996), dolomitization (Philips, 1991) and secondary mineral over-growth in sediments (Bryant and Blunt, 1992).

At the present time there is very little quantitatively known about the permeability of texturally unequilibrated crystallizing solid-fluid systems; in particular there are no published experimental determinations of permeability/porosity relationships for texturally unequilibrated crystallizing partially molten rocks. Therefore the use of the model described in Chapter 3 and the techniques for determining permeability described in Chapter 5 present the first opportunity for permeability/porosity relationships for realistic solid-fluid geometries to be generated for texturally unequilibrated crystallizing systems.

The evolution of the rock texture that occurs when a volume of melt, such as an igneous intrusion, crystallizes is very complex and is dependant on the styles of nucleation and growth of the crystals that form the texture (see Chapter 2). Homogeneous nucleation can produce two main forms of nuclei distribution; a *random distribution* of nuclei that grow to form crystals suspended in a viscous magma (a simple model of a granite); or a *settled distribution* of nuclei formed by the centres of crystals that were initially formed by homogeneous nucleation but then settled out of suspension (a simple model of an igneous cumulate). Heterogeneous nucleation, on the other hand, can form a wide

variety of nuclei distributions which are critically dependant on the distribution of the host material, such as impurities, intrusion walls and pre-existing crystals (Lofgren, 1980, 1983, Berkebile and Dowty, 1982) upon which the crystals nucleate. Once nucleation has occurred the texture then develops as a result of competing growth between the crystals. There is currently still much debate over the importance of crystal settling versus in situ crystallization (heterogeneous nucleation) as it is very difficult to extract the information required to distinguish between them from crystallized igneous rocks (Naslund and McBirney, 1996).

Only a single solid phase with either a random distribution or a settled distribution of nuclei will be considered in this thesis. This is because heterogeneous nuclei distributions are very dependant on the actual rocks being studied and such detailed study is beyond the scope of this thesis and because considering a single solid phase reduces the complexity in the evolution of the textures caused by different phases growing at different rates.

6.1 Permeability Results for the Simulations of Crystallizing Media

Three different solid-fluid geometries will be considered; a model composed of 900 cube-shaped crystals with a gravitationally settled nuclei distribution, which will be referred to as the *settled cube model*; a model composed of 900 cube-shaped crystals with a random nuclei distribution, which will be referred to as the *random cube model* and a model composed of 900 lath-shaped crystals with a gravitationally settled nuclei distribution, which will be referred to as the *settled lath model* (see section 3.3.1, section 4.1). The random cube model is representative of homogeneous nucleation within a melt and the settled models (cube and lath) are representative of a crystallizing mush formed by the gravitational settling of crystals from a melt. There are many more models that could be used (section 6.0), however, due to time constraints the three most general models were selected for investigation in this thesis.

6.1.1 The Determination of a Representative Volume (ReV)

It is important that the sample being studied/modelled is of a sufficient volume that the measurement of porosity is reproducible. For example, measurement of porosity on a number of sandstone samples may result in the sandstone having an average porosity of 0.15 ϵ normally

distributed with a standard deviation of 0.02ϵ . To assess the statistical variation in porosity of a random nuclei distribution, three models composed of 900 cube-shaped crystals were simulated. Each model consisted of the same volume (a cube), but had a different random distribution of nuclei and therefore a different distribution of porosity at the pore-scale. The porosity of each model was calculated for incrementally increasing volumes beginning at the centre of each model. As the sampled volumes become larger the local statistical variations in the three models decrease and all three models converge to a similar value of porosity. Figure 6.1 is a plot of sampled volume versus porosity. All the curves in figure 6.1 show an increase in sampled volume moving from left to right on the plot. It can be seen that the curves for the three random models (solid points) show a decreasing variation in porosity as the sampled volume is increased with the curves becoming approximately parallel between 60 % and 73 % of the total volume sampled. The largest volume available for the permeability calculations is therefore 73% of the total volume and a porosity of approximately 0.47ϵ . The further increase in porosity in all the curves after approximately 80 % of the total volume has been sampled is due to the edge-effect caused by crystals growing near the limits of the simulated volume (see section 3.3.2). The curves for the settled models for both cubes and laths (curves with crosses) are very different to the curves for the random cube models at low total volume sampled. This is because the crystals within the settled models are fairly uniformly distributed and therefore the porosity shows little statistical variation above approximately 20 % of the volume sampled. Figure 6.1 therefore shows that sampling approximately 73 % of the total volume results in a representative value for the porosity for both the random and settled models and also eliminates the edge effects.

6.1.2 The Permeability of the Models

Using the techniques outlined in Chapter 5, section 5.4, the permeability of the models with decreasing porosity due to crystallization was calculated. The permeability (given in units of voxels²) for the three principle axes are given in tables 6.1, 6.2, 6.3 for each model for a range of porosities. Calculating permeability for each of the axes of the models enables the degree of anisotropy due to variations in the pore-structure of the models to be assessed. The results given are based on using equation 5.12 for the hydrodynamic conductivity and therefore flow rate within the models is scaled

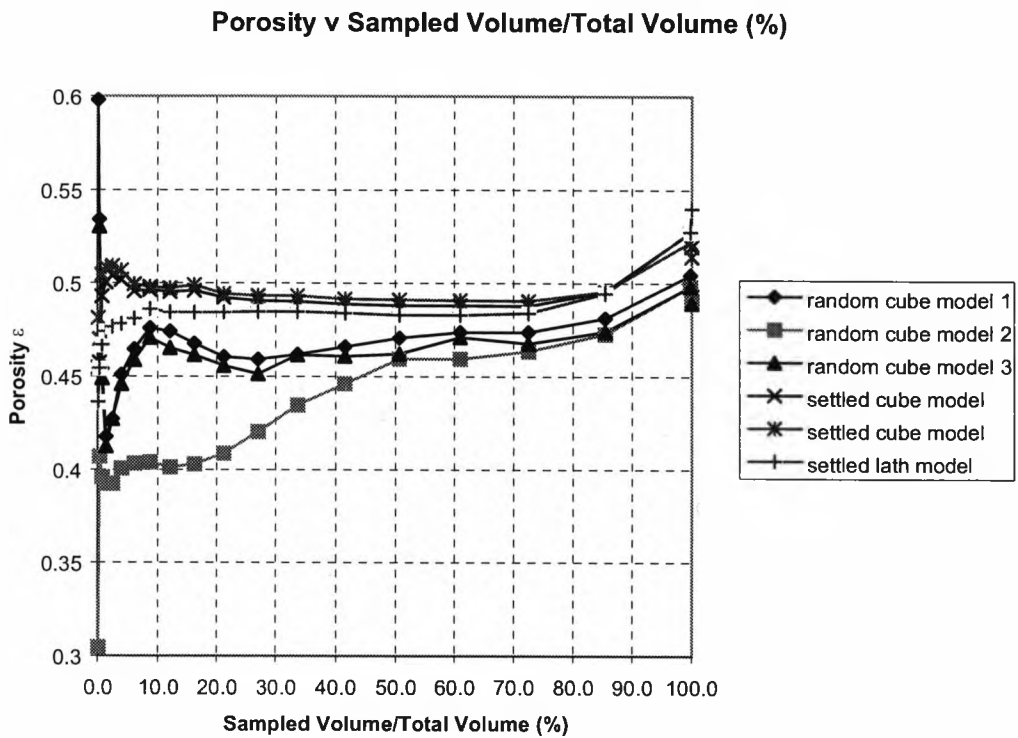


Figure 6.1 Plot of Porosity ϵ versus Sampled Volume/Total Volume (%) for the settled cube model, settled lath model and random cube model showing the variation of porosity with sampled volume for the simulations.

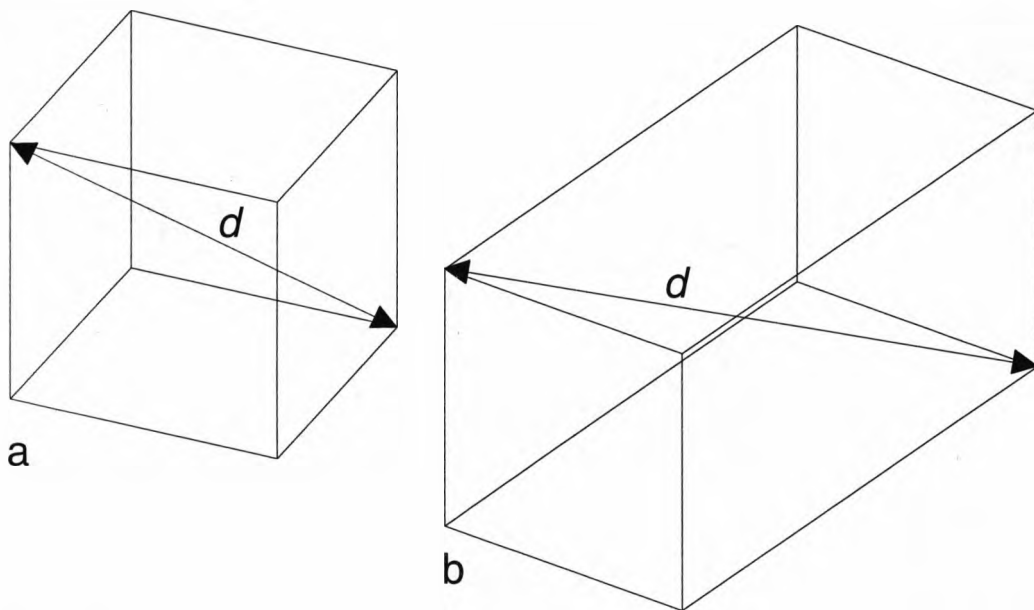


Figure 6.2a Diagram of a cube-shaped crystal showing maximum grain length d .
 Figure 6.2b Diagram of a lath-shaped crystal showing maximum grain length d .

by the area of the pore throats squared. The number of permeability calculations with changing porosity is limited by the width of each increment of growth on the crystals within the model. The width of an increment is constrained by the total number of voxels that compose the model for a given number of crystals within the model, which depends on the amount of computer memory available for the simulation, as discussed in section 3.2.3. It would be possible to increase the resolution of the decrease in porosity with crystallization by reducing the number of crystals within the volume, however, reducing the number of crystals within the volume would mean that it would not be possible to achieve a representative volume for the porosity of the random cube models. Therefore it is not possible to increase the resolution of the decrease in porosity with crystallization with the available computing facilities and due to the limited number of permeability/porosity values calculated no attempt has been made to curve fit the data points.

Table 6.1 Settled Cube Model (k_{scm}) Permeability (voxels²)

Porosity ϵ	k_{scm} X axis	k_{scm} Y axis	k_{scm} Z axis
0.327	3.70E-1	4.01E-1	3.14E-1
0.241	1.24E-1	1.29E-1	1.15E-1
0.169	2.12E-2	2.12E-2	1.90E-2
0.114	9.33E-5	1.01E-4	8.06E-5

Table 6.2 Settled Lath Model (k_{slm}) Permeability (voxels²)

Porosity ϵ	k_{slm} X axis	k_{slm} Y axis	k_{slm} Z axis
0.351	5.30E-1	5.03E-1	5.29E-1
0.261	2.11E-1	2.06E-1	2.25E-1
0.186	4.88E-2	4.65E-2	4.80E-2
0.126	1.15E-2	1.05E-2	1.05E-2

Table 6.3 Random Cube Model (k_{rcm}) Permeability (voxels²)

Porosity ϵ	k_{rcm} X axis	k_{rcm} Y axis	k_{rcm} Z axis
0.327	1.14	1.03	9.07E-1
0.277	4.76E-1	4.20E-1	3.96E-1
0.231	2.15E-1	1.96E-1	1.90E-1
0.191	8.97E-2	8.96E-2	8.51E-2
0.155	5.22E-3	5.15E-3	4.89E-3
0.125	1.38E-4	1.32E-4	1.29E-4

6.1.3 Scaling of the Permeability Results

Permeability has S.I. units of metres squared, therefore to enable comparison between the results presented in this thesis and experimental measurements of permeability the length of the voxels in the simulation must be defined in S.I. units. The usual scaling for permeability measurements is based on the maximum grain length before impingement of grains has occurred (Bryant and Blunt, 1992). If it is assumed that the maximum grain length for a crystal represented by a cube or a lath is d (m) (see fig. 6.2 a & b), this can be used to find the actual volume of a crystal V (m^3) with a maximum length d (m) by simple geometry. If the number of voxels within a crystal within the simulation are known then the length of one voxel v (m) can be found. The relation between d^2 and v^2 then gives the scaling factor for the permeability of the cube (Sc_c) and lath (Sc_l) based models as:

$$[6.1] \quad Sc_c = (1.0E - 3)d^2$$

$$[6.2] \quad Sc_l = (5.0E - 4)d^2$$

Where Sc is the scaling factor (m^2) and d is the maximum grain length (m). Comparison can now be made to other measurements by specifying a grain-diameter d in equations 6.1 and 6.2 and multiplying the results given in tables 6.1-6.3 by this value.

6.1.4 Sources of Error in the Calculation of Permeability

There are three main sources of error within the permeability calculations presented in this thesis:

i) Finite Sample Size

Finite sample size within the models results primarily in statistical uncertainties in the calculated values of permeability and porosity. Section 6.1.1 addresses the problem of finite sample size for the calculation of porosity and concludes that the simulation volume is great enough to produce a representative value of porosity. Section 6.1.4 concludes that the simulation volume is

large enough to give a representative value for permeability as the calculated permeability values for all three principal axes of the models are similar.

ii) Model Assumptions

The assumptions used to develop a network model of the permeability are discussed in section 5.3 onwards. Although they are not rigorous representations of the fluid flow within a porous medium they are commonly accepted for the calculation of permeability (see section 5.1vi) in real porous media. This is because the complexity of the void-space within real porous media precludes the use of exact methods (see section 5.11). The assumptions used in this thesis have been tested by calculating the permeability of a tomographic image of Fontainebleau sandstone for which experimental measurements of permeability were available (see section 5.5.3). This produced good agreement between the calculated and measured permeabilities which suggest that the assumptions made in the calculations are valid.

iii) Digitization

Finite resolution in any digitized representation of real materials will affect the permeability calculations, this will result in shifts in the calculated values. For a given grain-size the Fontainebleau sandstone sample and the simulations presented in this thesis have approximately the same resolution. The good agreement between the measured and calculated values of the permeability for the Fontainebleau sandstone sample suggests that the resolution is adequate. Similarly the good agreement with permeability measurements made on sphere packs (see section 6.3.1) suggests that the resolution within the simulations is also adequate.

6.1.5 Permeability-Porosity Relationships for the Three Different Models.

Figure 6.3 shows plots of the permeability against porosity relationships for the three models described previously, where the results have been scaled to a grain-size of 1 mm. The vertical black line in all the plots indicates the minimum value ($\sim 0.08 \epsilon$) for the percolation threshold (defined as the point of onset of permeability) for all the simulations at the available resolution of porosity. It is important to note that the resolution of the simulation is currently limited to about 0.05ϵ sampling increments in porosity due to the limitations imposed by the available computer memory. Therefore

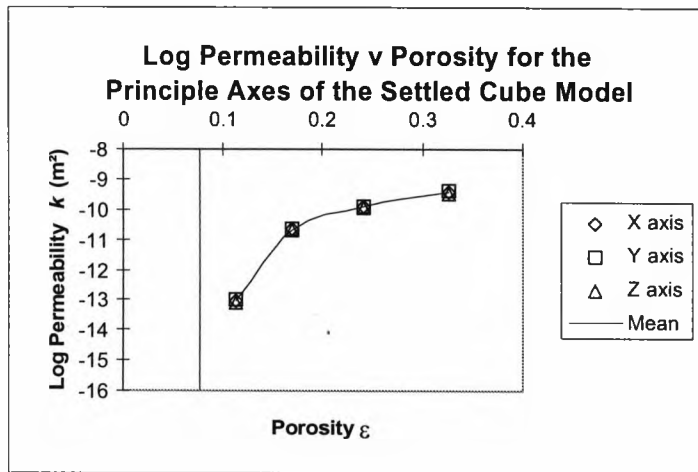


Figure 6.3a Plot of log permeability against porosity for the principal axes of the settled cube model. Vertical black line represents the percolation limit of the simulations at the current resolution (see section 6.2.3)

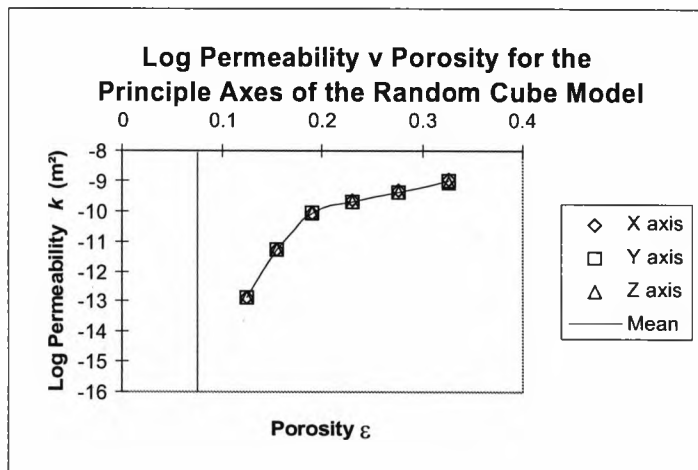


Figure 6.3b Plot of log permeability against porosity for the principal axes of the random cube model. Vertical black line represents the percolation limit of the simulations at the current resolution (see section 6.2.3)

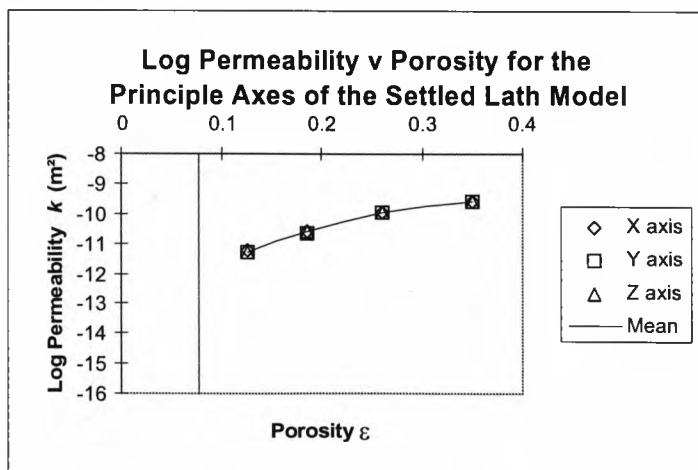


Figure 6.3c Plot of log permeability against porosity for the principal axes of the settled lath model. Vertical black line represents the percolation limit of the simulations at the current resolution (see section 6.2.3)

higher resolution in porosity may increase the value of the percolation threshold towards the last measurement before percolation ceases in the simulations.

In figure 6.3a the three principal axes for the settled cube model are plotted. It can be seen that there is good agreement among the three axes and that the curve through the mean of the points shows a similar shape to those shown in section 5.0, figure 5.1a. The down-turn in permeability occurs at about 0.18 ϵ porosity and the percolation threshold lies between 0.08 ϵ and 0.11 ϵ porosity. Figure 6.3b is a plot of the results for the random cube model. The permeability results are very similar to the settled cube model except that the initial permeability at 0.32 ϵ porosity is approximately half an order of magnitude greater for the random cube model. Figure 6.3c is a plot of the results for the settled lath model; this shows a different permeability/porosity relationship with decreasing porosity to the other two models. In the settled lath model the permeability decreases smoothly with no apparent down-turn in permeability with reducing porosity. This anomalous behaviour is probably due to a steep down-turn in the permeability before the percolation threshold that cannot be sampled at the current resolution of the simulation. It should be noted that all three models are isotropic for permeability and therefore the simulation volumes are large enough to allow the calculation of representative permeability values..

6.2 Comparison of the Permeability Results for the Simulated Crystallizing Media with Experiment and Theory

The permeability/porosity results for the three models will first be justified by comparing them directly with the experimental and theoretical work on related systems from the disciplines of chemical engineering and physics as no direct experimental or theoretical comparisons are available for crystallizing systems in the earth science literature. This is because the time and length scales involved in the crystallization of igneous systems preclude direct experimentation on melts at magmatic temperatures (Naslund and McBirney, 1996). Once the results have been justified; they can be used to predict permeability in crystallizing igneous systems (section 6.2.2).

6.2.1 Comparison of the Permeability of the Simulated Crystallizing Media with Theoretical and Experimental Work on Sphere Packs

It is natural to compare the settled cube models with random packings of monodisperse spheres because the crystal centres in the simulations are based upon the sphere centres in a dense random packing of touching spheres (Finney, 1968) and there are available experimental measurements of the permeability of sphere packings. Although it would be more desirable to compare the results with a random packing of cubes, no grain centre distributions or permeability measurements are available for such a packing. In addition, Bryant and Blunt (1992) have calculated the permeability for the over-growth of a dense random packing of touching spheres (see section 5.1vi) and this is therefore directly comparable with the settled cube model.

Figure 6.4 is a plot of the permeability/porosity results for the three simulated models compared with experimental measurements of permeability on random sphere packs (Ergun and Orning, 1949, Beavers *et al.*, 1949, Chu and Ng, 1989) and theoretical calculations of permeability on an over-grown sphere pack (Bryant and Blunt, 1992). The curve for over-grown spheres (black line with +) is scaled to the measured permeability for a pack of 1 mm diameter spheres at 0.36 ϵ porosity. It exhibits two distinct power-law behaviours (see section 5.0) with a change in slope occurring at about 0.1 ϵ porosity and has a percolation threshold at approximately 0.03 ϵ porosity (Bryant and Blunt, 1992).

The settled cube model (black line with black squares) can be compared directly with the results for over-grown spheres. The magnitude of the permeability for the cubes is slightly less than for the spheres at porosities greater than about 0.18 ϵ which seems reasonable. The down-turn in permeability occurs earlier than for the spheres, at about 0.18 ϵ porosity, as compared with 0.1 ϵ porosity for the spheres and the percolation threshold has a minimum value of approximately 0.08 ϵ porosity. This value is a minimum because it is the porosity value at which percolation ceases (and therefore the medium becomes impermeable) in all the simulations at the current resolution of porosity. Higher resolution in porosity may therefore increase the value of the percolation threshold nearer to 0.11 ϵ porosity which is the porosity of the last measurement before percolation ceases in the case of the settled cube model.

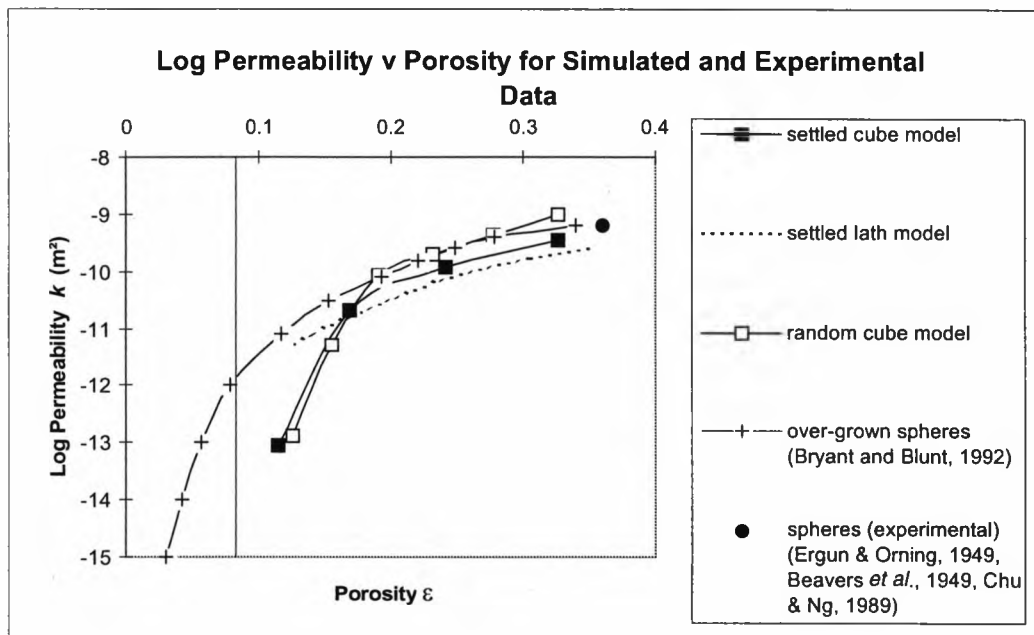


Figure 6.4 Plot showing a comparison between the simulated and experimental log permeability results for a grain size of 1 mm. Vertical black line represents the percolation limit of the simulations at the current resolution (see section 6.2.3).

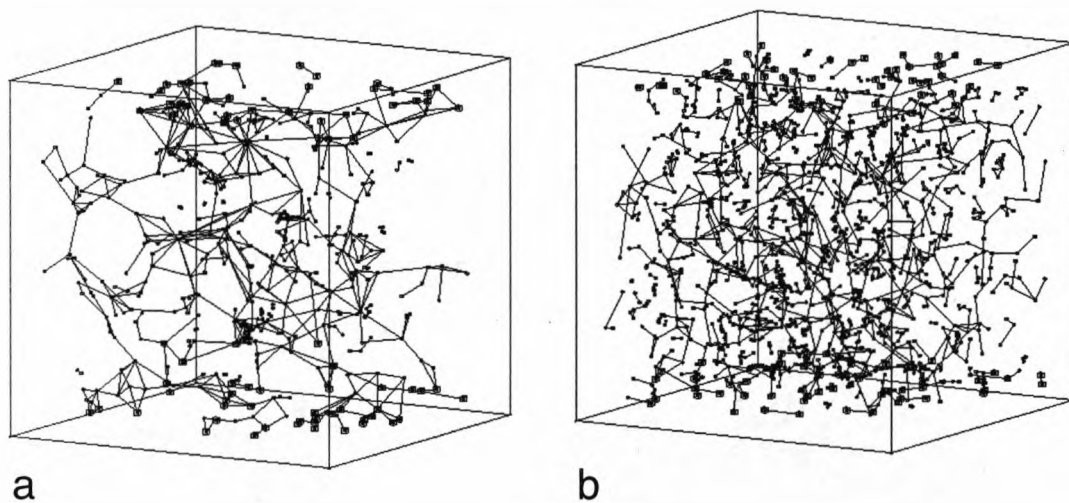


Figure 6.5a Network topology before pruning for the random cube model at approximately 0.11 ϵ porosity.

Figure 6.5b Network topology before pruning for the settled cube model at approximately 0.11 ϵ porosity.

The random cube model shows a closer match to the over-grown sphere model at porosities greater than 0.18 ϵ apart from a slightly higher permeability at 0.33 ϵ porosity. At porosities <0.18 ϵ it follows a similar trend to the settled cube model. The similarity between the two cube models suggests that the nuclei distribution does not have a strong affect on the permeability during over-growth, even though it produces void-space networks with dramatically different topologies (see fig. 6.5 a & b) at equivalent porosities. A similar poor correlation between permeability and variations in nuclei distribution has been shown by Coelho *et al.* (1997) for random packings in general, in which all the packs show similar permeabilities at similar porosities.

The settled lath model (black dotted line) shows a different permeability /porosity trend to the cube models with a lower magnitude of permeability and a similar shaped curve to the over-grown spheres. However, it must cease to percolate before the limit shown by the vertical black line in figure 6.4, therefore the down-turn in permeability is probably too steep to resolve as discussed earlier (section 6.1.5). This model is probably the least physically representative because it is based on the over-growth of a packing formed by equant particles with an inequant crystal shape. Unfortunately, a crystal centre distribution for a suitable packing of laths is not available and due to the anomalous nature of this curve at the current resolution of the simulation it will not be considered further.

Overall, the permeability results for the simulated crystallizing media are in good agreement with analogous work on spheres. The main difference between the results is the trend of the curves at low porosities (< 0.18 ϵ). The difference in the permeability/porosity trends between the cube models and the lath model presented in this thesis must be due to the inequant shape of the laths. However, due to the difficulty of inspecting the complex void-space geometries that control the permeability within the models this must remain conjecture. Similarly, the differences between the simulations presented in this thesis and the over-grown spheres are probably due to the shape of the crystals, this will be discussed further in section 6.2.2.

6.2.2 The Permeability of Crystallizing Igneous Systems

The random cube model (section 6.1, 6.2.1) is the initial step towards a model of crystallization in a simple conceptualization of a granite (section 6.0). However, as only one crystal

phase is considered, the application of this model to granites is probably limited. To improve this model, information about the evolution of textures in granites would be required, such as provided by Bryon *et al.* (1996). However, modelling of a more complex system although feasible is beyond the scope of this thesis. The settled cube model and the over-grown sphere model are, in contrast, reasonable analogues for crystallization of a layer composed of settled crystals within a volume of melt (section 6.0) and by comparing them with the textural equilibrium models (Von Bargen and Waff, 1986, Cheadle, 1989), predictions of the permeability of this system under non-equilibrium and equilibrium conditions can be made.

Theoretical curves for the permeability/porosity trends of isotropic systems in textural equilibrium (Von Bargen and Waff, 1986, Cheadle, 1989) are compared with the results for the settled cube model and the over-grown sphere model in figure 6.6. At porosities of greater than 0.18 ϵ the settled cube model (black line with white squares) and the equilibrium model (black line with white circles) of Cheadle (1989) have the lowest permeabilities for a given porosity. The over-grown sphere model (black line with +) has the largest permeability, however, the equilibrium model should have the largest permeability because the minimization of surface energy within the model should result in channels that are larger than the equivalent channels for a sphere pack. Therefore the equilibrium model is slightly in error at higher porosities. Despite this, it should be noted that the permeabilities of all three models are close to the permeability of a random sphere pack at large porosities as would be expected with at most a one quarter of an order of magnitude difference in the permeability.

The different permeability/porosity trends of the three models shown in figure 6.6 have two different causes. The non-equilibrium models (spheres and cubes) have different onsets in the downturn of permeability and different percolation thresholds due to the difference in the shape of the crystals for a given volume. This is because, for an identical volume crystal, a cube shaped crystal has a greater maximum length than a sphere and therefore a greater chance of contact with neighbouring crystals. If a crystal has a large maximum length for a given volume then it is more likely to block the flow channels between neighbouring crystals and this is what causes the downturn in permeability. Proof of this conjecture requires a simulation of a crystal with a maximum length for a given volume between that of a cube and a sphere. This would require an equant crystal

Log Permeability v Porosity for Theoretical Textural Disequilibrium and Equilibrium Models

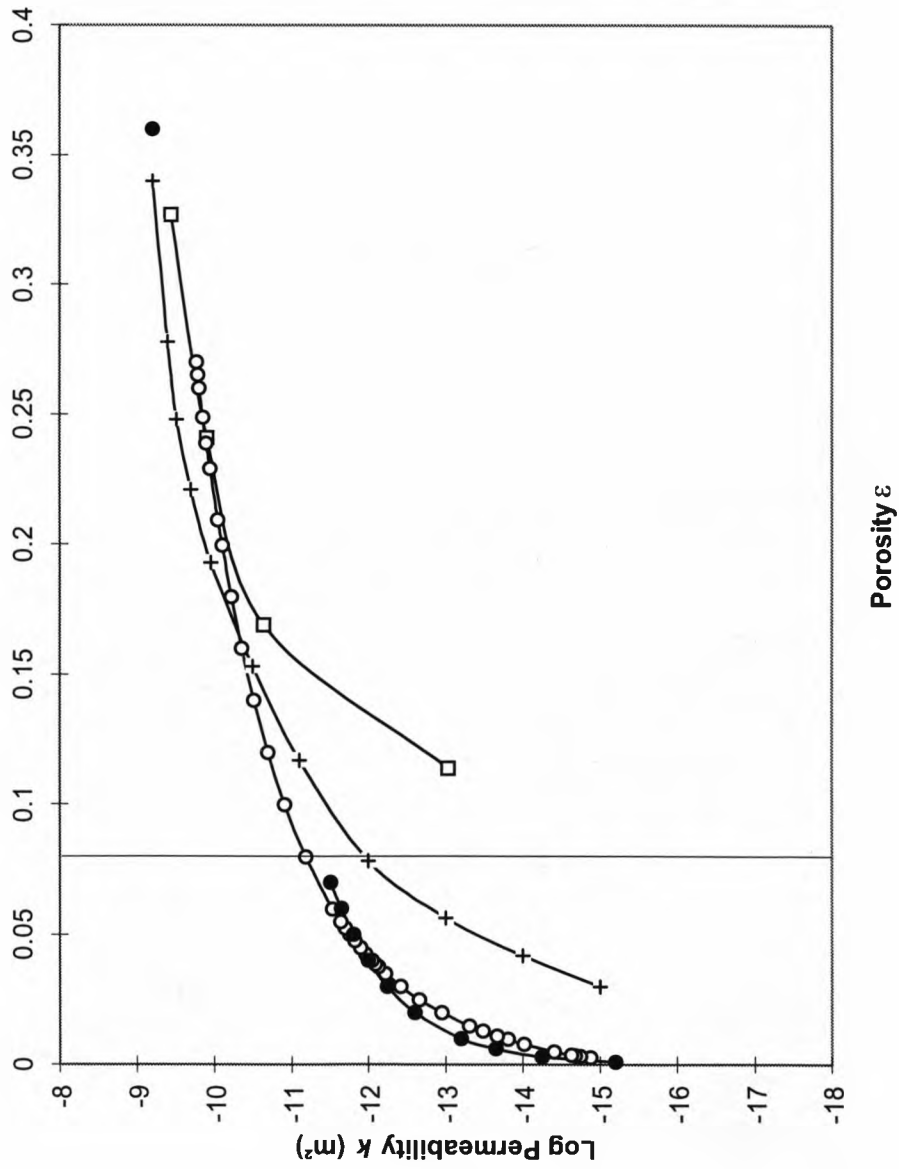


Figure 6.6 Plot showing the comparison between the log permeability/porosity of theoretical texturally disequibrated and equilibrated media for a grain-size of 1 mm. Vertical black line represents the percolation limit for the settled cube model at the current resolution.

with a greater number of facets than a cube, however, available computing power currently precludes this. The difference in the permeability/porosity trends between the unequilibrated models and the equilibrated models is because the minimization of surface energy in the case of the equilibrium models results in a higher permeability at low porosities for dihedral angles less than 60° . This is because the channel throat areas are larger than for the unequilibrated models and there is no percolation threshold because all the throats remain open down to vanishingly small porosities. Comparison of the permeability results for the equilibrium case from Von Barga and Waff (1986) and Cheadle (1989) show that Von Barga and Waff (1986) over-estimate permeability slightly at porosities less than 0.04ϵ and under-estimate at porosities greater than 0.04ϵ . This is because Von Barga and Waff (1986) used a channel geometry symmetry unit that cannot form a connected network and therefore they under-estimated the porosity, whereas Cheadle (1989) corrected for this.

Overall, the permeability/porosity results are consistent between the unequilibrated crystallization models and the equilibrium models and both show good agreement with the well-constrained experimental measurements of the permeability of sphere packs.

6.2.2.1 Implications

Figure 6.7 shows the idealized permeability /porosity relationship predicted for a cooling partially molten rock (based on figure 6.6). The previous sections have shown that the permeability/porosity relationships within a cooling partially molten rock are weakly dependent on grain-shape, nuclei distribution and degree of textural equilibration at porosities greater than approximately 0.18ϵ for the models investigated in this thesis. At porosities less than 0.18ϵ several different permeability/porosity relationships are evident. The difference between the two non-equilibrium models (spheres and cubes) has been interpreted as being due to differences in the shape of the crystals for a given crystal volume. Figure 6.7 shows that as the maximum grain length for a given crystal volume is decreased, then the percolation threshold moves to the left on the plot towards lower porosities. The minimum percolation threshold occurring at approximately 0.03ϵ for an over-grown packing of spheres. The dotted vertical lines show the increase in permeability that would occur if the unequilibrated systems became texturally equilibrated. This increase in permeability would occur at constant porosity unless combined with compaction (Hunter, 1996) of

Plot of Log Permeability v Porosity for Theoretical Textural Disequilibrium and Equilibrium

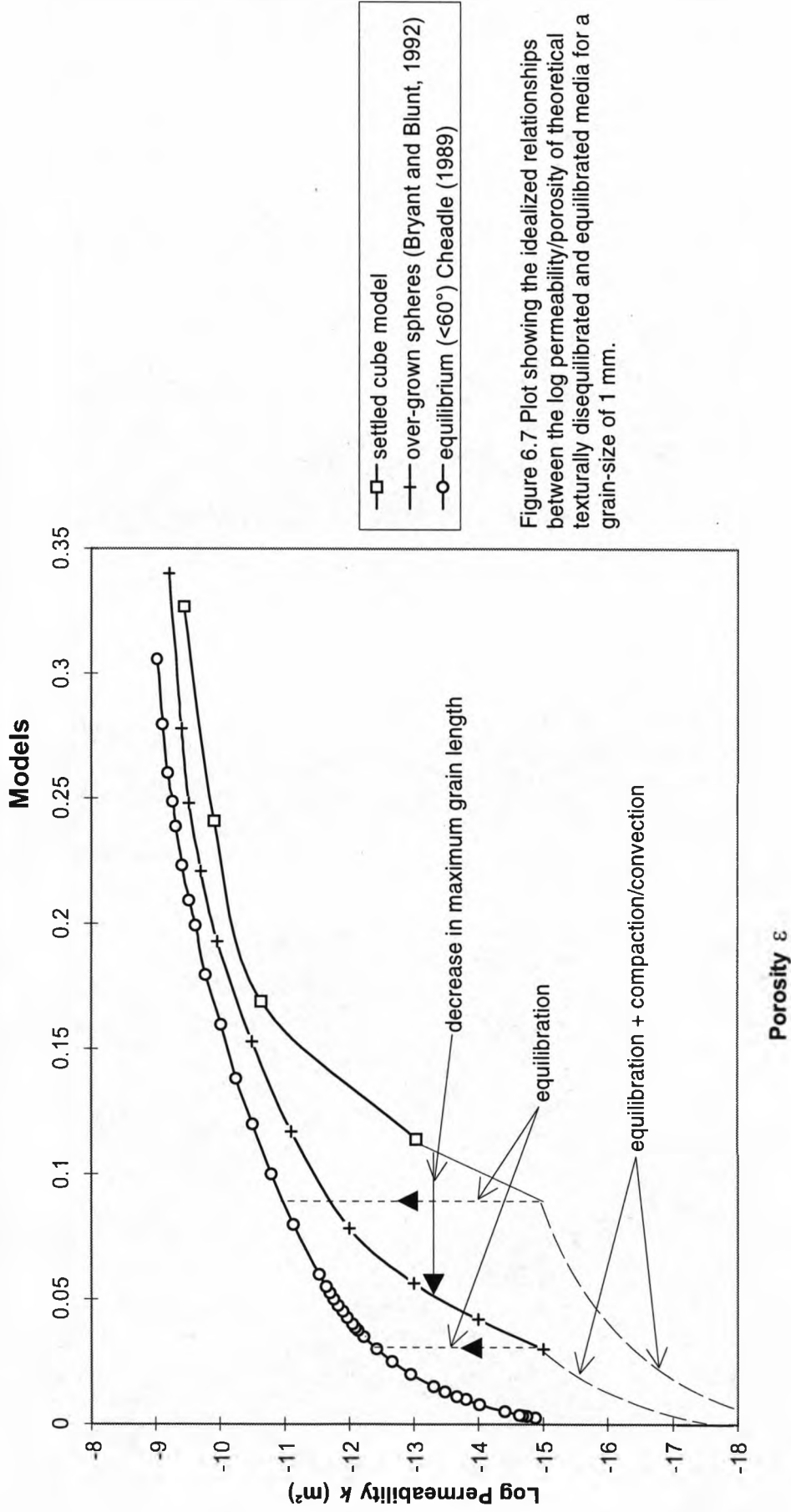


Figure 6.7 Plot showing the idealized relationships between the log permeability/porosity of theoretical texturally disequilibrated and equilibrated media for a grain-size of 1 mm.

the crystals and/or convection (Campbell, 1996) of the fluid within the porous medium. This is because textural equilibration itself does not result in porosity change, just a re-distribution of existing porosity to produce a lower total interfacial energy for the system. The lines on the plot are schematic and only show two of the many possible results of equilibration occurring. Equilibration could occur at any porosity resulting in a vertical increase in permeability on the plot. The magnitude of the permeability increase would be equal to the difference in permeability of the equilibrated and unequilibrated curves. The slashed curved lines on the other hand, show some of the many possible trends for a combination of equilibration and compaction/convection. The starting point of these equilibration and compaction/convection trends depends upon the porosity in the unequilibrated system when compaction/convection and equilibration are initiated. The implications of this are that for a monomineralic rock such as an olivine adcumulate to form in a system similar to the model, both compaction and/or convection and equilibration must be occurring at the same time. This is because if isolated pockets of melt form at high porosities ($> 0.11 \epsilon$) then different phases will crystallize within these pockets as the system cools. Equilibration prevents isolated pockets occurring and compaction and/or convection allow homogeneous mixing of the fluid within the system, thereby allowing sufficient transfer of the components required to form the crystals from an external reservoir of melt.

6.3 Conclusions

Permeability/porosity relationships for simulated crystallizing media have been presented which show good agreement with other theoretical results and experimental measurements in simple systems. The simulations have been used to model permeability/porosity in two different single crystal phase igneous systems; a system with a homogeneous nuclei distribution and a system formed from the over-growth of a settled nuclei distribution of pre-existing crystals. This has resulted in predictions for permeability/porosity in crystallizing igneous systems that has not previously been possible. A major implication of these results is that it is only possible to crystallize monomineralic rocks from a melt if compaction and/or convection and hence textural equilibration is occurring. The following is a summary of the major conclusions of this chapter.

- Permeability/porosity trends are weakly dependant on nuclei distribution.

- Permeability/porosity trends above 0.18 ϵ are only weakly dependant on grain shape and degree of equilibration for the models investigated in this thesis.
- Permeability/porosity trends below 0.18 ϵ are strongly dependant on grain shape and degree of equilibration.
 - Equilibration results in very low percolation thresholds (<0.01 ϵ).
 - Grain shape results in a range of percolation thresholds from 0.11 ϵ to 0.03 ϵ .
- Implications for igneous rocks are that it is only possible to crystallize monomineralic rocks from a melt if compaction and/or convection and hence equilibration is occurring.

Chapter 7

Concluding Remarks and Future Work

7.0 Conclusions

This thesis has presented a new, general three-dimensional simulation of the textures of unequilibrated crystallizing media that has a wide range of geological applications. In addition, the simulation has been used to develop a new, general method for characterizing the void-space of porous media enabling transport properties, such as permeability and electrical conductivity, for such media to be calculated for larger sample/model volumes than possible previously

The simulations described above have been applied to various geological problems. The three-dimensional simulation of crystallization has been used to investigate the differences between equilibrium and non-equilibrium textures as exhibited by their dihedral angles. This has resulted in a critique of a common technique for investigating the degree of equilibrium in rock samples (Elliott and Cheadle, 1997a, Elliott *et al.* 1997b) (see Chapter 3). In addition the simulation has been used by several co-workers (Jerram *et al.*, 1996, Boyle and Prior, 1997) to test hypotheses on the formation of textures.

The method developed in this thesis for characterizing the void-space of porous media and calculating the permeability and the electrical conductivity has been applied to a tomographic image of a sample of Fontainebleau sandstone. The results calculated for permeability showed good agreement with previous theoretical work and experimental measurements, yet the method used in this thesis is capable of calculating permeability for much larger samples than the previous methods due to reduced computer memory and C.P.U. time requirements. The results for electrical conductivity show good agreement with previous theoretical work, but poor agreement with experimental measurements. This suggested that the neglect of surface conduction by current methods of calculating electrical conductivity must be addressed in future work. Finally, a combination of the numerical simulation of crystallization and the permeability simulation was used

to calculate permeability/porosity relationships for unequilibrated crystallizing igneous systems which has not been possible previously. These permeability/porosity relationships were then combined with those of Cheadle (1989) for equilibrated systems to produce a set of curves describing the permeability/porosity trends in simple igneous systems for the two end-members of textural evolution. The major conclusions of Chapters 3-6 are summarized below:

i) Chapter 3

- A new 3-D voxel-based simulation of the evolution of textures in unequilibrated crystallizing systems has been developed.
- Capable of modelling:
 - Any nuclei distributions.
 - Any nucleation rate.
 - Any crystal shape.
 - Anisotropic crystal growth rates.
 - Multiple phases of crystallization.

ii) Chapter 4

- A 3-D simulation of crystallizing unequilibrated systems has been used to investigate the distributions of apparent dihedral angles expected for unequilibrated rock textures for comparison with those expected in equilibrated rock textures.
- The results of this investigation for fully crystallized, unequilibrated, monomineralic rocks were:
 - The distribution of apparent dihedral angles is similar to that expected from an equilibrated rock.
 - The distribution of apparent dihedral angles is largely independent of nuclei distribution and crystal shape.
- The results of this investigation for partially crystallized, unequilibrated rocks were:
 - Measurement of apparent dihedral angles at closed, triangular pores can produce results that mimic those of equilibrated rocks.

- Conclusion: care must be taken when interpreting textural equilibrium from apparent dihedral angle distributions.

iii) Chapter 5

- A new, general 3-D voxel-based method for characterizing the void-space of porous media has been developed.
- A network model for calculating the permeability/electrical conductivity has been combined with the void-space characterization method to produce a general method for calculating permeability/electrical conductivity in porous media. This method can be applied to much larger sample/model volumes than the only comparable method (Lattice Gas Automata).
- A 3-D tomographic image of a sample of Fontainebleau sandstone has been used to test the void-space characterization algorithm and permeability/electrical conductivity calculations. This resulted in good agreement between calculated and measured permeability values and poorer agreement for electrical conductivity.

iv) Chapter 6

- Permeability/porosity trends are weakly dependant on nuclei distribution.
- Permeability/porosity trends above 0.18 ϵ are only weakly dependant on grain shape and degree of equilibration for the models investigated in this thesis.
- Permeability/porosity trends below 0.18 ϵ are strongly dependant on grain shape and degree of equilibration.
 - Equilibration results in very low percolation thresholds ($<0.01 \epsilon$).
 - Grain shape results in a range of percolation thresholds from 0.11 ϵ to 0.03 ϵ .
- Implications for igneous rocks are that it is only possible to crystallize monomineralic rocks from a melt if compaction and/or convection and hence equilibration is occurring.

7.1 Future Work

The importance of the simulations presented in this thesis is that they allow hypotheses about the physical processes that occur during crystallization to be tested. The following is a list of possible future work.

7.1.2 Fluid-Flow

- 1) **Investigate the effect of multiple phases of nucleation and growth on fluid-flow.** Do small grains crystallizing within the channels formed by larger grains alter the permeability/porosity relationships? What are the permeability/porosity relationships for specific types of rocks, for example, dolomites, granites, in situ crystallization in magma chambers, etc.
- 2) **Investigate the effect of faceted morphologies.** Does increasing the number of facets alter textures/permeability appreciably?
- 3) **Quantify the effect of equilibration of the textures.** What effect does the transition to equilibrium have on permeability?

7.1.3 Textures

- 1) **Use the simulation to calibrate an image analysis program which could then be applied to rock textures.** The current problem with image analysis is that the numerical descriptions of textures produced are meaningless because there is no way of calibrating the analysis. A texture simulation allows the conditions that form the texture to be explicitly specified, therefore this can be related to the results of the analysis.
- 2) **Investigate detailed impingement relationships between crystals.** Can impingement relationships provide fundamental information about the formation of unequilibrated rocks?

References

Avrami, M., 1939, Kinetics of Phase Change. I: Journal of Chemical Physics, v. 7, p. 1103-1112.

Avrami, M., 1940, Kinetics of Phase Change. II: Journal of Chemical Physics, v. 8, p. 212-224.

Avrami, M., 1941, Kinetics of Phase Change. III: Journal of Chemical Physics, v. 9, p. 177-184.

Baldwin, C., Sederman, A. J., Mantle, M. D., Alexander, P., and Gladden, L. F., 1996,
Determination and Characterization of the Structure of a Pore Space from 3D Volume
images: Journal of Colloid and Interface Science, v. 181, p. 79-92.

Bear, J., 1972, Dynamics of fluids in porous media: New York, Elsevier, 764 p.

Beavers, G., Sparrow, E., and Rodenz, D., 1973, Influence of bed size on the flow characteristics and
porosity of randomly packed beds of spheres: Transactions of the American Society of
Mechanical Engineers: Journal of Applied Mechanics, v. 98, p. 655-660.

Beeré, W., 1975, A unifying theory of the stability of penetrating liquid phases and sintering pores:
Acta Metallurgica, v. 23, p. 131-138.

Berkebile, C. A., and Dowty, E., 1982, Nucleation in laboratory charges of basaltic composition:
American Mineralogist, v. 67, p. 886-899.

Bernabé, Y., Brace, W. F., and Evans, B., 1982, Permeability, porosity and pore geometry of hot-
pressed calcite: Mechanics of Materials, v. 1, p. 173-183.

- Berryman, J. G., and Milton, G. W., 1985, Normalization constraint for variational bounds on fluid permeability: *Journal of Chemical Physics*, v. 83, p. 754-760.
- Blair, S. C., Berge, P. A., and Berryman, J. G., 1996, Using two-point correlation functions to characterize microgeometry and estimate permeabilities of sandstone and porous glass: *Journal of Geophysical Research*, v. 101, p. 20359-20375.
- Bonnecaze, R. T., and Brady, J. F., 1990, A method for determining the effective conductivity of dispersions of particles: *Proceedings of the Royal Society of London Series A-Mathematical and Physical Sciences*, v. 430, p. 285-313.
- Bourbie, T., and Zinszner, B., 1985, Hydraulic and Acoustic Properties as a Function of Porosity in Fontainebleau Sandstone: *Journal of Geophysical Research*, v. 90, p. 11524-11532.
- Boyle, A. P., and Prior, D. J., 1997, Unravelling sulphide ore replacement textures using electron backscatter diffraction: evidence for oxidation of pyrite in hydraulic fracture zones, *Structural Controls and Genesis of Economic Resources (Mineral and Hydrocarbon Deposits)*; The Dave Johnston Memorial Meeting, Conference Abstracts, Trinity College Dublin, Ireland.
- Bryant, S., and Blunt, M., 1992, Prediction of relative permeability in simple porous media: *Physical Review A*, v. 46, p. 2004-2011.
- Bryant, S., Cade, C., and Mellor, D., 1993, Permeability prediction from geologic models: *The American Association of Petroleum Geologists Bulletin*, v. 77, p. 1338-1350.
- Bryant, S., and Pallatt, N., 1996, Predicting formation factor and resistivity index in simple sandstones: *Journal of Petroleum Science and Engineering*, v. 15, p. 169-179.

- Bryon, D. N., Atherton, M. P., Cheadle, M. J., and Hunter, R. H., 1996, Melt movement and the occlusion of porosity in crystallizing granitic systems: *Mineralogical Magazine*, v. 60, p. 163-171.
- Campbell, I. H., 1996, Fluid Dynamic Processes in Basaltic Magma Chambers, *in* Cawthorn, R. G., ed., *Layered Intrusions*: Amsterdam, Elsevier Science B.V., p. 45-76.
- Cheadle, M. J., 1989, Properties of Texturally Equilibrated Two-Phase Aggregates: Ph.D. Dissertation, University of Cambridge.
- Chu, C. F., and Ng, K. M., 1989, Flow in packed tubes with a small tube to particle diameter ratio: *American Institute of Chemical Engineers Journal*, v. 35, p. 148-158.
- Coelho, D., Thovert, J. F., and Adler, P. M., 1997, Geometrical and transport properties of random packings of spheres and aspherical particles: *Physical Review E*, v. 55, p. 1959-1978.
- Coker, D. A., Torquato, S., and Dunsmuir, J. H., 1996, Morphology and physical properties of Fontainebleau sandstone via a tomographic analysis: *Journal of Geophysical Research*, v. 101, p. 17497-17506.
- Darcy, H., 1856, *Les Fontaines Publiques de la Ville de Dijon*: (Paris: Dalmont).
- David, C., 1993, Geometry of Flow Paths for Fluid Transport in Rocks: *Journal of Geophysical Research*, v. 98, p. 12267-12278.
- Deckman, H. W., D'Amico, K. L., Dunsmuir, J. H., Flannery, B. P., and Gruner, S. M., 1989, Microtomography detector design: its not just resolution: *Advances in X-Ray Analysis*, v. 32, p. 641.

- D'Humieres, D., Lallemand, P., and Frisch, U., 1986, Lattice gas models for 3D hydrodynamics: *Europhysics Letters*, v. 2, p. 291.
- Dowty, E., 1980, Crystal growth and nucleation theory and the numerical simulation of igneous crystallization, *in* Hargraves, R. B., ed., *Physics of Magmatic Processes*: Princeton, New Jersey, Princeton University Press, p. 419-485.
- Doyen, P. M., 1988, Permeability, conductivity, and pore geometry of sandstone: *Journal of Geophysical Research*, v. 93, p. 7729-7740.
- Dullien, F. A. L., 1975, Single-phase flow through porous media and pore structure: *Chemical Engineering Journal*, v. 10, p. 1.
- Dullien, F. A. L., 1991, Characterization of Porous Media - Pore Level: *Transport in Porous Media*, v. 6, p. 581-606.
- Dullien, F. A. L., 1992, *Porous media: fluid transport and pore structure*: New York, Academic Press.
- Elliott, M. T., and Cheadle, M. J., 1997a, On the identification of textural equilibrium in rocks using dihedral angle measurements: Reply: *Geology*, v. 25, p. 1055.
- Elliott, M. T., Cheadle, M. J., and Jerram, D. A., 1997b, On the identification of textural equilibrium in rocks using dihedral angle measurements: *Geology*, v. 25, p. 355-358.
- Ergun, S., and Orning, A., 1949, Fluid flow through randomly packed columns and fluidized beds: *Industrial Engineering Chemistry*, v. 41, p. 1179-1184.

- Fatt, I., 1956, The network model of porous media I. Capillary pressure characteristics: *Petroleum Transactions of the A.I.M.E*, v. 209, p. 114.
- Faul, U. H., 1997, Permeability of partially molten upper mantle rocks from experiments and percolation theory: *Journal of Geophysical Research*, v. 102, p. 10299-10311.
- Finney, J., 1968, Random packings and the structure of the liquid state: Ph.D. Dissertation, University of London.
- Flannery, B. P., Deckman, H. W., Roberge, W. G., and D'Amico, K. L., 1987, Three-Dimensional X-ray Microtomography: *Science*, v. 237, p. 1439-1444.
- Fredrich, J. T., Greaves, K. H., and Martin, J. W., 1993, Pore Geometry and Transport Properties of Fontainebleau Sandstone: *International Journal of Rock Mechanics*, v. 30, p. 691-697.
- Fredrich, J. T., Menéndez, B., and Wong, T. F., 1995, Imaging the pore structure of geomaterials: *Science*, v. 268, p. 276-278.
- German, R. M., 1985, *Liquid Phase Sintering*: New York, Plenum.
- Gilbert, E. N., 1961, Random Subdivisions of Space into Crystals: *Annals of Mathematical Statistics*, v. 33, p. 958-972.
- Halliday, D., and Resnick, R., 1988, *Fundamental Physics*: New York, John Wiley & Sons, Inc.
- Hamilton, R. T., 1997, Darcy Constant for Multisized Spheres with No Arbitrary Constant: *American Institute of Chemical Engineers Journal*, v. 43, p. 835-836.

Happel, J., and Brenner, H., 1973, Low Reynolds number hydrodynamics with special applications to particulate media: Leyden, Noordhoff International Publishing.

Harker, D., and Parker, E. R., 1945, Grain shape and grain growth: Transactions of the American Society of Metallurgists, v. 34, p. 156-195.

Hasimoto, H., 1959, On the periodic fundamental solutions of the Stokes equations and their application to viscous flow past a cubic array of spheres: Journal of Fluid Mechanics, v. 5, p. 317-328.

Holness, M. B., and Graham, C. M., 1991, Equilibrium dihedral angles in the system H₂O-CO₂-NaCl-calcite, and implications for fluid flow during metamorphism: Contributions to Mineralogy and Petrology, v. 108, p. 368-383.

Hort, M., and Spohn, T., 1991, Crystallization calculations for a binary melt cooling at constant rates of heat removal: implications for the crystallization of magma bodies: Earth and Planetary Science Letters, v. 107, p. 463-474.

Hunter, R. H., 1987, Textural equilibrium in layered igneous rocks: Dordrecht, Reidel, v. Origins of Igneous Layering.

Hunter, R. H., 1996, Texture Development in Cumulate Rocks, *in* Cawthorn, R. G., ed., Layered Intrusions: Amsterdam, Elsevier Science B.V., p. 77-101.

Jerram, D. A., Cheadle, M. J., Hunter, R. H., and Elliott, M. T., 1996, The spatial distribution of grains and crystals in rocks: Contributions to Mineralogy and Petrology, v. 125, p. 60-74.

Johnson, W. A., and Mehl, R. F., 1939, Reaction kinetics in processes of nucleation and growth: Transactions of the A.I.M.E., v. 135, p. 416-458.

- Katz, A. J., and Thompson, A. H., 1986, Quantitative prediction of permeability in porous rock: *Physical Review B-Condensed Matter*, v. 34, p. 8179-8181.
- Katz, A. J., and Thompson, A. H., 1987, Prediction of rock electrical conductivity from mercury injection measurements: *Journal of Geophysical Research*, v. 92, p. 599-607.
- King, P. R., 1987, The use of field theoretic methods for the study of flow in a heterogeneous porous medium: *Journal of Physics A*, v. 20, p. 3935-3947.
- Kingery, W. D., 1963, Effects of microstructure on the properties of ceramics, *in* Klingsberg, C., ed., *The Physics and Chemistry of Ceramics*, Proceedings of a symposium held at Pennsylvania State University, May 28-30, 1962: New York, Gordon and Breach, p. 286-310.
- Kirkpatrick, R. J., 1981, Kinetics of Crystallization of Igneous Rocks, *in* Lasaga, A. C., and Kirkpatrick, R. J., eds., *Reviews in Mineralogy, Kinetics of Geochemical Processes*: Michigan, Mineralogical Society of America, v. 8, p. 321-398.
- Kirkpatrick, R. J., 1983, Theory of nucleation in silicate melts: *American Mineralogist*, v. 68, p. 66-77.
- Koplik, J., Lin, C., and Vermette, M., 1984, Conductivity and permeability from microgeometry: *Journal of Applied Physics*, v. 56, p. 3127-3131.
- Kretz, R., 1966, Interpretation of the Shape of Mineral Grains in Metamorphic Rocks: *Journal of Petrology*, v. 7, p. 68-94.
- Kreuzig, E., 1993, *Advanced Engineering Mathematics*: New York, John Wiley & Sons, Inc.

- Kwiecien, M. J., Macdonald, I. F., and Dullien, F. A. L., 1990, 3-Dimensional reconstruction of porous-media from serial section data: *Journal of Microscopy*, v. 159, p. 343-359.
- Landauer, R., 1978,, *in* Garland, J. C., and Tanner, D. B., eds., *Electrical Transport and Optical Properties of Inhomogeneous Media*: New York, AIP.
- Larson, R. E., and Higdon, J. J. L., 1989, A periodic grain consolidation model of porous media: *Physics of Fluids A-Fluid Dynamics*, v. 1, p. 38-46.
- Lin, C., and Cohen, M. H., 1982, Quantitative methods for geometric modelling: *Journal of Applied Physics*, v. 53(6), p. 4152-4165.
- Lofgren, G. E., 1980, Experimental studies on the dynamic crystallization of silicate melts, *in* Hargraves, R. B., ed., *Physics of Magmatic Processes*: Princeton, Princeton University Press, p. 487-551.
- Lofgren, G. E., 1983, Effect of heterogeneous nucleation on basaltic textures: A dynamic crystallization study: *Journal of Petrology*, v. 24, p. 229-255.
- Macdonald, M. J., Chu, C.-F., Guilloit, P. P., and Ng, K. M., 1991, A Generalized Blake-Kozeny Equation for Multisized Spherical Particles: *American Institute of Chemical Engineers Journal*, v. 37, p. 1583-1588.
- Miyazaki, K., 1991, Ostwald ripening of garnet in high P/T metamorphic rocks: *Contributions to Mineralogy and Petrology*, v. 108, p. 118-128.
- Naslund, H. R., and McBirney, A. R., 1996, Mechanisms of Formation of Igneous Layering, *in* Cawthorn, R. G., ed., *Layered Intrusions*: Amsterdam, Elsevier Science B.V., p. 1-43.

- Olson, J. F., 1995, Two-fluid flow in Sedimentary Rock: Complexity, Transport, and Simulation: Ph.D. Dissertation, Massachusetts Institute of Technology.
- Philips, O. M., 1991, Flow and Reactions in Permeable Rocks: Cambridge, Cambridge University Press.
- Pitas, I., 1993, Digital image processing algorithms: New York, Prentice-Hall International, Inc.
- Prager, S., 1961, Viscous flow through porous media: Physics of Fluids A-Fluid Dynamics, v. 4, p. 1477.
- Pratt, W. K., 1991, Digital Image Processing: New York, Wiley.
- Riegger, O. K., and Van Vlack, L. H., 1960, Dihedral angle measurement: Transactions of the Metallurgical Society of A.I.M.E., v. 218, p. 933-935.
- Roberts, J. N., and Schwartz, L. M., 1985, Grain consolidation and electrical conductivity in porous media: Physical Review B-Condensed Matter, v. 31, p. 5990-5997.
- Rubinstein, J., and Torquato, S., 1988, Diffusion-controlled reactions - mathematical formulation, variational-principles and rigorous bounds: Journal of Chemical Physics, v. 88, p. 6372-6380.
- Sahimi, M., 1993, Flow phenomena in rocks: from continuum models to fractals, percolation, cellular automata, and simulated annealing: Reviews of Modern Physics, v. 65, p. 1393-1534.
- Schwartz, L. M., Auzerias, F., Dunsmuir, J., Martys, N., Bentz, D. P., and Torquato, S., 1994, Transport and diffusion in three-dimensional composite media: Physica A, v. 207, p. 28-36.

Schwartz, L. M., and Banavar, J. R., 1989, Transport properties of disordered continuum systems: Physical Review B-Condensed Matter, v. 39, p. 11965-11970.

Sederman, A. J., Johns, M. L., Bramley, A. S., Alexander, P., and Gladden, L. F., 1997, Magnetic resonance imaging of liquid flow and pore structure within packed beds: Chemical Engineering Science, v. 52, p. 2239-2250.

Serra, J., 1982, Image Analysis and Mathematical Morphology: London, Academic Press.

Smith, C. S., 1948, Grains, Phases and Interfaces: An Interpretation of Microstructure: Transactions of the A.I.M.E., v. 175, p. 15-51.

Spanne, P., Thovert, J. F., Jacquin, C. J., Lindquist, W. B., Jones, K. W., and Adler, P. M., 1994, Synchrotron Computed Microtomography of Porous Media: Topology and Transports: Physical Review Letters, v. 73, p. 2001-2004.

Stickels, C. A., and Hucke, E. E., 1964, Measurement of Dihedral Angles: Transactions of the A.I.M.E., v. 230, p. 795-801.

Thompson, D'A. W., 1942, On Growth and Form: Cambridge, Cambridge University Press.

Thovert, J. F., Salles, J., and Adler, P. M., 1993, Computerized characterization of the geometry of real porous media: their discretization, analysis and interpretation: Journal of Microscopy, v. 170, p. 65-79.

Uhlmann, D. R., Chalmers, B., and Jackson, K. A., 1964, Interaction Between Particles and a Solid-Liquid Interface: Journal of Applied Physics, v. 35, p. 2986-2993.

- Vernon, R. H., 1968, Microstructures of High-grade Metamorphic Rocks at Broken Hill, Australia: *Journal of Petrology*, v. 9, p. 1-22.
- Vernon, R. H., 1970, Comparative grain-boundary studies of some basic and ultrabasic granulites, nodules and cumulates: *Scottish Journal of Geology*, v. 6, p. 337-351.
- Von Bargen, N., and Waff, H. S., 1986, Permeabilities, Interfacial Areas and Curvatures of Partially Molten Systems: Results of Numerical Computations of Equilibrium Microstructures: *Journal of Geophysical Research*, v. 91, p. 9261-9276.
- Waff, H. S., and Bulau, J. R., 1982, Experimental determination of near-equilibrium textures in partially molten silicates at high pressure: Tokyo, Center for Academic Publications, v. 12; *Advances in Earth and Planetary Sciences, High Pressure Research in Geophysics*.
- Watson, E. B., and Brenan, J. M., 1987, Fluids in the lithosphere, 1. Experimentally-determined wetting characteristics of CO₂-H₂O fluids and their implications for fluid transport, host-rock physical properties, and fluid inclusion formation: *Earth and Planetary Science Letters*, v. 85, p. 497-515.
- Zhang, S., Paterson, M. S., and Cox, S. F., 1994, Porosity and permeability evolution during hot isostatic pressing of calcite aggregates: *Journal of Geophysical Research*, v. 99, p. 15741-15760.
- Zhang, X., and Knackstedt, M. A., 1995, Direct simulation of electrical and hydraulic tortuosity in porous solids: *Geophysical Research Letters*, v. 22, p. 2333-2336.
- Zhao, H. Q., and Macdonald, I. F., 1993, An unbiased and efficient procedure for 3-D connectivity measurement as applied to porous media: *Journal of Microscopy*, v. 172, p. 157-162.

Zhao, H. Q., Macdonald, I. F., and Kwiecien, M. J., 1994, Multiorientation scanning - A necessity in the identification of pore necks in porous-media by 3-D reconstruction from serial section data: *Journal of Colloid and Interface Science*, v. 162, p. 390-401.

Appendix A: Publications in Support of this Thesis

Elliott, M. T., and Cheadle, M. J., 1997a, On the identification of textural equilibrium in rocks using dihedral angle measurements: Reply: *Geology*, v. 25, p. 1055.

Elliott, M. T., Cheadle, M. J., and Jerram, D. A., 1997b, On the identification of textural equilibrium in rocks using dihedral angle measurements: *Geology*, v. 25, p. 355-358.

Jerram, D. A., Cheadle, M. J., Hunter, R. H., and Elliott, M. T., 1996, The spatial distribution of grains and crystals in rocks: *Contributions to Mineralogy and Petrology*, v. 125, p. 60-74.

